Earth and Space Science

RESEARCH ARTICLE
10.1029/2021EA001844

Key Points:

- Spectral bands are presented for remote detection of anhydrous carbonates and nitrates
- Mid-IR band center comparisons for the ν_3 vibration compared to the ν_2 and ν_4 vibrations enable identification of carbonate chemistry
- NIR band center comparisons for ~2.3 versus 2.5 μm, ~2.3 versus 4 μm, and ~3.4 versus 4 μm best enable identification of carbonate chemistry

Supporting Information:

Supporting Information may be found in the online version of this article.

Correspondence to:

J. L. Bishop,
jbishop@seti.org

Citation:

Bishop, J. L., King, S. J., Lane, M. D., Brown, A. J., Lafuente, B., Hiroi, T., et al. (2021). Spectral properties of anhydrous carbonates and nitrates. *Earth and Space Science*, *8*, e2021EA001844. https://doi.org/10.1029/2021EA001844

Received 12 MAY 2021
Accepted 17 AUG 2021

Spectral Properties of Anhydrous Carbonates and Nitrates

J. L. Bishop[1,2], S. J. King[1], M. D. Lane[3], A. J. Brown[4], B. Lafuente[1,2], T. Hiroi[5], R. Roberts[6], G. A. Swayze[7], J.-F. Lin[6], and M. Sánchez Román[8]

[1]SETI Institute, Mountain View, CA, USA, [2]NASA-Ames, Moffett Field, CA, USA, [3]Fibernetics LLC, Lititz, PA, USA, [4]Plancius Research LLC, Severna Park, MD, USA, [5]Brown University, Providence, RI, USA, [6]University of Texas at Austin, Austin, TX, USA, [7]US Geological Survey, Denver, CO, USA, [8]Free University, Amsterdam, The Netherlands

Abstract The spectral properties of anhydrous carbonates and nitrates are dominated by strong, sharp vibrational bands due to the CO_3^{2-} and NO_3^- anions observed as absorption bands in near-infrared spectra, as Reststrahlen features or absorption bands in mid-IR spectra, depending on particle size, and as peaks in Raman spectra. These spectral features provide a reliable means to identify the occurrence of carbonates and nitrates on planetary surfaces, which in turn contribute to our understanding of the environment and chemistry of planetary bodies. Four modes occur for carbonates and nitrates due to symmetric stretching (ν_1), out-of-plane bending (ν_2), asymmetric stretching (ν_3), and in-plane bending (ν_4). The vibrational absorptions of these spectral features vary with the mineral structure and the size of the cation, where the calcite-, dolomite-, aragonite-, and alkali-type structures result in different spectral features. Mid-IR bands for carbonates and nitrates occur from 1,040 to 1,105 cm^{-1} for ν_1, from 810 to 906 cm^{-1} for ν_2, from 1,275 to 1,590 cm^{-1} for ν_3, and from 670 to 756 cm^{-1} for ν_4. In Raman spectra the carbonate and nitrate absorptions are observed near 1,050–1,080 cm^{-1} for ν_1, near 880 cm^{-1} for ν_2, near 1,415–1,430 cm^{-1} for ν_3, and near 680–700 cm^{-1} for ν_4. NIR spectra include bands due to overtones and combinations at ~1.75, 1.9, 2.0, 2.3, 2.5, 3.4, 4.0, and 4.6 μm for carbonates and ~1.8, 2.0, 2.2, 2.4, 2.6, 3.5, 4.1, and 4.8 μm for nitrates. This study provides data for remote determination of carbonate and nitrate chemistry and will enable better characterization of these minerals on planetary bodies including Mars, Ceres, and Bennu.

Plain Language Summary Carbonates are widespread minerals on Earth and have been identified as well on Mars, Ceres, near Earth asteroid (101955) Bennu, and in carbonaceous meteorites. Understanding the spectral properties of carbonates enables detection and characterization of this important mineral group. Furthermore, identifying the specific type of carbonate on planetary surfaces can help us constrain the geochemical environment of these planets or bodies. The spectral properties of nitrates are presented here as well because nitrates exhibit similar spectral features to carbonates due to their similar mineral structures. Nitrates are yet to be detected on planets other than Earth, but nitrogen has been detected on bodies in our Solar System and nitrates may be detected once researchers have access to their spectral properties.

1. Introduction

Carbonates are abundant minerals on Earth, and have also been observed on Mars (Ehlmann et al., 2008), Ceres (Carrozzo et al., 2018), and asteroid (101955) Bennu (Kaplan et al., 2020). Calcite or aragonite have also been detected in cosmic particles inferred to originate from carbonaceous meteoroids disrupted in the upper atmosphere (De Angelis et al., 2011; Rietmeijer et al., 2016). Carbonates form under a variety of aqueous conditions, depending on the specific mineral, and hold clues to the geologic history of carbon and CO_2 cycling on planetary bodies (Grady & Wright, 2006; Martin, 2017). On Earth, carbonates are present in sedimentary, igneous, and metamorphic rocks and are ubiquitous across many regions of the planet (e.g., Deer et al., 1992). Calcite, dolomite, and aragonite are the most abundant carbonates on Earth (e.g., Deer et al., 1992), but Mg-rich carbonates appear to be more common on Mars (Ehlmann et al., 2008; McKay et al., 1996; Wray et al., 2016). Remote detection and characterization of carbonates has been performed on both Earth and Mars using reflectance and emission spectroscopy (Bandfield et al., 2003; Ehlmann et al., 2008; Goetz et al., 1985; Rockwell & Hofstra, 2008) and on Ceres and Bennu using reflectance

Table 1
List of IR and Raman Active Modes

Mode	Vibration	IR active	Raman active
(a) Carbonates and nitrates with trigonal structure, 6-fold symmetry, and smaller cations (calcite-type and dolomite-type minerals)			
ν_1	Symmetric stretching	No	Yes (strong)
ν_2	Out-of-plane bending	Yes	No
ν_3	Asymmetric stretching	Yes (strong)	Yes (weak)
ν_4	In-plane bending	Yes	Yes (strong)
(b) Carbonates and nitrates with orthorhombic structure, 9-fold symmetry, and larger cations (aragonite-type minerals)			
ν_1	Symmetric stretching	Yes (weak)	Yes (strong)
ν_2	Out-of-plane bending	Yes	Yes (weak)
ν_3	Asymmetric stretching	Yes (split)	Yes (split)
ν_4	In-plane bending	Yes (split)	Yes (split)

spectroscopy (De Sanctis et al., 2016; Kaplan et al., 2020). Nitrates are less common on Earth and have not yet been identified on other planets, but their occurrence is an important source of nitrogen (N) for life (Summers, 2012) and they are an important source of fertilizer and explosives, and have been heavily mined in Chile and Peru (Ericksen, 1981).

Carbonates and nitrates form in a variety of anhydrous and hydrated forms (e.g., Adler & Kerr, 1963; Lippmann, 1973; Reeder, 1990a). Anhydrous carbonate spectra are dominated by the vibrational modes of the carbonate CO_3^{2-} anion and anhydrous nitrate spectra are similarly dominated by the vibrational modes of the nitrate NO_3^- anion. The size of the cations in these minerals determines the number of ions immediately surrounding it in the mineral structure, or the coordination number. Carbonates and nitrates containing smaller cations form a 6-fold coordination in the calcite and dolomite groups, while those minerals having larger cations form a 9-fold coordination in the aragonite (Weir & Lippincott, 1961) and alkali groups. The calcite group has a trigonal crystal system with rhombohedral habit and space group $R\bar{3}c$ (Reeder, 1990b). The dolomite group is similar with a trigonal crystal system and rhombohedral habit, but has space group $R\bar{3}$ because of reduced symmetry due to the presence of multiple cations (Reeder, 1990b). The aragonite group has an orthorhombic crystal system with space group Pmcn (Speer, 1990). Most carbonates have divalent cations, and for this study Fe is assumed to be present as Fe^{2+}, which fits best in the carbonate lattice structure. Alkali earth carbonates, containing monovalent Na^+ or K^+ cations, have monoclinic crystal structures and natrite (Na_2CO_3) may have 7-fold coordination (Zubkova et al., 2002), rather than 9-fold coordination. Nitrates are observed with trivalent cations as well as divalent cations and both ferric and ferrous nitrates are possible.

The Ca^{2+} cation can be found in both rhombohedral and orthorhombic structures as calcite and aragonite, while most other cations occur in only one group. The most common calcite group minerals include calcite ($CaCO_3$), siderite ($FeCO_3$), and magnesite ($MgCO_3$). Other carbonates with less common cations also fall in this category: rhodochrosite ($MnCO_3$), smithsonite ($ZnCO_3$), and otavite ($CdCO_3$). The carbonates dolomite ($CaMg(CO_3)_2$) and ankerite ($Ca(Fe,Mg,Mn)(CO_3)_2$) are very similar to the calcite group but have reduced symmetry due to mixed cations. Aragonite ($CaCO_3$) is the most common carbonate with orthorhombic structure; others include cerussite ($PbCO_3$), strontianite ($SrCO_3$), and witherite ($BaCO_3$). A complete list of anhydrous carbonate minerals can be found in Railsback (1999).

Four vibrations occur for anhydrous carbonates and nitrates in the mid-IR region due to symmetric and asymmetric vibrations of the CO_3^{2-} and NO_3^- anions (Table 1). These include the *symmetric stretching vibration* (ν_1), the *out-of-plane bending vibration* (ν_2), the *asymmetric stretching vibration* (ν_3), and the *in-plane bending vibration* (ν_4) (e.g., Adler & Kerr, 1963; Lane & Christensen, 1997; Scheetz & White, 1977; Weir & Lippincott, 1961; White, 1974). For the trigonal calcite and dolomite structures the ν_1 band is not IR active (i.e., not predicted to occur, see Table 1), thus only three bands are observed in IR spectra. In contrast, the aragonite structure is orthorhombic and all four vibrations are IR active. Additionally, the ν_3 and ν_4 bands are split, resulting in six bands in IR spectra. In some cases a weak ν_1 band is observed for trigonal

carbonates, likely due to structural perturbations. The ν_1, ν_3, and ν_4 modes are Raman active and these three vibrations are expected as peaks in spectra of calcite-type carbonates; however, the ν_3 peak is very weak and is not always observed (e.g., Buzgar et al., 2009; Gunasekaran et al., 2006; Krishnamurti, 1960). For Raman spectra of the aragonite-type carbonates, the ν_2 mode is often weakly observed and the ν_3 and ν_4 modes are typically split into two vibrations (e.g., Buzgar et al., 2009; Gunasekaran et al., 2006; Krishnamurti, 1960).

Early studies of mid-IR spectra of carbonates and nitrates were measured of mineral powders mixed with potassium bromide (KBr) salt (e.g., Adler & Kerr, 1963; Weir & Lippincott, 1961; White, 1974). This technique produced strong and sharp peaks and the KBr prevented the bands from becoming saturated. The spectral properties of numerous minerals were characterized in this way (Farmer, 1974) with a focus on the fundamental vibrations occurring from about 700 to 1,800 cm^{-1} in order to probe mineral structures and correlate infrared vibrations with X-ray diffraction (XRD) parameters. Salisbury et al. (1987) investigated calcite from 400 to 4,000 cm^{-1} using transmittance and reflectance spectroscopy and discovered the presence of multiple overtone and combination bands in the range 1,700–4,000 cm^{-1} that are useful for identification of minerals. Furthermore, Salisbury et al. (1987) noted that the strength of these overtone and combination bands tends to increase with smaller particle size, while the strength of the fundamental bands decreases with smaller particle size. This trend was investigated for several carbonate minerals including calcite, dolomite, aragonite, and cerussite (Salisbury et al., 1991). Selected carbonate spectra from their study are shown in Figure 1 to illustrate comparisons of transmittance spectra with reflectance spectra of natural mineral surfaces, the 75–250 μm size fraction, and the <75 μm size fraction.

Near-infrared (NIR) reflectance spectra of anhydrous carbonates follow trends in band positions with cation type and structure (Bishop et al., 2017; Crowley, 1986, 1987; Gaffey, 1985, 1986, 1987; Hunt & Salisbury, 1971), while the spectral properties of hydrous carbonates are largely dominated by water bands, especially in the NIR region (Calvin et al., 1994; Harner & Gilmore, 2015). Nitrates follow similar trends (Bishop et al., 2017; Cloutis et al., 2016; Sutter et al., 2007; Wang et al., 2018). The spectral features depend on the mineral structure, as well as the size and charge of the cation. The most common carbonate cations include Ca^{2+}, Mg^{2+}, Fe^{2+}, Mn^{2+}, Sr^{2+}, Pb^{2+}, and Ba^{2+}. The effective ionic radius is a measure of the size of the cation in the mineral structure and depends on the size of the atom, number of electrons, and coordination number to the carbonate or nitrate ion (e.g., Shannon, 1976). These values are given for the electronic high spin states of several cations found in carbonates and nitrates (Shannon, 1976) and are listed in Table 2. Under ambient conditions the high spin state is favored for these cations in carbonate and nitrate minerals and a transition to the low spin state is observed at elevated pressures (e.g., Lin et al., 2012; Mattila et al., 2007). Ammonium nitrate (NH_4NO_3) crystallizes in a few polymorphic structures with the orthorhombic structure most common at room temperature and a trigonal structure possible at elevated temperatures (e.g., Hendricks et al., 1932; Théorêt & Sandorfy, 1964). The effective ionic radius is computed at 1.48 angstroms (Å) for the 6-fold form, at 1.54 Å for the 8-fold form, and at 1.67 Å for the 12-fold form (Sidey, 2016); thus, the effective ionic radius for the 9-fold orthorhombic structure is estimated at 1.6 Å (Table 2).

Rigorous spectroscopic analyses of carbonates and nitrates are essential for remote detection of these minerals on planetary surfaces. This study builds on previous measurements and analyses to present spectral data using multiple techniques over extended wavelength ranges for a significantly broader compositional range including several types of cations and mineral structures. Investigations of reflectance and emission spectra of carbonates and carbonate-bearing samples have been performed in the lab (e.g., Bishop et al., 2011; Bishop, Perry, et al., 2013; Clark et al., 1990; Ehlmann et al., 2008; Gaffey, 1986, 1987; Hunt & Salisbury, 1971; Lane, 1999; Lane & Christensen, 1997, 1998; Salisbury et al., 1991) to support their identification on Mars.

Carbonates have long been predicted to be present on that planet (e.g., Fanale et al., 1982; Gooding, 1978; McKay & Nedell, 1988; Pollack et al., 1987) and have been found at minor or trace abundances in several martian meteorites (e.g., Bishop, Mustard, et al., 1998; Bishop, Pieters, et al., 1998; Gooding et al., 1988; Kirschvink et al., 1997; McKay et al., 1996; Scott et al., 1998; Treiman et al., 1993). Early analyses of telescopic data suggested the presence of carbonates on Mars (Blaney & McCord, 1989; Calvin et al., 1994; Pollack et al., 1990). These early potential detections were confirmed by orbital detections of carbonates using spectra collected by the Compact Reconnaissance Imaging Spectrometer for Mars (CRISM) instrument on the Mars Reconnaissance Orbiter mission (Ehlmann et al., 2008). However, detection of carbonates on Mars has been challenging because they are always mixed with other minerals and rocks at the CRISM

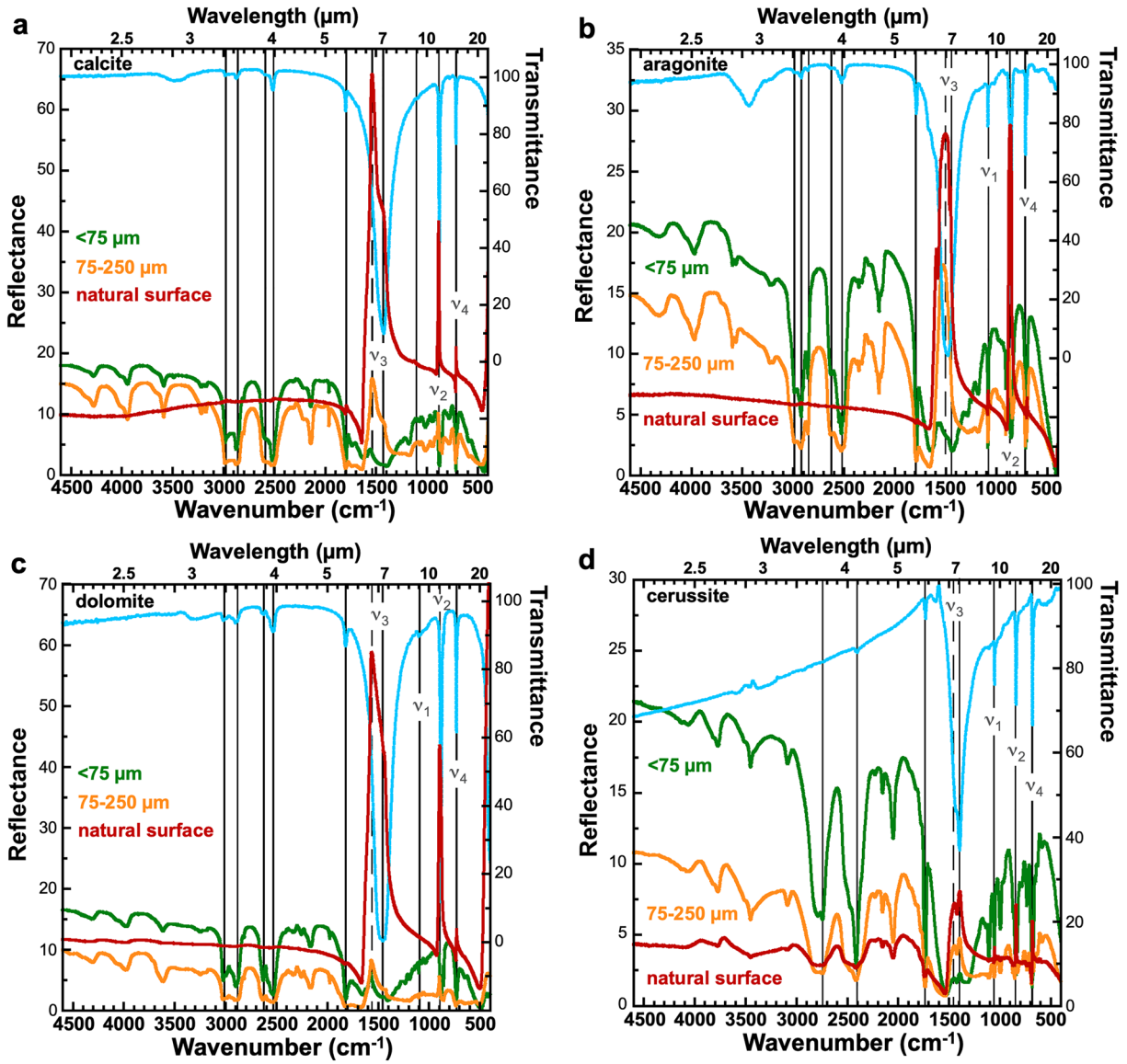

Figure 1. Reflectance spectra of selected carbonates for <75 µm grains (green spectra), 75–250 µm grains (orange spectra), a natural mineral surface (red spectra), and transmittance spectra of KBr pellets (blue spectra). (a) Calcite, (b) Aragonite, (c) Dolomite, (d) Cerussite. Data from Salisbury et al. (1991).

scale of 18 m per pixel at best. Carbonates could also be responsible for a mid-IR doublet near 1,390 and 1,580 cm^{-1} in spectra of martian soil collected by the Thermal Emission Spectrometer (TES) instrument on the Mars Global Surveyor mission (Bandfield et al., 2003), although this doublet could also be due to hydrated iron sulfates (Lane et al., 2004) or the ferric oxyhydroxide mineral ferrihydrite (Bishop & Murad, 2002). The visible/near-infrared (VNIR) characterization of carbonates using spectral bands near 2.3, 2.5, and 3.4 µm in CRISM data have enabled mapping Mg-rich carbonates at Nili Fossae and Jezero crater (Brown et al., 2010, 2020; Ehlmann et al., 2008; Horgan et al., 2020; Viviano et al., 2013), dolomite at Libya Montes (Bishop, Tirsch, et al., 2013; Tirsch et al., 2018), and Ca- or Fe-rich carbonates at Leighton crater (Michalski & Niles, 2010), McLaughlin crater (Michalski et al., 2013) and Huygens crater (Wray et al., 2016). In situ analyses by the Spirit rover also identified Fe/Mg-carbonates on Mars (Morris et al., 2010) that were later observed in CRISM data over the site (Carter & Poulet, 2012). Additionally, small (<1 wt.%) abundances of fine-grained Fe- or Mg-bearing carbonates were assumed to be present at Gale crater to explain evolved gas results measured by the Sample Analysis at Mars instrument on the Mars Science Laboratory (MSL) rover Curiosity (Leshin et al., 2013; Ming et al., 2014).

Table 2
Effective Ionic Radii of Cations Typically Found in Carbonates and Nitrates

Cation	*R* (Å)	Charge	CN
Al	0.54	3	6
Fe	0.64	3	6
Mg	0.72	2	6
Cu	0.73	2	6
Zn	0.74	2	6
Co	0.74	2	6
Li	0.76	1	6
Fe	0.78	2	6
Mn	0.83	2	6
Cr	0.80	2	6
Ti	0.86	2	6
Ca	1.00	2	6
Na	1.02	1	6
NH_4	1.48	1	6
Ca	1.18	2	9
Na	1.24	1	9
Sr	1.31	2	9
Pb	1.35	2	9
Ba	1.42	2	9
K	1.55	1	9
NH_4	~1.6	1	9

Note. *R* is the effective ionic radius in Å; values for metals are from Shannon (1976) and for ammonia from Sidey (2016); CN is the coordination number; values given are for high spin state (favored).

Another reason detection of carbonates on Mars has been a challenge is due to the sparse and thin occurrences across the planet. Characterization of the composition of these carbonate outcrops requires a detailed understanding of the spectral properties of these minerals. Therefore, providing a comprehensive database of carbonate spectral features for remote identification was the motivation for this study. Nitrates follow related structural and spectral trends and may also be present on Mars and other Solar System bodies. For these reasons we added nitrates to this study as well. This work encompasses VNIR reflectance and mid-IR reflectance and emission spectra for comparison with orbital spectra of Mars and in situ data where available. Raman spectroscopy is included in this study because the Mars 2020 rover mission includes a Raman spectrometer (Beegle et al., 2015) that is probing sediments at Jezero crater in search of carbonates. The MSL rover possesses an XRD instrument (Blake et al., 2013) and is characterizing the mineralogy of Gale crater and may be able to identify carbonates or nitrates if sufficiently abundant. However, to date neither has been detected at Gale crater by the CHEmistry and MINeralogy (CheMin) XRD instrument (Rampe et al., 2020). The VNIR, mid-IR, Raman, and XRD data of carbonates and nitrates with a wide range of chemistries and structures presented here are intended to support coordinated identification and characterization of carbonates and nitrates on Mars and other planetary surfaces.

2. Materials and Methods

2.1. Samples

Anhydrous carbonate samples were collected over a number of years from multiple sources for this study (Bishop, Perry, et al., 2013; King et al., 2014; Lane & Bishop, 2019; Lane & Christensen, 1997; Lin et al., 2012) and their purity was confirmed by XRD and/or electron microprobe (Tables 3 and 4). Some carbonates were also acquired with variable abundances of Mg, Fe, and Mn cations (Lin et al., 2012; Liu et al., 2015). The magnesiosiderite sample was obtained from the Vargas Gem and Mineral Collection at the University of Texas at Austin (collection number: V3817), and has a chemical composition of $(Fe_{0.65}Mg_{0.33}Mn_{0.02})CO_3$ as determined by microprobe analyses (Lin et al., 2012). Other carbonates were synthesized with a range of Ca, Mg, and Fe similar to those in a previous study (Romanek et al., 2009). Synthesis experiments were performed at 25°C–45°C and 1 atm total pressure inside an anaerobic chamber filled with a 4% H_2/96% N_2 gas mixture. Stock solutions (1.0 M) of $NaHCO_3$, $Fe(ClO_4)_2$, $Ca(ClO_4)_2$, and $Mg(ClO_4)_2$ were prepared separately inside the chamber, from which individual solutions of the desired chemistry were made for each experimental run. The pH was adjusted to 8 in all of the experimental runs and the solid precipitates were recovered after 30 days for analysis by XRD and ICP-OES. Some carbonate samples are partially hydrated and tend to exhibit weaker, but still visible, fundamental vibration bands. However, the NIR overtones and combinations were typically more difficult to identify due to the strong hydration bands and disrupted mineral structure.

Several synthetic nitrate samples with different cations were obtained from Scholar Chemistry and Sigma Aldrich https://www.sigmaaldrich.com/. The mid-IR fundamental bands were investigated for each of these synthetic nitrates. However, only the anhydrous nitrates were studied in the NIR region because the hydrous nitrate spectra, similar to hydrous carbonate spectra, are dominated by water features rather than nitrate-related bands.

When sufficient sample material was available, multiple particle size separates were prepared for reflectance spectroscopy measurements. Elemental abundance for several newly acquired samples with sufficient material was determined at Bureau Veritas (formerly ACME labs) using X-ray Fluorescence (XRF) and is reported in Table 5.

Table 3
List of Carbonate Samples Used in This Study

Carbonate sample ID	Mineral name	Chemical formula	Structural type	Description	Location collected or synthesized
JB0551 (ML-C2)	Calcite	$CaCO_3$	Calcite	Pure by XRD, IR	Rodeo, Durango, Mexico, Lane and Christiansen (1997)
JB1457	Calcite	$CaCO_3$	Calcite	Pure by XRD, IR	Mazada, Israel
JB1458	Calcite	$CaCO_3$	Calcite	Pure by XRD, IR	Big Timber, Montana, USA
JB1460	Calcite	$Ca_{0.98}Mg_{0.02}CO_3$	Calcite	Trace organics	Somerset, England
HS194B	Calcite	$CaCO_3$	Calcite		Mexico, Salisbury et al. (1991)
HS48B	Calcite	$CaCO_3$	Calcite		Kansas, Salisbury et al. (1991)
JB0946	Magnesite	$Mg_{0.996}Fe_{0.004}CO_3$	Calcite	Pure by XRD, IR	Brumado Bahia, Brazil
JB1161	Magnesite	$Mg_{0.995}Fe_{0.005}CO_3$	Calcite	Pure by XRD, IR	UT mineral collection, Lin et al. (2012)
JB825 (MS-C1)	Mg-calcite	$Ca_{0.86}Mg_{0.14}CO_3$	Calcite	Partially hydrated	synthesized at 25°C, M. Sánchez Román
JB826 (MS-C2)	Mg-calcite	$Ca_{0.82}Mg_{0.18}CO_3$	Calcite	Partially hydrated	synthesized at 35°C, M. Sánchez Román
JB827 (MS-C3)	Mg-calcite	$Ca_{0.76}Mg_{0.24}CO_3$	Calcite	Partially hydrated	synthesized at 35°C, M. Sánchez Román
JB1162	Mg-siderite	$Mg_{0.33}Fe_{0.65}Mn_{0.02}CO_3$	Dolomite	Pure by XRD, IR	UT mineral collection, Lin et al. (2012)
HS67	Rhodochrosite	$MnCO_3$	Calcite	Pink, 1% Fe	USGS Speclab
HS338	Rhodochrosite	$MnCO_3$	Calcite	Some Fe and Ca substitution, minor orthopyroxene, talc	USGS Speclab
JB1163	Siderite	$Mg_{0.06}Fe_{0.91}Mn_{0.03}CO_3$	Calcite	Pure by XRD, IR	UT mineral collection, Lin et al. (2012)
JB1462	Siderite	$Ca_{0.03}Mg_{0.31}Fe_{0.66}CO_3$	Calcite	Possible minor pyrite	Nova Scotia, Canada
JB1463	Siderite	$Ca_{0.02}Mg_{0.06}Fe_{0.88}Mn_{0.04}CO_3$	Calcite	Minor calcite, organics	Roxbury Iron Mine, CT, USA
ML-C49	Smithsonite	$Zn_{0.91}Ca_{0.03}Fe_{0.04}Mn_{0.02}CO_3$	Calcite	Pure by XRD, IR	San Antonio Mine, Mexico, Lane and Christiansen (1997)
JB0778 (ML-C64)	Ankerite	$Ca(Fe,Mg,Mn)(CO_3)_2$	Dolomite	XRD shows minor calcite, Fe oxides, and silica admixtures	unknown, Lane and Christiansen (1997)
JB832 (MS-S28)	Ankerite	$Ca_{0.50}Mg_{0.28}Fe_{0.22}CO_3$	Dolomite	Partially hydrated	synthesized at 35°C, M. Sánchez Román
JB833 (MS-S29)	Ankerite	$Ca_{0.47}Mg_{0.34}Fe_{0.19}CO_3$	Dolomite	Partially hydrated	synthesized at 45°C, M. Sánchez Román
JB1461	Dolomite	$Ca_{0.52}Mg_{0.40}Fe_{0.08}CO_3$	Dolomite	97.3% dolomite, 2.7% calcite	Selasvann, Norway
NMNH R12596	Dolomite	$Ca_{0.54}Mg_{0.46}CO_3$	Dolomite		Austria, Salisbury et al. (1991)
HS102B	Dolomite	$Ca_{0.59}Mg_{0.41}CO_3$	Dolomite		Massachusetts, Salisbury et al. (1991)
Vergo-1	Dolomite	$Ca_{0.61}Mg_{0.38}Fe_{0.01}CO_3$	Dolomite		Indiana, Salisbury et al. (1991)
JB0779	Dolomite	$Ca(Fe,Mg,Mn)(CO_3)_2$	Dolomite	3% quartz	Copperopolis, CA, USA
JB829 (MS-S22)	Fe/Ca/Mg-carbonate	$Ca_{0.36}Mg_{0.02}Fe_{0.62}CO_3$	Dolomite	Partially hydrated	synthesized at 35°C, M. Sánchez Román
JB830 (MS-S25)	Fe/Ca-carbonate	$Ca_{0.43}Fe_{0.57}CO_3$	Dolomite	Partially hydrated	synthesized at 35°C, M. Sánchez Román
JB831 (MS-S26)	Fe-dolomite	$Ca_{0.55}Fe_{0.45}CO_3$	Dolomite	Partially hydrated, traces of aragonite	synthesized at 45°C, M. Sánchez Román
ML-C43	Kutnahorite	$Ca_{0.97}Mg_{0.04}Fe_{0.01}Mn_{0.96}Zn_{0.01}CO_3$	Dolomite	Pure by XRD, IR	Sterling Hill Mine, Ogdensburg, NJ, Lane and Christiansen (1997)

Table 3
Continued

Carbonate sample ID	Mineral name	Chemical formula	Structural type	Description	Location collected or synthesized
ML-C23	Minrecordite	$CaZn(CO_3)_2$	Dolomite	Pure by XRD, IR	unknown, Lane and Christiansen (1997)
JB1459	Aragonite	$CaCO_3$	Aragonite	Pure by XRD, IR	Minglanilla, Cuenca, Spain
JB1640	Aragonite	$CaCO_3$	Aragonite	Pure by XRD, IR	Tazouta, Sefrou Province, Morocco
JB1659 (ML-C70)	Aragonite	$CaCO_3$	Aragonite	Pure by XRD, IR	Molina de Aragon, Spain, Lane and Christiansen (1997)
NMNH B10083	Aragonite	$CaCO_3$	Aragonite		Czechoslovakia, Salisbury et al. (1991)
JB1745	Potassium carbonate	K_2CO_3		Partially hydrated	Synthetic, Sigma-Aldrich
Vergo-2	Cerussite	$PbCO_3$	Aragonite		Australia, Salisbury et al. (1991)
JB1658 (ML-C66)	Strontianite	$SrCO_3$	Aragonite		Fraser Duntile Quarry, Ottawa, Ontario, Lane and Christiansen (1997)
HS272	Strontianite	$SrCO_3$	Aragonite	Minor Ca substitution	USGS Speclab
HS273	Witherite	$BaCO_3$	Aragonite	Pure by XRD, IR	USGS Speclab
JB1744	Natrite	Na_2CO_3	aragonite		Synthetic, Sigma-Aldrich

Note. Sample chemistry determined by microprobe, bulk oxide analyses, or solid solution rations during synthesis; USGS Speclab data from: https://www.usgs.gov/labs/spec-lab/capabilities/spectral-library.

2.2. XRD

XRD analyses were performed for this study using a portable Terra field XRD unit (Olympus NDT) based on the same technology as CheMin on MSL *Curiosity* rover (Blake et al., 2012). Terra is a transmission XRD instrument using a direct detection charge-coupled device (CCD), a Co X-ray source with Kβ filter, and a

Table 4
List of Nitrate Samples Used in This Study

Nitrate sample ID	Mineral name	Chemical formula	Structural type	Purchased from
JB0994	Aluminum nitrate	$Al(NO_3)_3 \cdot 9H_2O$	Trigonal rhombohedral	Synthetic, Scholar Chemistry
JB1582	Ammonium nitrate	NH_4NO_3	Trigonal rhombohedral	Synthetic, Sigma-Aldrich
JB0995	Ferric nitrate	$Fe(NO_3)_3 \cdot 9H_2O$	Trigonal rhombohedral	Synthetic, Scholar Chemistry
JB1579	Ferric nitrate	$Fe(NO_3)_3 \cdot 9H_2O$	Trigonal rhombohedral	Synthetic, Sigma-Aldrich
JB1583	Lithium nitrate	$LiNO_3$	Trigonal rhombohedral	Synthetic, Sigma-Aldrich
JB0996	Magnesium nitrate	$Mg(NO_3)_2 \cdot 6H_2O$	Trigonal rhombohedral	Synthetic, Scholar Chemistry
JB0997	Sodium nitrate	$NaNO_3$	Trigonal rhombohedral	Synthetic, Scholar Chemistry
JB1584	Sodium nitrate	$NaNO_3$	Trigonal rhombohedral	Synthetic, Sigma-Aldrich
JB1581	Zinc nitrate	$Zn(NO_3)_2 \cdot 3H_2O$	Trigonal rhombohedral	Synthetic, Sigma-Aldrich
JB0998	Potassium nitrate	KNO_3	Orthorhombic	Synthetic, Scholar Chemistry
JB1586	Barium nitrate	$Ba(NO_3)_2$	Orthorhombic	Synthetic, Sigma-Aldrich
JB0997	Sodium nitrate	$NaNO_3$	Orthorhombic	Synthetic, Scholar Chemistry
JB1587	Lead nitrate	$Pb(NO_3)_2$	Orthorhombic	Synthetic, Sigma-Aldrich
JB1585	Strontium nitrate	$Sr(NO_3)_2$	Orthorhombic	Synthetic, Sigma-Aldrich

Table 5
Carbonate Chemistry

Sample Number	JB1457e	JB1458e	JB1460e	JB1459a	JB1459e	JB1640	JB1461a	JB1461e	JB1462e	JB1463e	JB946
Mineral	Calcite	Calcite	Calcite	Aragonite	Aragonite	Aragonite	Dolomite	Dolomite	Siderite	Siderite	Magnesite
Grain size range	125–250 μm	125–250 μm	125–250 μm	<45 μm	125–250 μm	125–250 μm	<45 μm	125–250 μm	125–50 μm	125–250 μm	<125 μm
Composition:											
SiO_2	0.2	0.1	<0.1	1.5	0.2	1.64	0.5	0.3	0.1	2.1	0.49
Al_2O_3	0.11	0.06	0.04	0.54	0.11	0.3	0.04	0.08	0.07	0.12	0.21
Fe_2O_3	0.04	<0.01	0.01	0.17	0.05	0.41	7.16	7.13	49.96	59.41	0.44
CaO	>50.00	>50.00	>50.00	>50.00	>50.00	54.4	30.55	30.72	1.49	0.86	0.19
MgO	0.38	<0.01	0.84	0.35	0.11	<0.01	17.03	17.29	11.72	3.51	46.03
Na_2O	<0.01	<0.01	<0.01	0.01	<0.01	<0.01	<0.01	<0.01	<0.01	<0.01	<0.01
K_2O	<0.01	<0.01	<0.01	0.11	<0.01	0.1	<0.01	<0.01	<0.01	<0.01	0.05
MnO	<0.01	0.06	<0.01	<0.01	<0.01	<0.01	0.17	0.17	0.84	2.64	0.37
TiO_2	<0.01	<0.01	<0.01	0.02	<0.01	0.03	<0.01	<0.01	<0.01	<0.01	<0.01
P_2O_5	<0.01	<0.01	<0.01	<0.01	<0.01	<0.01	<0.01	<0.01	<0.01	<0.01	<0.01
Cr_2O_3	<0.01	<0.01	<0.01	<0.01	<0.01	<0.01	<0.01	<0.01	<0.01	<0.01	<0.002
Ba	<0.01	<0.01	<0.01	<0.01	<0.01	<0.01	<0.01	<0.01	0.03	0.03	<5
Ni	<0.001	<0.001	<0.001	<0.001	<0.001	N/A	0.001	<0.001	0.001	<0.001	<20
Co	<0.001	<0.001	<0.001	<0.001	<0.001	N/A	<0.001	<0.001	<0.001	<0.001	N/A
Cu	0.002	<0.001	0.002	0.003	0.002	N/A	0.004	<0.001	0.08	0.01	N/A
Pb	<0.001	<0.001	0.112	0.001	0.002	N/A	<0.001	<0.001	<0.001	<0.001	N/A
SO_3	0.016	0.011	0.066	0.048	0.044	<0.002	0.004	0.018	0.284	0.027	N/A
Sn	0.01	0.01	0.02	0.02	0.02	N/A	0.01	0.01	0.03	0.03	N/A
Sr	0.003	<0.002	0.022	0.676	0.705	0.21	0.005	0.005	<0.002	<0.002	<2
Zn	<0.001	<0.001	0.898	<0.001	<0.001	N/A	0.001	<0.001	0.011	0.015	N/A
Zr	<0.002	<0.002	<0.002	<0.002	<0.002	N/A	<0.002	<0.002	<0.002	0.003	<5
V_2O_5	<0.002	<0.002	<0.002	<0.002	<0.002	N/A	<0.002	0.002	0.01	0.01	N/A
LOI	43.06	43.08	43.59	42.42	43.43	42.4	44.52	44.59	35.92	31.55	51.5
Sum	100.2	100.06	100.41	100.41	101.16	99.55	99.98	100.35	100.56	100.26	99.22
Total C	12.5	12.6	12.2	12	12.4	12.03	12.8	13	11.8	10.7	N/A

Note. LOI is loss on ignition at 1000°C; total C may include organic C as well as carbonate.

sample holder with a piezoelectric vibration system. This places the sample in motion during the analysis, allowing coarser-grained materials to be analyzed, and reducing preferred orientation effects (Sarrazin et al., 2005). Data were collected from 5 to 55 2θ, and identification of mineral phases was performed using the automated cloud-based application QAnalyze (https://www.qanalyze.com/) and the software Xpowder (www.xpowder.com), together with reference data supplied from the American Mineralogist Crystal Structure Database (Downs & Hall-Wallace, 2003).

Synchrotron XRD patterns were performed previously on samples investigated by Lin et al. (2012) and Liu et al. (2015).

2.3. Emission Spectroscopy

Emission spectra were acquired using a modified Nicolet Nexus 670 Fourier transform infrared (FTIR) interferometric spectrometer over the range 2,000–200 cm^{-1} with 2 cm^{-1} spectral sampling as in Lane and

Christensen (1997, 1998) and Lane and Bishop (2019). Two blackbody targets (at ~70°C and 100°C) were measured to determine the instrument response function and instrument temperature used for data calibration. The emissivity spectra of the minerals, heated to and kept at ~70°C during measurement, were obtained by reducing the raw wavelength and temperature-dependent data according to the one-temperature procedure of Ruff et al. (1997), assuming that sample emissivity equals unity at the Christiansen feature (e.g., Logan et al., 1975; Salisbury, 1993).

2.4. Raman Spectroscopy

Raman spectra were measured in the Mineral Physics Laboratory at the University of Texas on selected samples. This system is equipped with a Coherent Verdi V2 laser with a 532 nm wavelength, an electron multiplying charge-coupled device, and a Shamrock spectrometer from Andor Technology (e.g., Lin et al., 2012). The laser power was limited to ~50 mW to avoid overheating the samples. Multiple Raman spectra were acquired for several grains of each sample to test for purity and obtain the strongest signal.

2.5. Reflectance Spectroscopy

Reflectance spectra were acquired on bulk samples in a horizontal position for this study at Brown University's Reflectance Experiment Laboratory (RELAB) using a bidirectional VNIR spectrometer under ambient conditions relative to Halon and a biconical Nicolet FTIR spectrometer in a controlled, dry environment relative to a rough gold surface as in previous studies (e.g., Bishop, Perry, et al., 2013). The bidirectional spectra were collected from 0.3 to 2.5 μm at 5 nm spectral sampling. Infrared reflectance spectra were measured with 2 cm^{-1} spectral sampling from 1 to 50 μm in a controlled environment purged of H_2O and CO_2 for 10–12 h. Composite, absolute reflectance spectra were prepared by scaling the FTIR data to the bidirectional data near 1.2 μm. Size fractions <45, 45–75, 75–90, 90–125, 125–250, and >250 μm were measured for several samples, while only particulates <125 μm were run when sample volume was limited. For consistency across samples we typically used spectra of the <125 μm or 90–125 μm size fractions for the spectral analyses.

Additional FTIR reflectance spectra were collected at the USGS Spectroscopy Laboratory (Clark et al., 2007; Kokaly et al., 2017) or reported by Salisbury et al. (1991). Many of these samples were first characterized and investigated by Hunt and Salisbury (1971).

2.6. Continuum Removal

A continuum was removed from the carbonate spectra across the ranges 2.20–2.645 and 3.175–4.247 μm and from the nitrate spectra across the ranges 2.25–2.8 and 3.35–4.4 μm in order to facilitate comparison of the band shapes and strengths near 2.3–2.4, 2.5–2.6, 3.4–3.6, and 4–4.2 μm using a technique proposed in Brown (2006) and implemented in Brown et al. (2008). The carbonate bands in cerussite occur at longer wavelengths than the other carbonates and thus the nitrate spectral ranges were used for cerussite in the continuum removal process.

3. XRD of Carbonates and Nitrates

3.1. XRD Lab Measurements

XRD results are shown in Figure 2 for selected samples. The characteristic strongest (hkl) peaks for trigonal structure carbonates including dolomite, siderite, and calcite (Figure 2a), and the trigonal structure nitrate $NaNO_3$ (Figure 2c) correspond to the (012), (104), (006), (110), and (113) crystallographic planes (corresponding *d*-spacing values are listed in Table S1a). The characteristic strongest (hkl) peaks for orthorhombic structure carbonates, including aragonite, strontianite, and witherite (Figure 2b), and the orthorhombic structure nitrate KNO_3 (Figure 2d) correspond to (111), (021), (002), (012), (102), (112), and (130) crystallographic planes (corresponding *d*-spacing values are listed in Table S1b). The diffraction patterns of carbonates and nitrates are well known and available in databases such as RRUFF (Lafuente et al., 2015). Peak positions for the carbonates and nitrates in our study are listed in Table S1.

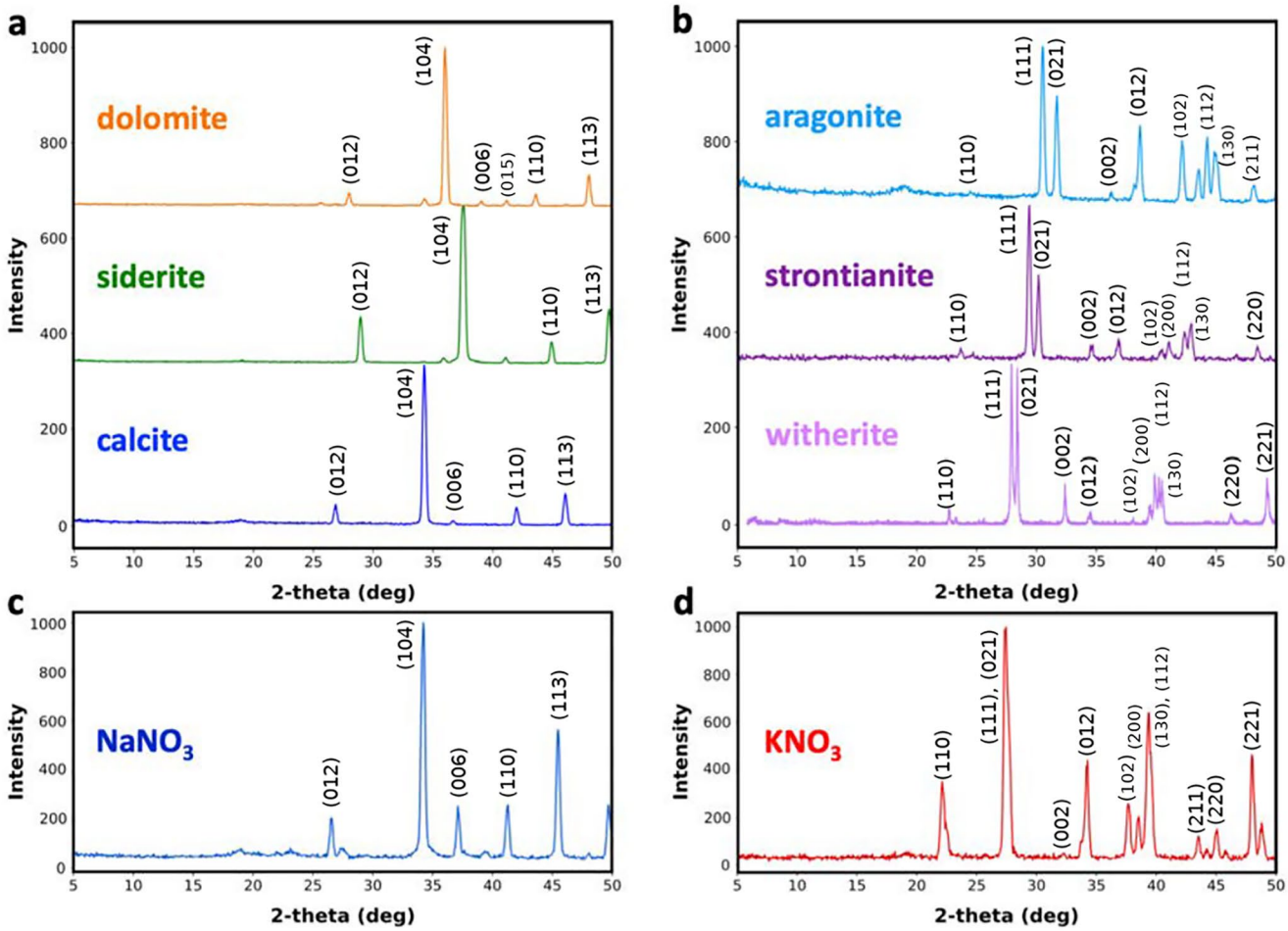

Figure 2. XRD of selected carbonates and nitrates, offset for clarity. (a) Examples of trigonal structure (6-fold) carbonates from our study including dolomite, siderite and calcite. (b) Examples of orthorhombic structure (9-fold) carbonates including aragonite, strontianite, and witherite. (c) $NaNO_3$, a nitrate with trigonal structure. (d) KNO_3, a nitrate with orthorhombic structure.

3.2. XRD Synchrotron Measurements

Synchrotron XRD patterns were measured for the samples from the Lin et al. (2012) and Liu et al. (2015) studies. They observed lattice parameters of the siderite-rich sample as $a = 4.6909$ (±0.0005) Å and $c = 15.3687$ (±0.0049) Å and of the magnesiosiderite $(Fe_{0.65}Mg_{0.33}Mn_{0.02})CO_3$ sample as $a = 4.6753$(±0.0012) Å and $c = 15.2794$ (±0.0030) Å under ambient conditions.

4. Fundamental Vibrations of Carbonates and Nitrates

4.1. Raman Spectra

Raman spectra were measured for selected carbonate and nitrate samples with different chemical compositions to confirm sample purity and compare Raman spectra with the NIR and mid-IR spectra. Raman spectra of calcite, siderite, dolomite, and aragonite are shown in Figures 3a and 3b as examples of carbonates and Raman spectra of $NaNO_3$, $LiNO_3$, KNO_3, $Sr(NO_3)_2$, and $Pb(NO_3)_2$ are shown in Figures 3c and 3d as examples of nitrates. Raman peaks are expected for ν_3 (near 1,400 cm^{-1}), ν_1 (near 1,100 cm^{-1}), and ν_4 (near 700 cm^{-1}) vibrations in spectra of the trigonal, 6-fold symmetry (calcite-type) structures (e.g., Buzgar et al., 2009; Gunasekaran et al., 2006; Krishnamurti, 1960) and this is what we observed in Figure 3a for the trigonal carbonates and in Figure 3c for the trigonal nitrates. The ν_3 peak is generally weak in our carbonate spectra, as observed previously (Gunasekaran et al., 2006). For the orthorhombic structures, a weak peak is sometimes observed for the ν_2 vibration near 800 cm^{-1} and the ν_3 and ν_4 peaks are often split

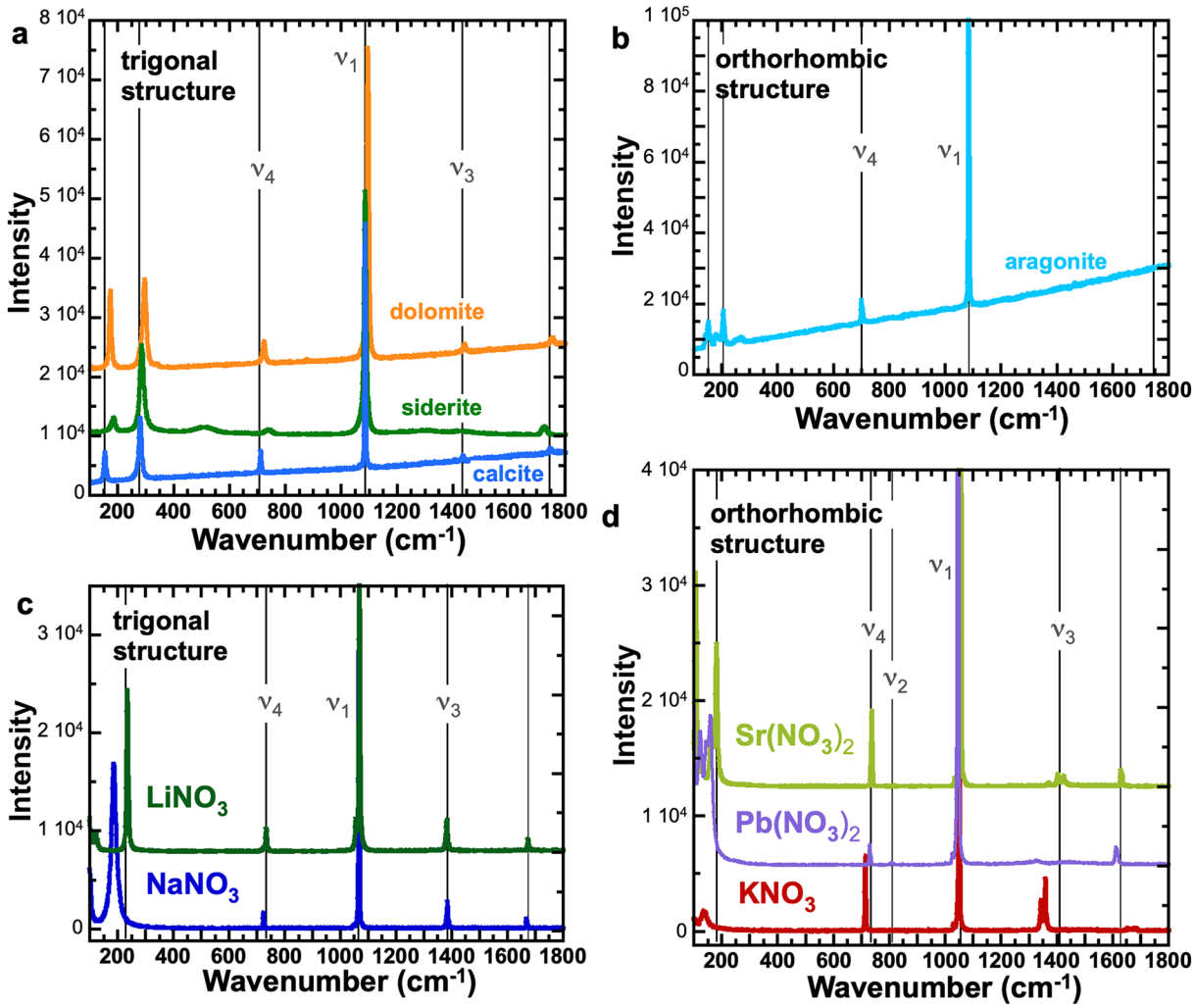

Figure 3. Raman spectra of selected carbonates and nitrates. (a) Example trigonal structure carbonates from our study including dolomite, siderite, and calcite. (b) Aragonite, an orthorhombic structure carbonate. (c) $LiNO_3$ and $NaNO_3$ nitrates with trigonal structure. (d) $Sr(NO_3)_2$, $Pb(NO_3)_2$, and KNO_3 nitrates with orthorhombic structure. Spectra are offset for clarity.

(e.g., Buzgar et al., 2009; Gunasekaran et al., 2006; Krishnamurti, 1960). This trend was observed for the orthorhombic nitrates in our study (Figure 3d). Besides the fundamental stretching and bending vibrations, peaks were observed in our Raman spectra due to lattice modes near 150–300 cm^{-1} and due to a combination band near 1,600–1,700 cm^{-1}. Lattice vibrations occur due to libration and translational motions, termed *L* and *T* lattice modes (e.g., Urmos et al., 1991). Raman peak positions for the fundamental vibrations and *L* and *T* lattice modes are given in Table 6.

4.2. Mid-IR Emissivity Spectra

Mid-IR emissivity spectra are shown in Figure 4 for multiple carbonates from the calcite, dolomite, and aragonite type structures. These spectra were measured of coarse-grained samples (Lane & Bishop, 2019; Lane & Christensen, 1997) and exhibit downward bands (decreased emissivity) in most cases for the fundamental vibrations and lattice modes in emissivity spectra. The single-cation calcite-type trigonal structure spectra are shown in Figure 4a and are offset for clarity and ordered by the position of their symmetric stretching (ν_3) band and lattice vibration. This ordering of the spectra roughly compares with the size of the effective ionic radii of the cation (Table 2) from the smallest (Mg^{2+}) in magnesite to Fe^{2+} in siderite to Mn^{2+} in rhodochrosite and the largest (Ca^{2+}) in calcite, where the smaller cations have higher frequency

Table 6
Raman Peaks in Wavenumbers (cm^{-1}) for Carbonates and Nitrates

a. Carbonates

Sample #	$\nu_1+\nu_4$	ν_3'	ν_3	ν_1	ν_2	ν_4	ν_4'	lattice-L	lattice-T	Source
Magnesite (Mg):	1763		1446	1094		738		330	214	Farsang et al. (2018)
Mg-siderite (Fe/Mg):										
JB1162B				1090		736		303	195	Lin et al. (2012)
Siderite (Fe):	vw		vw	s		w		m		
JB1462F										
JB1463F	1798		1429	1086		734		286	185	this study
	1724			1085		731		284	183	Farsang et al. (2018)
Rhodochrosite (Mn):	1727		1415	1086		718		290	185	Farsang et al. (2018)
Calcite (Ca):	vw		vw	s		w		m		
JB1457F	1749		1436	1086		712		281	154	this study
JB1458F	1750		1436	1086		711		281	154	this study
JB1460F	1748		1436	1086		712		281	156	this study
	1751		1438	1088		713		284	158	Farsang et al. (2018)
	1748		1434	1085		711		281	154	Urmos et al. (1991)
Dolomite (Ca,Fe,Mg):	vw		w	s		w		m		
JB1461F	1794		1443	1096		724		297	174	this study
	1759		1442	1098	881	724		301	178	Farsang et al. (2018)
Aragonite (Ca):				s		w		m		
JB1459F				1085		703		206	153	this study
			1463	1085	853		705	208	155	Farsang et al. (2018)
		1573	1461	1083			701	250		Buzgar & Apopei (2009)
		1547	1462	1085	853	705	701	284	153	Urmos et al. (1991)
			1463	1086	854	707	702	285		Krishnamurti (1960)
Strontianite (Sr):										
		1543	1445	1069			700	242		Buzgar & Apopei (2009)
			1447	1074	855	711	701	246		Krishnamurti (1960)
Witherite (Ba):										
		1511	1422	1059			693	227		Buzgar & Apopei (2009)
			1421	1061	852	699	691	227		Krishnamurti (1960)
Natrite (Na):										
			1429	1080		702		290		Buzgar & Apopei (2009)
K2CO3										
		1426	1374	1063		702	677	237		Buzgar & Apopei (2009)

b. Nitrates

Sample #	$\nu_1+\nu_4$	ν_3	ν_1	ν_2	ν_4	lattice-L	lattice-T	Source
LiNO3	vw	w	s		w	m		
JB1583	1675	1383	1069		734	236	122	this study
NaNO3								
JB0997A	vw	w	s		vw	m		
JB1584B	1669	1385	1067		724	186		this study
Sr(NO3)2	vw	vw	s		w	m		

Table 6
Continued

b. Nitrates								
Sample #	$\nu_1+\nu_4$	ν_3	ν_1	ν_2	ν_4	lattice-L	lattice-T	Source
JB1585	1629	1404	1056		737	182	108	this study
Pb(NO3)2	vw	vw	s		vw	m		
JB1587	1611	1335	1046		731	160	123, 95	this study
KNO3		vw	s		vw	vw		
JB998A		1358, 1344	1050		715	138		this study

Note. s, m, w, and vw refer to strong, medium, weak, and very weak bands.

vibrations and the larger cations have lower frequency vibrations. If these band positions depended only on the size of the cation, then smithsonite (Zn^{2+}) would be expected to have a vibration between that of magnesite and siderite. Therefore, other factors must be contributing to the vibrational energies for smithsonite. Potential other effects could include the cation's ability to accept electrons. In the case of Zn^{2+}, the addition of two electrons would fill the *d* orbital and form a stable electron shell, so Zn^{2+} may pull the electrons from the oxygen atom in the CO_2^{2-} group closer to it than expected based on its size, creating a tighter Zn-O bond and looser C-O bond and lower CO_2^{2-} vibrational frequency. The ν_3 and ν_2 vibrations and the lattice mode have the strongest bands for the calcite-type spectra. The ν_1 vibration is not observed at all in emissivity spectra of these samples and the ν_4 vibration is tiny and shaped in an upward/downward derivative-type (zigzag) pattern due to anomalous dispersion that is enhanced for smaller particle sizes. The shape of the ν_3 band includes the greatest band depth near 1,500–1,600 cm^{-1}, with a much weaker shoulder near 1,400 cm^{-1}, which is closer to where the ν_3 vibration is observed in transmittance spectra of calcite-type carbonates (Weir & Lippincott, 1961; White, 1974). Specific molecular oscillators for calcite are identified in Lane (1999). The ν_3 band center in emission spectra varies from 1,572 cm^{-1} for magnesite to 1,523 cm^{-1} for calcite among the 6-fold single-cation trigonal structure carbonates, occurs near 1,530–1,550 cm^{-1} for

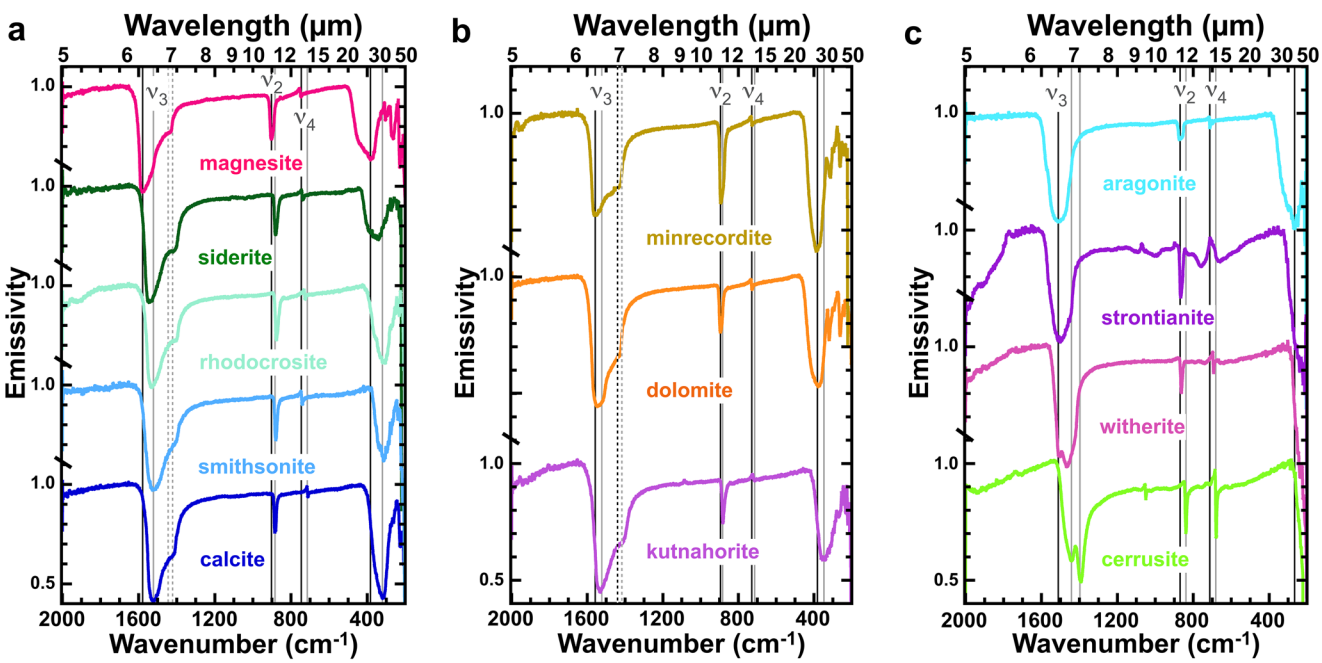

Figure 4. Emissivity spectra of coarse-grained carbonates. (a) Spectra of the 6-fold single-cation calcite-type minerals with trigonal structure: magnesite, siderite, rhodochrosite, smithsonite, and calcite. (b) Spectra of the 6-fold multiple cation dolomite-type minerals with trigonal structure: minrecordite, dolomite, and kutnahorite. (c) Spectra of the 9-fold aragonite-type minerals with orthorhombic structure: aragonite, strontianite, witherite, and cerussite. Some spectra multiplied to facilitate comparison of the spectral features. Data from Lane and Christensen (1997) and Lane and Bishop (2019).

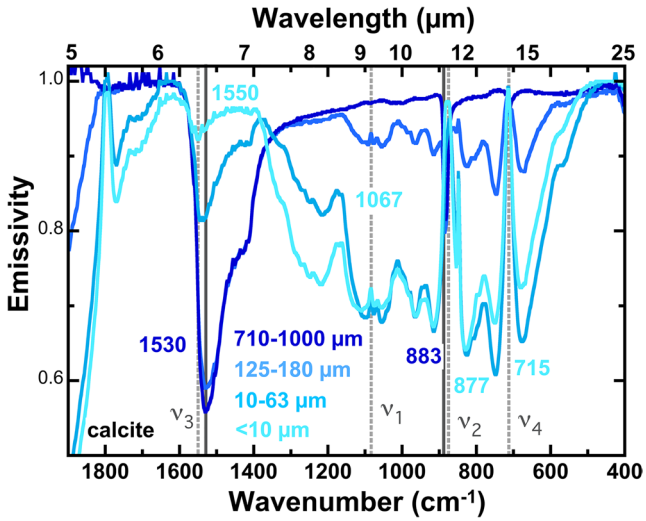

Figure 5. Mid-IR emissivity spectra of different size fractions of calcite. Solid lines mark the bands for the coarsest fractions, while dotted lines mark the bands/peaks for the finest fractions (adapted from Lane & Christensen, 1998).

the 6-fold multiple cation dolomite-type minerals with trigonal structure, and varies from 1,505 cm^{-1} for aragonite to a doublet near 1,440 and 1,394 cm^{-1} for cerussite among the 9-fold minerals with orthorhombic structure.

Figure 4b includes emissivity spectra of multiple cation dolomite-type trigonal structure samples including minrecordite, dolomite, and kutnahorite. These spectra are similar to the calcite-type spectra, but the shape of the ν_3 band is closer to a doublet with a relatively stronger ~1,400 cm^{-1} component compared to the deepest part of the band near 1,550 cm^{-1}. For the aragonite-type orthorhombic structure samples, spectra of aragonite, strontianite, witherite, and cerussite are shown in Figure 4c. The band center for the ν_3 vibration correlates well with cation size for aragonite (Ca^{2+}), strontianite (Sr^{2+}), and witherite (Ba^{2+}), but occurs at a lower wavenumber for cerussite (Pb^{2+}). For these aragonite-group spectra, the ν_3 vibration occurs as a single band or as a doublet much closer together in intensity and wavenumber (~40–50 cm^{-1}) than the features observed for the calcite-group spectra, where the shoulder occurs at lower wavenumbers and is offset by 100 cm^{-1} or more. In addition, a weak ν_1 band is observed for strontianite and cerussite and the ν_4 band is also typically stronger than in the spectra of calcite-group spectra. The additional structure in the strontianite spectrum and the lower emissivity above ~1,800 cm^{-1} differ from the other aragonite-type examples and are due to the onset of volume scattering effects that are related to decreased particle size (e.g., Lane & Christensen, 1998). This is termed Type II behavior in Lane (1999).

The size of carbonate grains (particles) plays an important role in the position and shape of their spectral features in emission and reflectance spectroscopy (Lane, 1999; Lane & Christensen, 1998; Salisbury & Wald, 1992). Spectral features for all minerals change shape when the particle size approaches the wavelength of the vibration (e.g., Aronson et al., 1966; Hunt & Vincent, 1968; Lyon, 1964; Moersch & Christensen, 1995; Mustard & Hays, 1997). Mineral hand samples or mineral grains larger than ~500 μm typically behave as a consolidated sample with respect to the wavelength of light in infrared emission and reflectance spectroscopy and the spectral features of these coarse-grained minerals are dominated by surface scattering. In contrast, as the particle size decreases, the number of grain to air interfaces increases per unit volume, causing an increase in porosity and internal volume scattering of light. Thus, surface scattering dominates the spectral properties of mineral hand samples, rocks, and large particles, while volume scattering dominates the spectral properties of small particles or mineral grains.

Additionally, scattering of light in particulate mineral samples also depends on the difference between the optical properties of the mineral and the air (or other gas filling pore spaces). The real (n) and imaginary (k) indices of refraction control whether bands are observed in the spectra for mineral vibrations. Typically, an emissivity minimum or reflectance maximum is observed when n is small and k is large for coherent scattering termed "Type I" (Hunt & Vincent, 1968) or "Class 1" (Moersch & Christensen, 1995) behavior. Type I scattering is observed for the ν_3 band in carbonates and this band always occurs as an emissivity minimum or reflectance maximum, although the strength of the band varies with particle size. A different case occurs for the ν_2 and ν_4 vibrations in carbonates because these bands follow "Type II/Class 2" behavior (Hunt & Vincent, 1968; Moersch & Christensen, 1995) and have a small value of n but only somewhat large value of k, resulting in lower absorption coefficients compared to the ν_3 vibration. For these vibrations, the spectral bands invert direction once the grain size decreases past a critical threshold where the particles become optically thin rather than optically thick (Lane, 1999). This trend is observed in Figure 5 for emissivity spectra of calcite, where the ν_3 band depth decreases with decreasing particle size, but remains as an emissivity minimum, while the ν_2 and ν_4 vibrations flip direction for the smaller particle sizes, occurring as peaks instead of dips in emissivity.

The contributions of n and k to both the shape and direction of the fundamental vibrations of minerals govern the differences between emissivity and reflectance spectra versus transmittance spectra (e.g., Lane & Bishop, 2019). For transmittance spectra the absorptions are controlled by the absorption coefficient that

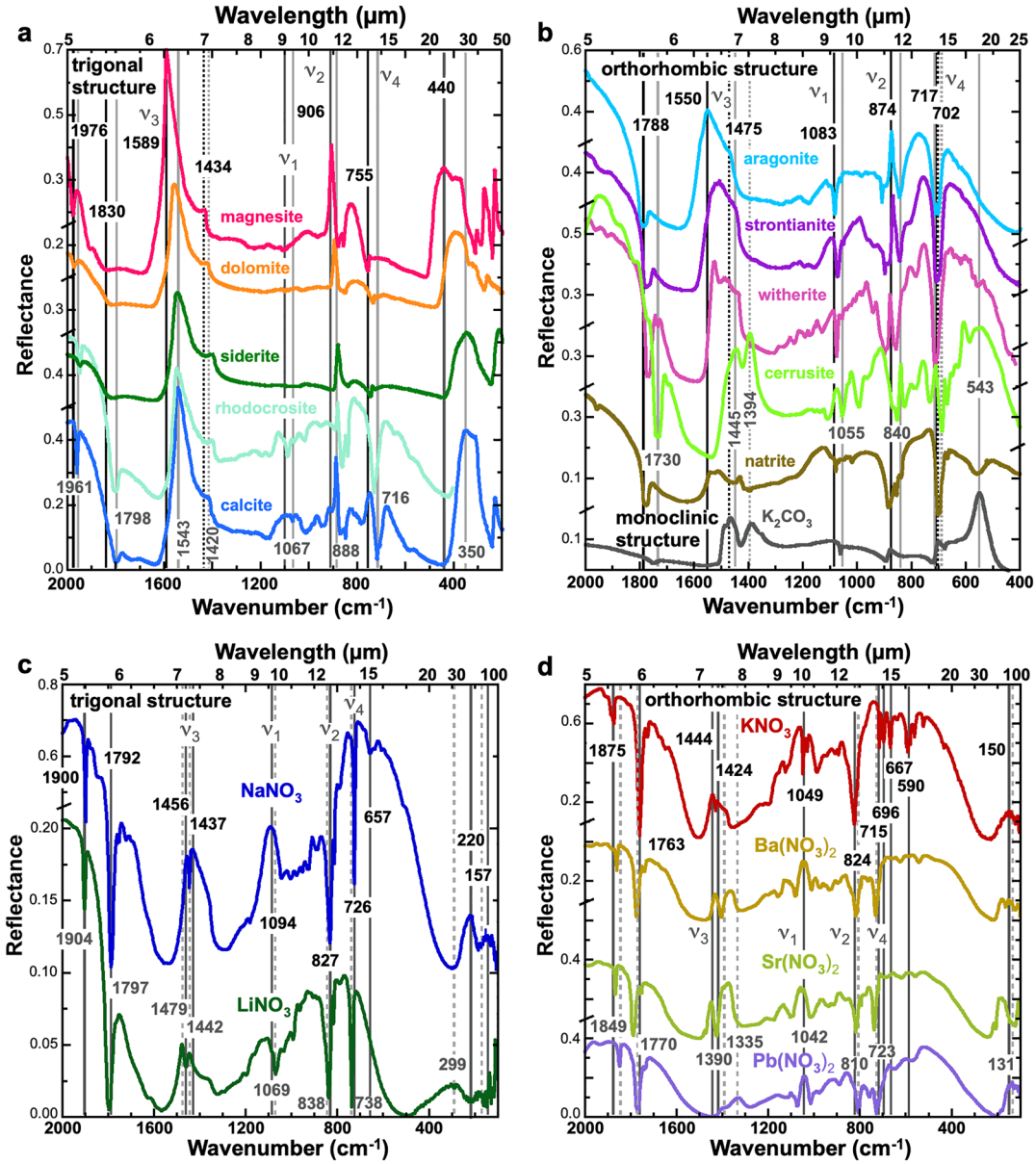

Figure 6. Mid-IR reflectance spectra of carbonates and nitrates. (a) Spectra of the 6-fold calcite/dolomite-type carbonates: magnesite, dolomite, siderite, rhodochrosite, and calcite. (b) Spectra of the 9-fold aragonite-type carbonates: aragonite, strontianite, witherite, and cerussite, as well as the alkali carbonates natrite and K_2CO_3. (c) Spectra of the 6-fold calcite-type nitrates: $NaNO_3$ and $LiNO_3$. (d) Spectra of the 9-fold aragonite-type nitrates: KNO_3, $Ba(NO_3)_2$, $Sr(NO_3)_2$, and $Pb(NO_3)_2$. The carbonates have a particle size of 90–125 or <125 μm and the nitrates have <125 μm particle size. Cerussite is an exception with a particle size range of 74–250 μm (from Salisbury et al., 1991). The strontianite and witherite spectra are from the USGS spectral library and all other samples were measured at RELAB. The band centers are marked by gray lines, where solid lines refer to the bands in the top spectrum and dashed lines refer to the spectrum at the bottom in each group.

depends on k alone, which produces differences between some mineral spectra in transmittance versus reflectance and emissivity spectra. In the case of carbonates, band ν_3 occurs at a shorter wavelength (~6–7 μm) than the other fundamental vibrations (~9–15 μm) and surface scattering is most important, which is controlled by n. Bands ν_2 and ν_4 occur at longer wavelengths and volume scattering is initially more dominant as particle size decreases, which is largely dependent on k. For these reasons, the bands for the ν_2 and ν_4 vibrations are more likely to flip direction than the band for the ν_3 vibration in spectra of minerals.

Table 7
Fundamental Band Centers Measured in Wavenumbers (cm^{-1}) for Carbonates and Nitrates

a. Carbonates with trigonal rhombohedral structure, 6-fold symmetry, and smaller cations

Sample #	Grain size	$\nu_1+\nu_2$	$\nu_1+\nu_4$	ν_3'	ν_3	ν_1	ν_2	ν_4	ν_4'	Lattice
Magnesite (Mg):										
JB0946E	<125 μm	1976	1830	1589	1434	1105	906	755		380
JB1161B	45–125 μm	1977	1828	1589	1431	1106	906	756		374, 239
					1478	~1087	892	749		Transmittance
Mg-siderite (Fe/Mg):										
JB1162B	45–125 μm	1957	1816	1559	1419	1091	889	748		395, 260
Siderite (Fe):										
JB1163B	45–125 μm	1946	1811	1540	~1410	1101	879	744		350, 247
JB1462D	90–125 μm	1954	1814	1558	1408	1090	887	745		398, ~260
JB1463D	90–125 μm	1947	1810	1544	1403	1087	880	744		342, 245
					1470	~1087	869	738		Transmittance
Rhodocrosite (Mn):										
HS67	<250 μm	1948	1802	1547	1402	1088	881	731		
HS338	74–250 μm	1948	1807	1545	1403	1087	879	732		
					1480	~1087	870	728		Transmittance
Mg-calcite (Ca/Mg):										
JB0825	~<250 μm	1962	1795	1574	1417	1084	870	720		~325
JB0826	~<250 μm	1963	1797	1586	1419	1086	873	723		~320
JB0827	~<250 μm	1963	1796	1584	1420	1086	873	724		~320
Calcite (Ca):										
JB0551	90–125 μm	1959	1798	1537	~1425	1065	885	714		
JB1457D	90–125 μm	1960	1798	1543	~1420	1068	888	715		349, 227
JB1458D	90–125 μm	1961	1798	1543	~1420	1067	888	716		350, 228
JB1460	90–125 μm	1961	1798	1546	~1425	1084	889	717		351, 227
HS194B	74–250 μm	1961	1800	1539	~1420	1068	887	717		
					1432	1087	881	712		Transmittance

b. Carbonates with trigonal rhombohedral structure, 6-fold symmetry, and mixed cations

Sample #	Grain size/ Sample info	$\nu_1+\nu_2$	$\nu_1+\nu_4$	ν_3'	ν_3	ν_1	ν_2	ν_4	ν_4'	Lattice
Dolomite (Ca,Fe,Mg):										
JB1461D	90–125 μm	1972	1817	1559	1424	1098	895	733		398, 155
JB0779	<125 μm	1974	1817	1568	1425	1099	898	732		399, 154
HS102B	74–250 μm	1975	1821	1568	1427	1101	897	735		402
					1480	~1087	883	730		Transmittance
Ankerite (Ca,Fe,Mg,Mn):										
JB0778	<125 μm	1869	1796	1564	1446	1017	875	714	698	405, 233, 151
JB0832	~<250 μm		1787		1411	1083	886	715	702	
JB0833	~<250 μm		1788		1413	1083	885	715	702	
Fe-Ca-Mg carbonates:										
JB0829	~<250 μm	~1955	1798		1392	1081	873	736		~310
JB0830	~<250 μm	~1955	1797		1393	1080	875	733		~310
JB0831	~<250 μm	~1955	1796		1391	1080	872	731		~320

Table 7
continued

c. Carbonates with orthorhombic structure, 9-fold symmetry, and larger cations

Sample #	Grain size	$\nu_1+\nu_2$	$\nu_1+\nu_4$	ν_3'	ν_3	ν_1	ν_2	ν_4	ν_4'	Lattice
Aragonite (Ca):										
JB1459D	90–125 μm		1788	1550	~1475	1083	874	717	702	285, 268
JB1640	90–125 μm		1788	1549	~1475	1083	873	717	702	286, 268
JB1659	<125 μm		1787	1549	~1480	1083	875	715	700	286, 268
NMNH B10083	74–250 μm		1789	1528	~1475	1084	875	718	702	
				1550	1430	1087	866	715	703	Transmittance
Strontianite (Sr):										
JB1658	<125 μm		1787	1549	~1475	1083	875	715	700	413, 269
HS272	74–250 μm	1925	1776	1507	~1450	1072	868	710	703	
					1496	1074	863, 845	707	701	Transmittance
Witherite (Ba):										
HS273	74–250 μm	1962	1769	1525	~1445	1075	879	713	705	556
					1470	1060	858, 845	709	695	Transmittance
Cerussite (Pb):										
Vergo-2	74–250 μm		1730	1445	1394	1055	840	711	688	543
					1450	1053	840, 826	678	670	Transmittance

d. Carbonates with monoclinic structure and alkali cations

Sample #	Grain size	$\nu_1+\nu_2$	$\nu_1+\nu_4$	ν_3'	ν_3	ν_1	ν_2	ν_4	ν_4'	Lattice
Natrite (Na):										
JB1744	<250 μm	1957	1776	1540	1431	1078	885	703	696	559
Potassium carbonate (K):										
JB1745	<250 μm		1745	1485	1388	1061	894	721	701	549

e. Nitrates with trigonal rhombohedral structure, 6-fold symmetry, and smaller cations

Sample #	Grain size	$\nu_1+\nu_2$	$\nu_1+\nu_4$	ν_3'	ν_3	ν_1	ν_2	ν_4	ν_4'	Lattice
$Al(NO_3)_3 \cdot 9H_2O$										
JB0994A	<125 μm			1355		1046	816	720		~460
$Fe(NO_3)_3 \cdot 9H_2O$										
JB0995A	<125 μm			1382	1275	~1047	837	733		565, 419
JB1579B	<250 μm			1399	1290	1057	837	732		567, 419
$Mg(NO_3)_2 \cdot 9H_2O$										
JB0996A	<125 μm	1880	1799	1469	1356	1057	832	733		589, 454, 304
$Cu(NO_3)_2 \cdot 3H_2O$										
JB1580	<250 μm			1346	1281	1051	~837	731		600, 488, 326
$Zn(NO_3)_2 \cdot 6H_2O$										
JB1581	<250 μm			1410	1359	1057	833	739		578, 420, 231
$LiNO_3$										
JB1583	<250 μm	1904	1797	1479	1442	1069	838	738		291, 156
					1420	1068	843	738		Transmittance
$NaNO_3$										
JB0997A	<125 μm	1900	1788	1456	1433	1092	833	726		657, 299, 154
JB1584B	<250 μm	1900	1792	1456	1437	1094	827	726		657, 299, 157
					1395	1068	838	727		Transmittance

Table 7
continued

f. Nitrates with orthorhombic structure, 9-fold symmetry, and larger cations

Sample #	Grain size	$\nu_1+\nu_2$	$\nu_1+\nu_4$	ν_3'	ν_3	ν_1	ν_2	ν_4	ν_4'	Lattice
$Ca(NO_3)_2 \cdot 4H_2O$										
JB1578	<250 μm	1874	1802, 1783	~1455	1412	1059	824	748		611, 328, 232
$Sr(NO_3)_2$										
JB1585	<250 μm	1868	1792	1448	1384	1059	820	741		619, 559, 180
$Pb(NO_3)_2$										
JB1587	<250 μm	1849	1775	~1390	1335	1042	810	731	723	648, 579, 131
$Ba(NO_3)_2$										
JB1586	<250 μm	1861	1778	1427	1371	1051	821	733		656, 543, 178
KNO_3										
JB998A	<125 μm	1875	1763	1444	1424	1049	824	715	696	667, 590, 150
					1420	1050	827	714		Transmittance
NH_4NO_3										
JB1582A	<125 μm	1867	1757	1446	1346	1065	833	717		

Note. All band centers determined from reflectance spectra in this study; black numbers refer to upward peaks, blue numbers refer to downward bands, and red numbers indicate transmittance peaks from Weir and Lippincott (1961).

4.3. Mid-IR Reflectance Spectra

Reflectivity (R) and emissivity (E) are related by Kirchhoff's Law where $R = 1 - E$ under optimal circumstances (e.g., hemispherical or bidirectional off-axis reflectance), but in practice differences generally occur between reflectance spectra and emissivity spectra, especially for smooth surfaces or small particles (e.g., Lane & Bishop, 2019). Emissivity spectra can be measured of planetary surfaces in the mid-IR range but reflectance can only be measured at solar wavelengths. For this reason, reflectance spectra must be converted to emissivity spectra for comparison with remote sensing data. Reflectance spectra are typically easier to acquire in the lab and the spectra provide similar shapes and identical trends to emissivity spectra and thus can provide important information for planetary spectroscopy.

Mid-IR reflectance spectra are shown in Figure 6 for selected carbonates and nitrates. Spectra are offset for clarity and arranged in order of the wavelength positions of their ν_3 bands. Overall, similar patterns were observed for the fundamental vibrations of carbonates and nitrates, with the nitrate bands occurring at smaller wavenumbers (or longer wavelengths) than their associated carbonate bands. The ν_3 band is often observed as a doublet or main band with a shoulder in reflectance or emissivity spectra, while only one band is observed in transmittance spectra. Band centers were recorded for the reflectance spectra of these samples and both the band centers were provided where two bands were observed (Table 7). These two bands are termed ν_3' and ν_3, where ν_3' refers to the higher wavenumber (cm^{-1}) or shorter wavelength (μm) band and ν_3 refers to the band that is more similar to that observed in transmittance spectra.

Examples of the trigonal structure single cation calcite-type and multiple cation dolomite-type carbonates are grouped together in Figure 6a. The ν_3 band centers occur at 1,589 and 1,434 cm^{-1} for magnesite and at 1,543 and 1,420 cm^{-1} for calcite. The ν_3 band centers fall in between this range for the other trigonal structure carbonates and follow a trend of decreasing wavenumber (or increasing wavelength) from Mg^{2+} to Fe^{2+} to Mn^{2+} to Ca^{2+} as expected based on the size of the effective ionic radii (Table 2, Figure S1). Similarly, the ν_2 and ν_4 band centers shift from 906 and 755 cm^{-1} for magnesite to 888 and 716 cm^{-1} for calcite, and the primary lattice mode for magnesite occurs at 440 cm^{-1} and is shifted toward smaller wavenumbers (or longer wavelengths) for calcite. The ν_1 band is observed only weakly, if at all, in reflectance spectra of trigonal structure carbonates. A full list of band centers is given in Table 7 for the mid-IR fundamental vibrations and lattice modes of the carbonates and nitrates studied here.

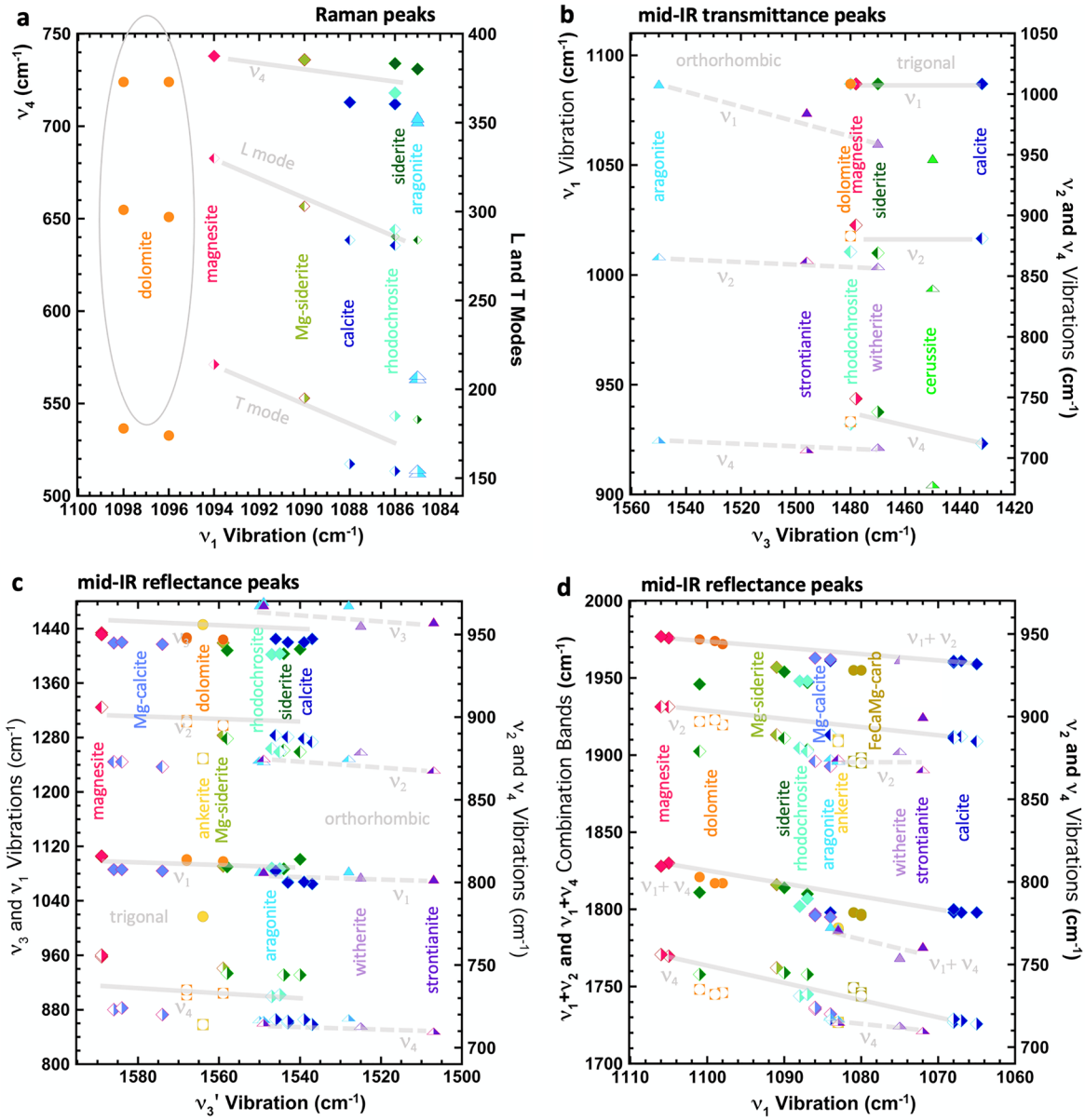

Figure 7. Raman and IR carbonate bands versus structure and chemistry. (a) Comparison of the strongest Raman peaks due to the ν_1 stretching vibration and the *L* and *T* modes for several trigonal carbonates and aragonite. (b) Comparison of the mid-IR transmittance bands due to the ν_3, ν_1, ν_2, and ν_4 fundamental vibrations for several trigonal and orthorhombic carbonates. (c) Comparison of the mid-IR reflectance bands due to the ν_3', ν_3, ν_1, ν_2, and ν_4 fundamental vibrations for several trigonal and orthorhombic carbonates. (d) Comparison of the mid-IR reflectance bands due to the $\nu_1 + \nu_2$ and $\nu_1 + \nu_4$ combination bands and the ν_1, ν_2, and ν_4 fundamental vibrations for several trigonal and orthorhombic carbonates. Note that the cerussite data is off the scale for this panel and not shown. In each case the calcite group minerals are marked by diamonds, the dolomite group minerals by circles, and the aragonite group minerals by triangles. Due to the large quantity of reflectance data in panels c and d, filled shapes are used for the left *y*-axis values and open or partially open shapes are used for the right *y*-axis values in order to help differentiate these values. Solid gray lines mark trends in the calcite group minerals, while dashed gray lines mark trends in the aragonite group minerals.

Reflectance spectra (not shown) were also acquired of several additional carbonates with mixed cations, including a high Mg dolomite, an Fe-bearing dolomite, a Mg-bearing siderite, and a Mg-bearing calcite. Many of these fall in the dolomite category with a mixture of Ca, Fe, and Mg cations. The band centers occurred at larger wavenumbers for the dolomite spectra that contain more Mg and at smaller wavenumbers for the samples with higher Fe abundance (Table 7). As expected, spectra of the Mg-bearing siderite and Mg-bearing calcite showed that the band centers for these mixed cation carbonates (Table 7) occurred at higher values than in the spectra of siderite and calcite, respectively.

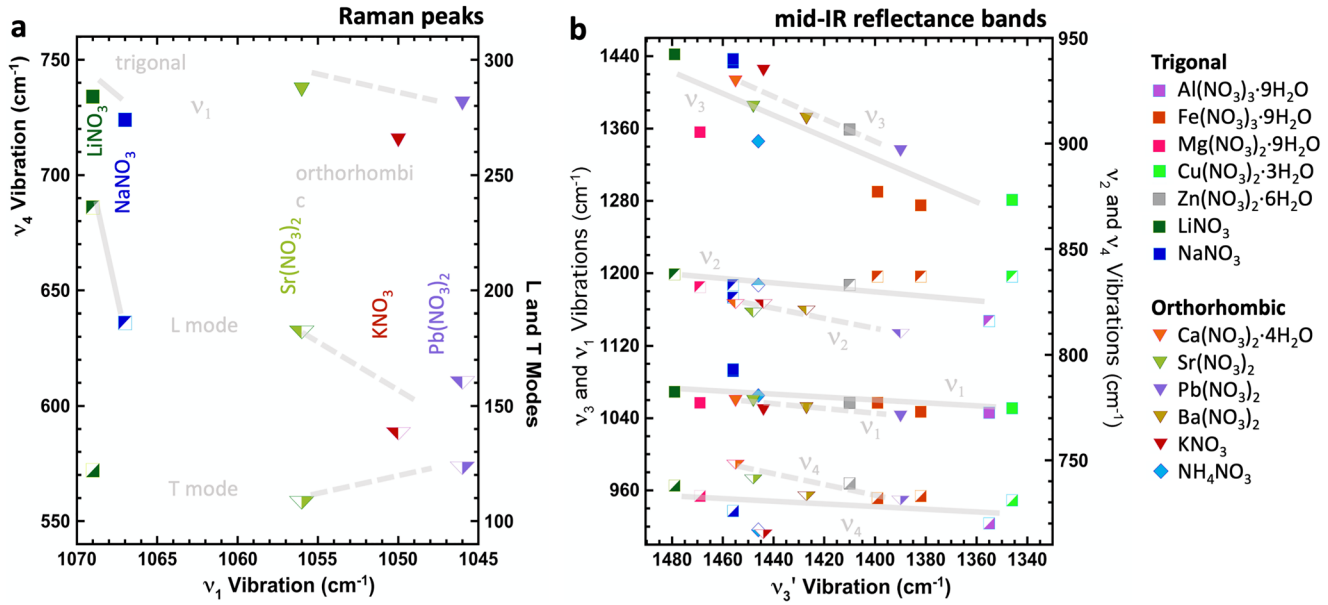

Figure 8. Raman and IR nitrate bands versus structure and chemistry. (a) Comparison of the strongest Raman peaks due to the ν_1 stretching vibration and the *L* and *T* modes for several trigonal and orthorhombic nitrates. (b) Comparison of the mid-IR reflectance bands due to the ν_3', ν_3, ν_1, ν_2, and ν_4 fundamental vibrations for several trigonal and orthorhombic nitrates. In each case the trigonal structure nitrates are marked by squares and the orthorhombic structure nitrates by triangles. Ammonium nitrate is marked with diamonds. Solid gray lines mark trends in the trigonal minerals, while dashed gray lines mark trends in the orthorhombic minerals.

Carbonates with orthorhombic structure illustrate a similar trend in band centers shifting toward smaller wavenumbers (or longer wavelengths) as the effective ionic radii of the cations increases, with the exception of cerussite (Figure S1). As observed in the emissivity spectra (Figure 4c), the shape of the ν_3 band in spectra of aragonite-type carbonates is more comparable to an asymmetric band than a doublet. The ν_1 bands were clearly present for these orthorhombic carbonates and complex features were often observed for the ν_2 and ν_4 bands. The lattice modes were present at lower wavenumbers that were often only partially observed due to the wavenumber constraints of the beam splitter at 200 cm^{-1} that cut off these bands.

Reflectance spectra of the alkali carbonates with monoclinic structures (i.e., natrite [sodium carbonate] and potassium carbonate; Figure 6b) have a clear doublet of roughly equal intensity for the ν_3 bands, and include bands for the ν_1 vibration and also the lattice mode. The band positions for spectra of sodium and potassium carbonates follow the expected trends of decreasing wavenumbers for K^+, which has a larger effective ionic radius than Na^+ (Figure S1).

Reflectance spectra were measured of several trigonal structure nitrates, but many of these were hydrated and exhibited weaker NO_3 bands. Reflectance spectra are shown for lithium (Li) nitrate and sodium (Na) nitrate in Figure 6c, where the ν_3 band centers occur at 1,479 and 1,442 cm^{-1} for the Li^+ form and at 1,456 and 1,437 cm^{-1} for the Na^+ form, following the trend observed for carbonates where band centers shift toward smaller wavenumber values for larger cations. Reflectance spectra of ammonium nitrate (not shown) include the ν_3 doublet at 1,446 and 1,346 cm^{-1}, following the expected trend of decreasing frequency with increasing cation size because the effective ionic radius of NH_4^+ is larger than that of Na^+. The shape of the ν_3 bands in these nitrate spectra are different from the ν_3 bands in trigonal carbonate spectra, instead occurring as doublets with similar intensities and closer vibrational energies than observed for the carbonates. Bands were observed for the ν_1, ν_2, and ν_4 vibrations and also lattice modes for the trigonal structure nitrates (Table 7). Spectra of the orthorhombic nitrates (Figure 6d) are similar to spectra of the orthorhombic carbonates with parallel trends for all of the vibrations. The band positions for Pb nitrate also occur at smaller wavenumbers, as observed for Pb carbonate. Band centers listed in Table 7 are primarily for the reflectance spectra measured in this study, but are provided for transmittance spectra from the literature as well, when available.

4.4. Variations in the Fundamental Vibrations With Chemistry

The wavenumbers of the strongest bands in Raman, mid-IR transmittance, and mid-IR reflectance spectra exhibit trends with carbonate chemistry and structure (Figure 7). In Raman spectra the ν_1 band is strongest, in contrast to a stronger ν_3 band in mid-IR spectra. The position of this ν_1 band is compared with the positions of the ν_4 band and the L and T lattice modes in Figure 7a. These data are somewhat scattered and do not demonstrate clear trends in band position for ν_4, L, or T with ν_1. This illustrates that ν_1 vibrational energies are more complex than ν_3 vibrational energies and do not relate as directly to the effective ionic radii of the cations. The ν_1 values for dolomite-type carbonates cluster at higher wavenumbers, followed by magnesite, then calcite, and then finally by rhodochrosite and siderite with similar values at lower wavenumbers.

As observed for emissivity and reflectance spectra, the ν_3 band is strongest for transmittance spectra. The frequencies of the ν_1, ν_2, and ν_4 bands in transmittance spectra typically occurred at lower energies than expected relative to the reflectance and emission spectra, and the ν_3 position in transmittance spectra typically occurs between the values of the ν_3' and ν_3 bands in reflectance spectra (Table 7). The ν_3 band center in transmittance spectra is compared in Figure 7b with the band centers for the ν_1, ν_2, and ν_4 vibrations, when present, using values reported by Weir and Lippincott (1961) for several carbonate minerals and in Böttcher et al. (1992) for rhodochrosite. Different trends were observed for the trigonal carbonates and orthorhombic carbonates and in general the ν_3 vibrations of the orthorhombic carbonates occurred at a higher wavenumber than the ν_3 vibrations of the trigonal carbonates with the same or similar cations. For the calcite-type trigonal structure carbonates the ν_1 and ν_2 band positions did not vary much with decreasing ν_3 band position, but the ν_4 band values decreased with decreasing ν_3 band values from magnesite to siderite to calcite. For the aragonite-type orthorhombic structures the ν_1 band decreased in energy corresponding to decreasing energy of the ν_3 band and size of the effective ionic radii of the cation (Figure S1); however, the energies of the ν_2 and ν_4 bands followed this trend to a lesser degree and their band positions varied only slightly from aragonite to strontianite to witherite. For cerussite, the values of ν_2, and ν_4 occurred at lower energies than expected relative to the other orthorhombic carbonates, which may be due to the electronic configuration of the Pb^{2+} cation.

A larger number of reflectance spectra was available for comparison in this study. These data are given in Figure 7c for the band positions of ν_3' (higher wavenumber band of the ν_3 doublet) compared to the other fundamental vibrations, and in Figure 7d for the ν_1 band positions compared to the ν_2 and ν_4 band positions as well as the $\nu_1 + \nu_2$ and $\nu_1 + \nu_4$ combination band positions. Similar trends were observed for the band positions of the ν_3' band in emissivity and reflectance spectra and the ν_3 band position in transmittance spectra compared to the effective ionic radii of the cations in the carbonates (Figure S1). The band positions were most consistent for magnesite-siderite-rhodocrosite-calcite in the trigonal structure carbonates, for aragonite-strontianite-witherite in the orthorhombic carbonates, and for natrite and potassium carbonate in the monoclinic alkali carbonates. Carbonates containing Zn^{2+} (smithsonite) and Pb^{2+} (cerussite) did not follow these trends, likely due to the electronic structures of these cations. For the trigonal carbonates a trend of slightly decreasing ν_3 and ν_1 vibrational energies was observed with decreasing ν_3' values, but the ν_2 and ν_4 trends are a bit scattered indicating a more complex association. For the orthorhombic carbonates, similar trends in slightly decreasing ν_3, ν_1, ν_2, and ν_4 band energies are observed with decreasing energies, following the expected trends for aragonite, strontianite, and witherite. The data for cerussite is not included because those bands all occur at much lower values and are off the scale of the plot. In general, the ν_2 and ν_4 band positions for aragonite group carbonates occur at lower energies than these bands for calcite group carbonates. In contrast to the ν_3 and ν_3' vibrational energies that are separated for the trigonal and orthorhombic carbonates, the ν_1 vibrational energies overlap for both groups, but the ν_1 band positions within each group are generally consistent with the effective ionic radii of the cations in the carbonates. In Figure 7d consistent trends in decreasing wavenumber are observed for the ν_2 and ν_4 bands with decreasing wavenumber of the ν_1 band for the trigonal structure carbonates. Similar lines are observed as well for the combination bands due to $\nu_1 + \nu_2$ and $\nu_1 + \nu_4$, providing confidence in these band assignments. For the calcite group these combination bands vary as expected from magnesite to siderite to rhodochrosite to calcite and the mixed cation dolomite group carbonates fall in the middle of this range. For the orthorhombic structure carbonates consistent trends are also observed for the ν_2 and ν_4 bands and the $\nu_1 + \nu_4$ combination band, but the $\nu_1 + \nu_2$ combination band is generally absent and if present it is very weak. In fact, this band

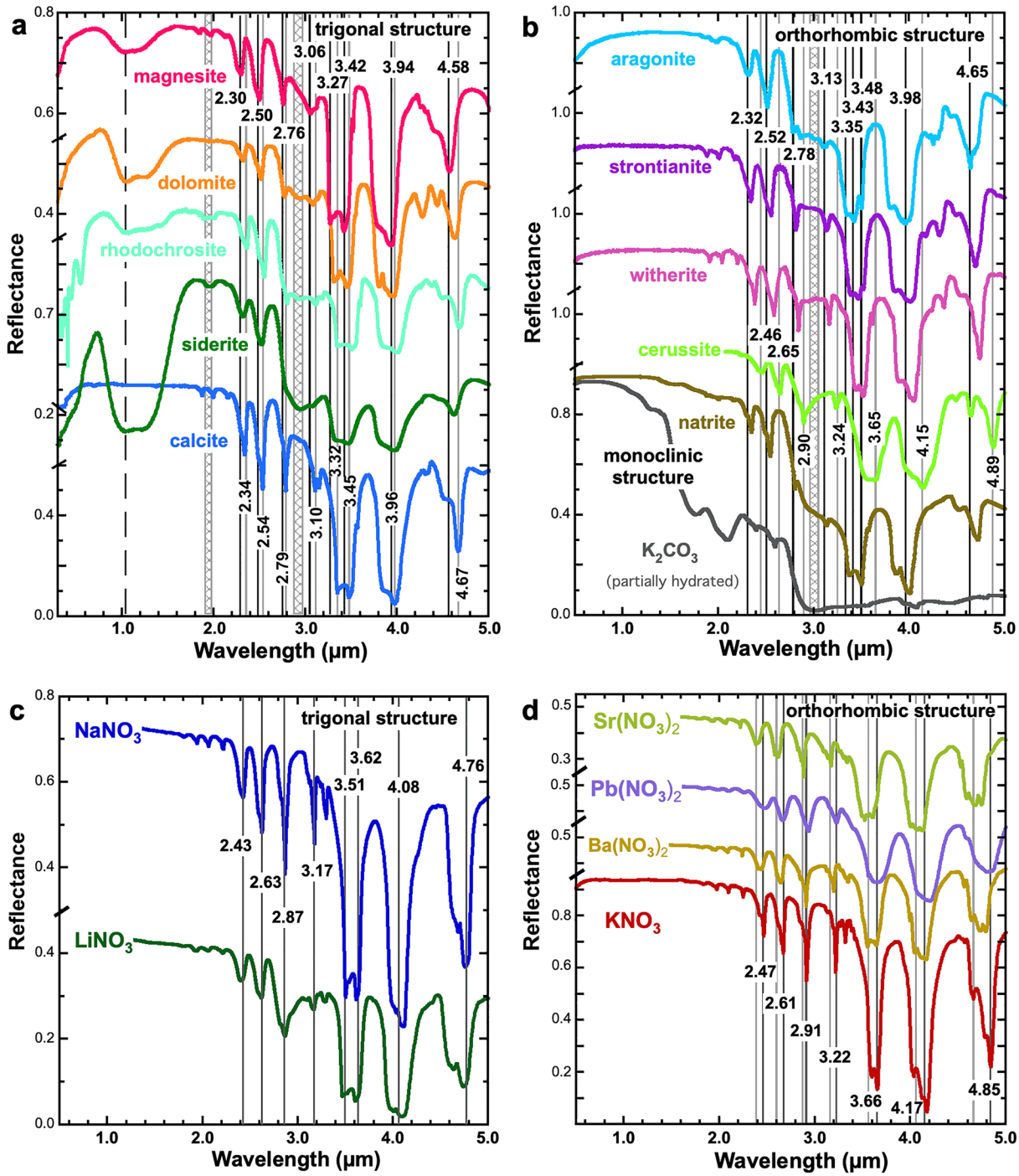

Figure 9. Visible/near-infrared reflectance spectra of carbonates and nitrates. (a) Spectra of the 6-fold calcite/dolomite-type carbonates: magnesite, dolomite, rhodochrosite, siderite, and calcite. (b) Spectra of the 9-fold aragonite-type carbonates: aragonite, strontianite, witherite, and cerussite, as well as the alkali carbonates natrite and K_2CO_3. (c) Spectra of the 6-fold calcite-type nitrates: $NaNO_3$ and $LiNO_3$. (d). Spectra of the 9-fold aragonite-type nitrates: KNO_3, $Sr(NO_3)_2$, $Ba(NO_3)_2$, and $Pb(NO_3)_2$. The carbonates have particle size 90–125 or <125 μm (74–250 μm for cerussite, from Salisbury et al., 1991) and the nitrates have particle size <125 μm. The strontianite and witherite spectra are from the USGS spectral library and all other samples were measured at RELAB. The band centers are marked by gray lines for selected features. The band center values reported are from the continuum-removed data where available, or estimated from the spectra in this figure.

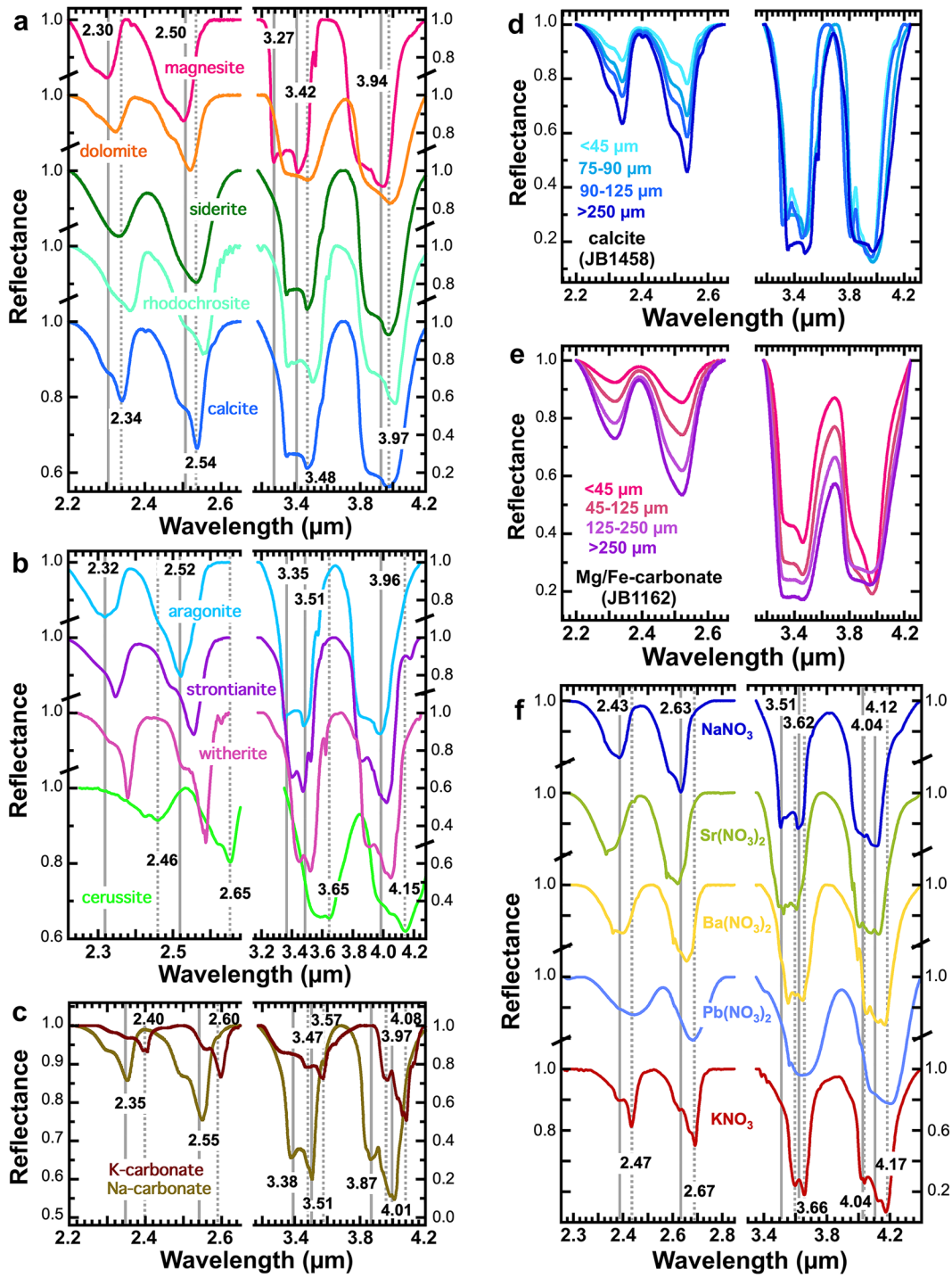

Figure 10. Continuum removed near-infrared reflectance spectra of several carbonates and nitrates with different chemistries. (a) Trigonal structure calcite- and dolomite-type carbonates. (b) Rhombohedral structure aragonite-type carbonates. (c) Alkali carbonates. (d) Multiple grain sizes of calcite. (e) Multiple grain sizes of Mg/Fe-carbonate. (f) Nitrates. Gray lines are drawn to facilitate comparison of the data. Spectra of finer-grained size fractions (<125 or 45–125 μm) were typically used for panels (a, b, c, and f), while multiple size ranges are presented in panels (d and e). The continuum was removed across the regions 2.2–2.65 and 3.175–4.25 μm for the carbonate spectra and across the regions 2.25–2.8, and 3.35–4.4 μm for the nitrate spectra. The cerussite spectra were processed with the nitrate region for continuum removal because the cerussite bands occur at longer wavelengths than in spectra of other carbonates.

could be misidentified in the strontianite spectrum because the observed band position is inconsistent with that of the other carbonates, occurring at a lower than expected wavenumber.

The wavenumbers of the strongest fundamental bands exhibit trends with nitrate chemistry and structure as well (Figure 8). The ν_1 band occurs at higher wavenumbers in Raman spectra for the trigonal structure nitrates than for the orthorhombic structure nitrates (Figure 8a). Apparent trends identified for these data occur from Li^+ to Na^+ for the trigonal nitrates and from Sr^{2+} to K^+ for the orthorhombic nitrates, but bands due to lead nitrate occur lower than expected based on the effective ionic radius of Pb^{2+}. More data are available for reflectance spectra of orthorhombic nitrates in our study than orthorhombic carbonates and thus trends can be more readily determined (Figure 8b). In contrast to the spectra of carbonates, the band positions of the ν_3' vibration overlap for the trigonal and orthorhombic nitrates. Trigonal nitrates display trends of greatly decreasing ν_3 wavenumbers, and slightly decreasing ν_1, ν_2, and ν_4 wavenumbers with decreasing ν_3' values. For the orthorhombic nitrates, trends of greatly decreasing ν_3 and ν_4 wavenumbers and slightly decreasing ν_1 and ν_2 wavenumbers were observed with decreasing ν_3' values. Thus, these correlations indicate that the vibrational energies are internally consistent.

The mid-IR band centers did not correspond as well though with the effective ionic radii for the nitrates as for the carbonates (Figure 8b). However, general trends were consistent for the orthorhombic nitrates such that the frequencies decreased from Ca^{2+} to Sr^{2+} to Ba^{2+}, as expected with their size. The band centers for lead nitrate have the lowest wavenumber values, as observed for carbonates, potentially due to the stable electronic configuration for Pb^{2+}. NH_4^+ is thought to occur as an orthorhombic structure nitrate, although it can form 6-fold or 9-fold structures. The band centers we observed tend to fall closer to the trigonal data than the orthorhombic data, but there is enough spread in these datapoints that it is difficult to assign a specific type based on these data.

Interestingly, for the trigonal structure nitrates the smaller trivalent cations (Al^{3+} and Fe^{3+}) had lower wavenumber values than the intermediate-sized Mg^{2+} and Zn^{2+} cations, and the larger Li^+ and Na^+ cations had the highest wavenumber values. Apparently, the charge on the cations is playing a greater role than the cation size for nitrates in determining the bond strength and thus vibrational frequency. This could be due to the shape of the electronic orbitals or because the nitrate anion has three oxygen atoms sharing only one electron that is available for bonding with the cations. Cu^{2+} was an exception for this trend and copper nitrate has lower wavenumber values, similar to those of the trivalent cations, perhaps due to its electronic configuration.

5. Visible/NIR Reflectance Spectra of Carbonates and Nitrates

5.1. Visible/NIR Spectra

The NIR region is often defined as the wavelengths where volume scattering dominates the spectral properties rather than surface scattering, reflectance is high, and absorptions due to vibrations occur as downward bands. This spectral range includes features due to overtones of the fundamental ν_3, ν_1, ν_2, and ν_4 bands and their combination bands. The VNIR region includes electronic excitations as well due to first transition metals including Fe^{2+}, Mn^{2+}, or Cu^{2+} in carbonate and nitrate minerals. For this study the VNIR region is defined as ~0.3–5 μm. VNIR reflectance spectra of several anhydrous carbonates and nitrates are shown in Figure 9. A large number of spectral features are observed for these minerals, with the strongest carbonate bands occurring near 3.4–3.5 and 3.9–4 μm for most carbonates (Figures 9a and 9b) and near 3.5–3.7 and 4.1–4.2 μm for most nitrates (Figures 9c and 9d).

Salisbury et al. (1987) compared reflectance and transmittance spectra of calcite across the range 2.5–25 μm (400–4,000 cm^{-1}) and emphasized the importance of multiple carbonate overtone and combination bands for remote detection of carbonates. Their study illustrated how bands near 3.4 μm (~2,900 cm^{-1}) and 4 μm (~5,200 cm^{-1}) are much stronger and potentially easier to detect in remote sensing than some of the mid-IR bands. These VNIR reflectance spectra follow trends largely based on the effective ionic radii, as observed for the mid-IR bands; however, lead carbonate and lead nitrate spectral bands occur at longer wavelengths similar to the trend observed in the mid-IR region spectra.

Earth and Space Science
10.1029/2021EA001844

Table 8
Band Centers and Depths for Selected Carbonates and Nitrates From Continuum-Removed Spectra

		Wavelength	Band	Wavelength	Band	Wavelength	Band	Wavelength	Band	Wavelength	Band	Wavelength	Band
Sample #	Grain size	~2.3 μm	Depth	~2.5 μm	Depth	~3.3–3.4 μm	Depth	~3.4–3.5 μm	Depth	~3.8 μm	Depth	~3.9–4.0 μm	Depth
Carbonates with trigonal rhombohedral structure, 6-fold coordination, and smaller cations													
Magnesite (Mg):													
JB0946E	<125 μm	2.301	0.154	2.503	0.268	3.274	0.755	3.420	0.810			3.940	0.883
JB1161B	45–125 μm	2.301	0.424	2.501	0.527			3.420	0.924			3.937	0.896
Mg-siderite (Fe/Mg):													
JB1162B	45–125 μm	2.319	0.346	2.522	0.451			3.459	0.885			3.964	0.808
Siderite (Fe):													
JB1462D	90–125 μm	2.320	0.140	2.525	0.265			3.466	0.680			3.974	0.773
JB1463D	90–125 μm	2.333	0.145	2.534	0.247	3.427	0.838	3.506	0.707			3.964	0.886
JB1163B	45–125 μm	2.334	0.374	2.538	0.488			3.480	0.911			3.983	0.806
Rhodocrosite (Mn):													
HS67	<250 μm	2.363	0.171	2.553	0.286	3.360	0.637	3.512	0.720			4.013	0.833
HS338	N/A	2.360	0.217	2.554	0.402	3.358	0.784	3.510	0.832			4.006	0.875
Mg-calcite (Ca/Mg):													
JB0825	~<250 μm			2.516	0.074			3.462	0.310			3.964	0.575
JB0826	~<250 μm			2.511	0.075	3.376	0.305	3.455	0.334			3.961	0.581
JB0827	~<250 μm			2.514	0.085	3.376	0.334	3.455	0.365			3.961	0.629
Calcite (Ca):													
JB1457D	90–125 μm	2.340	0.260	2.537	0.260	3.352	0.774	3.478	0.821			3.980	0.901
JB1458D	90–125 μm	2.341	0.264	2.537	0.413	3.316	0.739	3.455	0.786	3.810	0.782	3.961	0.856
JB1460D	90–125 μm	2.338	0.201	2.534	0.338	3.427	0.834	3.506	0.723	3.813	0.725	3.961	0.862
HS194B	74–250 μm	2.340	0.242	2.536	0.394	3.351	0.835	3.479	0.850			3.976	0.860
HS48B	74–250 μm	2.338	0.248	2.535	0.384	3.351	0.657	3.479	0.683			3.979	0.734
JB552	125–180 μm	2.342	0.321	2.539	0.517	3.355	0.865	3.477	0.880			3.979	0.898
Carbonates with rhombohedral structure, 6-fold coordination, and mixed cations													
Dolomite (Ca, Fe, Mg):													
JB0779	<125 μm	2.322	0.117	2.516	0.202	3.311	0.639	3.452	0.716	3.807	0.663	3.958	0.814
JB1461D	90–125 μm	2.324	0.097	2.518	0.199	3.316	0.595	3.457	0.688			3.964	0.817
HS102B	74–250 μm	2.325	0.163	2.514	0.298	3.308	0.741	3.449	0.766	3.804	0.750	3.951	0.801
NMNH R12596	74–250 μm	2.324	0.236	2.515	0.389	3.308	0.868	3.451	0.884	3.804	0.862	3.951	0.893
Salisbury/Vergo 3C	74–250 μm	2.322	0.205	2.515	0.337	3.310	0.832	3.451	0.864	3.806	0.845	3.951	0.891
Fe/Mg/Ca-Carbonate:													
JB829	~<250 μm	2.298	0.005	2.514	0.009	3.378	0.140	3.501	0.157			3.992	0.329
JB832	~<250 μm	2.302	0.012	2.507	0.017	3.378	0.215	3.501	0.175			3.964	0.354

Earth and Space Science

10.1029/2021EA001844

Table 8
Continued

Sample #	Grain size	Wavelength ~2.3 μm	Band Depth	Wavelength ~2.5 μm	Band Depth	Wavelength ~3.3–3.4 μm	Band Depth	Wavelength ~3.4–3.5 μm	Band Depth	Wavelength ~3.8 μm	Band Depth	Wavelength ~3.9–4.0 μm	Band Depth
JB833	~<250 μm	2.296	0.052	2.473	0.042	3.376	0.276	3.501	0.190			3.964	0.362
Ankerite (Ca, Fe, Mg, Mn):													
JB0778	<125 μm	2.314	0.046	2.531	0.030	3.414	0.140	3.478	0.164			3.977	0.283
JB0830	~<250 μm	2.306	0.009	2.507	0.017	3.418	0.203	3.501	0.196			3.983	0.392
JB0831	~<250 μm	2.302	0.012	2.507	0.017	3.418	0.204	3.501	0.186			3.983	0.356
Carbonates with orthorhombic structure, 9-fold coordination, and larger cations													
Aragonite (Ca):													
JB1459D	90–125 μm	2.318	0.146	2.522	0.303	3.352	0.840	3.478	0.870			3.980	0.912
JB1640D	90–125 μm	2.318	0.146	2.521	0.311	3.350	0.767	3.506	0.731	3.813	0.735	3.961	0.871
JB1659	<125 μm	2.319	0.092	2.522	0.197	3.351	0.627	3.506	0.575	3.813	0.591	3.964	0.820
NMNH B10083	74–250 μm	2.318	0.116	2.520	0.254	3.349	0.727	3.505	0.667	3.809	0.674	3.957	0.796
Strontianite (Sr):													
JB1658	<125 μm	2.347	0.158	2.556	0.258			3.474	0.819	3.861	0.657	4.023	0.878
HS272	74–250 μm	2.347	0.203	2.555	0.354	3.399	0.811	3.472	0.843	3.857	0.763	4.019	0.868
Cerrusite (Pb):													
Salisbury/Vergo 1C	74–250 μm	2.460	0.086	2.653	0.197	3.588	0.685	3.646	0.692	4.057	0.670	4.147	0.761
Witherite (Ba):													
HS273	74–250 μm	2.379	0.226	2.588	0.345	3.452	0.791	3.522	0.842	3.910	0.712	4.050	0.878
Carbonates with monoclinic stucture, 9-fold coordination, and alkali cations													
Natrite (Na):													
JB1744	<125 μm	2.353	0.081	2.550	0.145	3.377	0.567	3.506	0.708	3.867	0.555	4.010	0.861
Potassium carbonate (K):													
JB1745	<125 μm	2.397	0.047	2.599	0.092	3.468	0.314	3.571	0.415	3.971	0.372	4.083	0.773
Nitrates with trigonal rhombohedral structure and 6-fold coordination													
$LiNO_3$:													
JB1583A	<125 μm	2.402	0.159	2.621	0.236	3.472	0.781	3.606	0.815	4.014	0.895	4.089	0.936
$NaNO_3$:													
JB997A	<125 μm	2.429	0.230	2.627	0.351	3.508	0.866	3.619	0.872	4.039	0.912	4.119	0.959
JB1584A	<125 μm	2.428	0.186	2.627	0.298	3.508	0.826	3.616	0.834	4.039	0.888	4.119	0.947
Nitrates with orthorhombic structure and 9-fold coordination													
$Sr(NO_3)_2$:													
JB1585A	<125 μm	2.386	0.201	2.617	0.297	3.526	0.790	3.608	0.761	4.010	0.875	4.129	0.922
$Pb(NO_3)_2$:													
JB1587A	<125 μm	2.472	0.124	2.665	0.207	3.563	0.578	3.641	0.640			4.206	0.826

Table 8
Continued

Sample #	Grain size	Wavelength ~2.3 μm	Band Depth	Wavelength ~2.5 μm	Band Depth	Wavelength ~3.3–3.4 μm	Band Depth	Wavelength ~3.4–3.5 μm	Band Depth	Wavelength ~3.8 μm	Band Depth	Wavelength ~3.9–4.0 μm	Band Depth
$Ba(NO_3)_2$:													
JB1586A	<125 μm	2.439	0.157	2.646	0.249	3.555	0.773	3.648	0.754	4.054	0.839	4.168	0.913
KNO_3:													
JB998A	<125 μm	2.467	0.188	2.673	0.250	3.599	0.762	3.657	0.822	4.039	0.747	4.175	0.935

Note. Continuum removal was processed across two regions for all spectra using Mr. Prism (Brown & Storrie-Lombardi, 2006): 2.2–2.65 and 3.175–4.25 μm for carbonates, 2.25–2.8 and 3.35–4.4 μm for nitrates.

In order to more accurately determine the band centers of the most prominent NIR bands, we removed the continuum of these spectra using Mr. PRISM software (Brown & Storrie-Lombardi, 2006). The continuum is a curve in the baseline of the spectrum that can induce changes in the apparent position and band depth of spectral features. Removing this continuum better enables comparison of specific band properties among samples. Selected continuum-removed spectra of carbonates are shown in Figure 10 and the band centers and depths for several carbonates are listed in Table 8 to illustrate the trends in these bands with different cations. A full list of all continuum-removed NIR carbonate and nitrate spectra is provided in Table S2.

We prepared several comparison plots for the bands occurring near 2.3, 2.5, 3.4, and 4 μm in order to further investigate patterns of carbonate chemistry and structure using the wavelength positions of the band centers (Figure 11). These bands occur at 2.30, 2.50, 3.42, and 3.94 μm for most magnesites, near 2.33, 2.53, 3.48, and 3.97 μm for siderite, and near 2.34, 2.54, 3.47, and 3.97 μm for calcite (Figures 9–11, Table 8). These bands near 2.3 and 2.5 μm are consistent with previous measurements of carbonate minerals (Gaffey, 1987; Hunt & Salisbury, 1971). Rhodochrosite does not follow the expected trend, based on the effective ionic radius of Mn^{2+}, for these bands because they appear at longer wavelengths (2.36, 2.55, 3.51, 4.01 μm). Gaffey (1987) observed the rhodochrosite band at 2.37 μm without removing the continuum, which is close to our continuum-removed value of 2.36 μm. The band near 3.4 μm is actually a doublet for most carbonates (Figures 9 and 10, Table 8) and we opted to use the deeper band of the doublet on the long wavelength side for these analyses to conform with past studies.

The dolomite-type carbonates typically form a cluster in between the values of calcite, siderite, and magnesite, consistent with the presence of Ca, Fe, and Mg cations in these carbonates. For the orthorhombic carbonates bands are observed at 2.32, 2.52, 3.51, and 3.96 μm for most aragonites, at 2.35, 2.56, 3.47, and 4.02 μm for strontianite, at 2.38, 2.59, 3.52, and 4.05 μm for witherite. For the alkali carbonates these bands are observed at 2.35, 2.55, 3.50, and 4.01 μm for natrite and at 2.40, 2.60, 3.58, and 4.08 μm for potassium carbonate. The bands near 2.3 and 2.5 μm are consistent with previous measurements of aragonite, strontianite, and witherite (Gaffey, 1987; Hunt & Salisbury, 1971). These bands appear at longer wavelengths than expected for cerussite based on the effective ionic radius of Pb^{2+} and occur at 2.43, 2.65, 3.65, and 4.15 μm, likely due to the electronic structure of the Pb^{2+} cation. Despite the monoclinic structure for alkali carbonates, their band positions follow the expected trend for the effective ionic radii of 9-fold coordinated cations in the orthorhombic structure aragonite group. Our band positions for natrite are roughly consistent with those found by De Angelis et al. (2019) for natrite at 2.34, 2.54, 3.49, and 3.99 μm. Their sample was hydrated at the time of measurement (including water bands near 2 and 3 μm), which could have disrupted the structure slightly. Hopkinson et al. (2018) observed a band at 2.35 μm for natrite, consistent with our spectra, and at 2.36 μm for potassium carbonate, at a shorter wavelength than we observed.

The NIR spectrum of $NaNO_3$ with trigonal structure (Figure 9c) includes bands at 2.43, 2.63, 2.87, 3.17, a doublet at 3.51 and 3.62, a broader band near 4.08, and an asymmetric band with a deep absorption at 4.76 μm. The NIR spectrum of $LiNO_3$ contains similar bands, but they are weakly expressed due to the presence of some H_2O in this sample that is disrupting the structure. Four nitrates with orthorhombic structure were measured and the NIR spectra (Figure 9d) exhibit multiple features, similar in shape to the orthorhombic carbonates, but offset toward longer wavelengths. A prominent trend is observed consistent with the effective ionic radii for $Sr(NO_3)_2$, $Ba(NO_3)_2$, and KNO_3, where the band centers shift toward longer wavelengths with increasing cation size. The band centers for KNO_3 occur at 2.47, 2.61, 2.91, 3.22, 3.66, 4.17, and 4.85 μm. The spectrum of $Pb(NO_3)_2$ contains bands closer to those observed in spectra of KNO_3 (i.e., shifted toward longer wavelengths than expected based on the effective ionic radius). This is similar to the band positions observed for cerussite (lead carbonate). Thus, it appears that the NIR spectra of many carbonates and nitrates follow similar trends with the size of the effective ionic radii of their cations, but the minerals containing Mn^{2+} and Pb^{2+} cations have bands at longer wavelengths than expected.

Comparison of the band centers near 2.3 and 2.5 μm produces clusters of carbonate minerals separated by chemistry. Slightly different trend lines are observed for trigonal, orthorhombic and

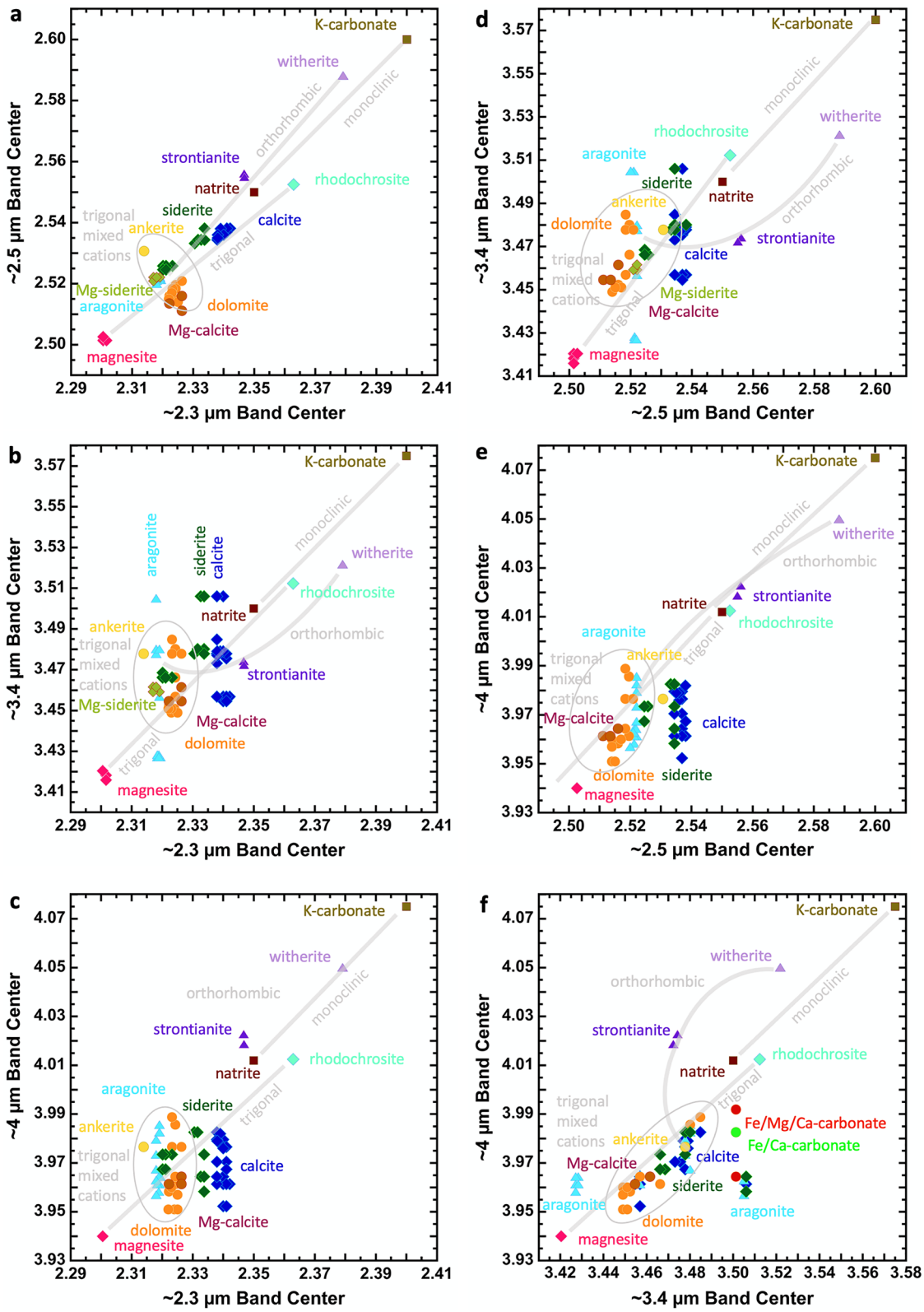

Figure 11. Near-infrared band center comparisons for carbonates. Clusters are identified for spectrally distinct groups. (a) ~2.3 versus ~2.5 µm, (b) ~2.3 versus ~3.4 µm, (c) ~2.3 versus ~4 µm, (d) ~2.5 versus ~3.4 µm, (e) ~2.5 versus ~4 µm, and (f) ~3.4 versus ~4 µm. Diamond symbols mark trigonal structure carbonates, circles mark mixed-cation trigonal structures, triangles mark orthorhombic structures, and squares mark monoclinic structures.

monoclinic carbonates (Figure 11a). A comparison of the bands near 2.3 and 3.4 μm shows related trends with chemistry and structure, but there is wider variance along the 3.4 μm axis and the aragonite-type carbonates do not exhibit a linear trend (Figure 11b). The CRISM spectral range for Mars includes the 3.4 μm band as well, although it is not as readily observed due to some thermal emission contributions in the spectra. Comparing the bands near 2.3 and 4 μm also has wider variance along the 4 μm axis (Figure 11c), and there is more separation between the calcite-type, aragonite-type, and alkali carbonates. Comparing the ~2.5 μm band center with the ~3.4 μm band center produces regular trends for the calcite-type carbonates, but not for the aragonite-type carbonates (Figure 11d). Comparing the band centers near 2.5 and 4 μm produces clusters of carbonates following patterns with the cations and mineral structures, but the variance is wide along the 4 μm axis (Figure 11e). A comparison of the ~3.4 and ~4 μm bands produces tight clusters of carbonates by chemistry (Figure 11f), similar to the ~2.3 versus ~2.5 μm comparison; however, the aragonite-type carbonates form a curving trend rather than a linear trend. Overall, comparisons of the ~2.3 versus ~2.5 μm band centers, the ~2.3 versus ~4 μm band centers, and the ~3.4 versus ~4 μm band centers would be most useful for identifying carbonate cations and structure remotely.

Band shape also varies with carbonate type (Brown et al., 2021). Carbonate bands in the continuum-removed spectra were fit using an asymmetric Gaussian model (Figure S2) in terms of frequency (rather than wavelength), as described in a previous study (Brown, 2006). Centroid, width, and asymmetry (Table S3) were then determined for the bands near 2.5 and 4 μm as outlined in Brown et al. (2010) for several carbonates in this study. These data include multiple grain sizes for some samples including calcite that exhibit a wider range of values at 4 μm. Comparisons of the centroid with the parameters width and asymmetry are shown in Figure 12. Both parameters produce distributions of the data useful for constraining the chemistry of carbonates in spectral data; however the centroid and parameters of the ~2.5 μm band cluster more tightly, which would better enable extraction of carbonate composition from these data. Comparisons of the centroid to the width and asymmetry parameters reveal separate clusters of data for many types of carbonates in our study (Figure 12). Clear patterns are observed in some cases that distinguish types of carbonate minerals and specific carbonate compositions by combining width or asymmetry parameters together with the band center. The accuracy would be improved by using data from both the bands near 2.5 and 4 μm.

The Fe^{2+} and Mn^{2+} electronic excitation bands in carbonate spectra arise from crystal field splitting, where a 3d electron transitions from the ground state to an excited state, and from electronic transfer between atoms (Burns, 1993). In the case of crystal field theory transitions for siderite an Fe^{2+} electron jumps from the $^5T_{2g}$ ground state to the ^5E_g excited state (e.g., Gaffey, 1987; Hunt & Salisbury, 1971; Lobanov et al., 2015) producing a deep, broad absorption band near 1.0–1.3 μm (Figure 13; Gaffey, 1987; Hunt & Salisbury, 1971). This band is nearly saturated in spectra of siderites with >40 wt.% FeO, but is observed as a weaker band in spectra of carbonates containing less Fe. This is observed for dolomite JB1461 (6.4 wt.% FeO) and dolomite JB779 (unknown FeO) with moderate crystal field theory bands, as well as for magnesite sample JB1161 (0.35 wt.% FeO) and magnesite sample JB946 (0.40 wt.% FeO) with weak crystal field theory bands (Figure 13). This Fe crystal field theory band can also be split due to the presence of Mg or other cations that disrupt the structure. Spectra of some of the Fe-bearing carbonates in Figure 13 exhibit two crystal field theory absorption minima near 1.04–1.08 μm and near 1.25–1.29 μm. Additional O^{2-} to Fe^{2+} charge transfer bands are observed below 0.8 μm.

For rhodochrosite spectra, crystal field splitting arises for an electronic transition in Mn^{2+} from the $^6A_{1g}$ ground state to multiple excited states giving rise to sharp absorptions in the range 0.3–0.55 μm (Gaffey, 1987; Hunt & Salisbury, 1971; Le Paillier-Malécot, 1973; Stevenson, 1968). These are observed at 0.311, 0.345, 0.409, 0.443, and 0.548 μm in spectra of two rhodochrosite spectra from the Hunt and Salisbury (1971) collection. Other siderite samples containing 1.3 and 2.7 wt.% MnO exhibit features in this region at different wavelengths attributed to crystal field theory bands of the disrupted structure of $MnCO_3$ in a siderite framework.

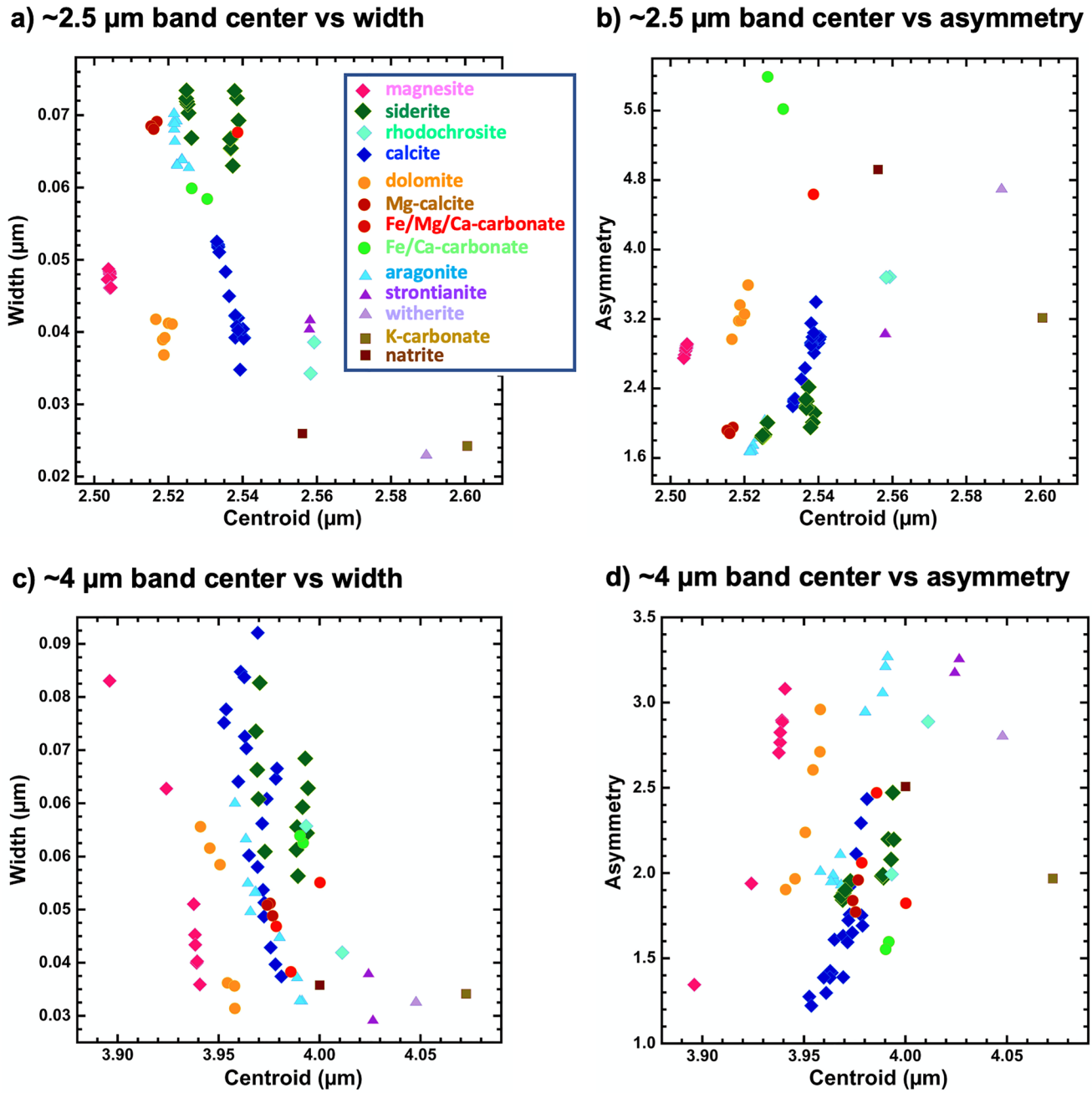

Figure 12. Band parameter comparisons for carbonates. (a) Band center versus width at ~2.5 µm. (b) Band center versus asymmetry at ~2.5 µm. (c) Band center versus width at ~4 µm. (d) Band center versus asymmetry at ~4 µm. Diamond symbols mark trigonal structure carbonates, circles mark mixed-cation trigonal structures, triangles mark orthorhombic structures, and squares mark monoclinic structures.

6. Band Assignments for Overtones and Combination Bands

6.1. Changes in Spectral Features With Particle Size and Chemistry

Investigating the spectral properties of carbonates containing both Fe and Mg cations is important because Fe/Mg-carbonate has been found in martian meteorites (e.g., Bishop, Mustard, et al., 1998; McKay et al., 1996) and is present on Mars in multiple locations (e.g., Bishop, Tirsch, et al., 2013; Brown et al., 2020; Ehlmann et al., 2008; Wray et al., 2016). In order to demonstrate changes in band position and spectral shape with particle size and chemistry, three trigonal carbonates were selected with variable Fe and Mg cations.

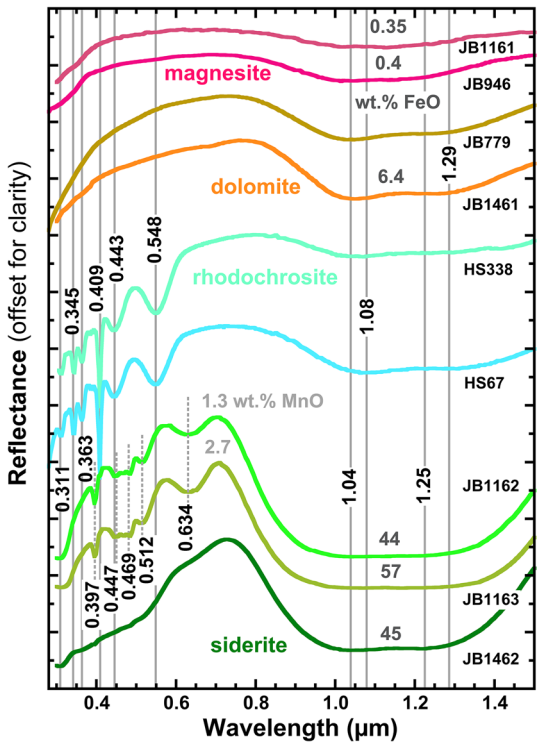

Figure 13. Extended visible region reflectance spectra of Fe^{2+}-, Mg^{2+}-, and Mn^{2+}-bearing carbonates including electronic absorptions due to Fe^{2+} and Mn^{2+}. The spectra of carbonates with the highest Fe abundance are shown at the bottom and the lowest Fe abundance at the top.

VNIR spectra are brighter for the finer grain sizes and bands are typically broader for the spectra of the coarser grain size fractions (Figure 14a). The Fe-rich samples also contain minor Mn, discussed above. The shape of the strong bands near 3.4 and 4 μm changes with grain size, such that broader and flatter features are observed for the coarser size fraction and narrower features with more structure are observed in the finer size fractions. Spectra of the Mg-rich carbonate have stronger bands than the samples containing more Fe. The band centers shift slightly toward longer wavelengths as the Fe concentration increases, similar to trends in the mid-IR region. For example, the bands at 2.300 and 2.501 μm in the magnesite spectrum shift to 2.319 and 2.522 μm for the Fe/Mg-carbonate spectrum and to 2.334 and 2.538 μm in the siderite spectrum.

Mid-IR spectra exhibit stronger Reststrahlen features for the coarser grained samples and more contrast near 1,700–2,000 cm^{-1} for the finer grained samples (Figure 14b). The ν_3 vibration near 1,500 cm^{-1} occurs as an upward peak for all spectra, contrasted by the ν_4 vibration near 750 cm^{-1} that occurs as a downward band for all grain sizes. Finally, the ν_2 vibration near 900 cm^{-1} occurs as a reflectance maximum for larger particle sizes and as a reflectance minimum for smaller particle sizes.

6.2. Comparing Calculated Overtones and Combination Bands With Measured Bands

Early spectral analyses by Schaefer et al. (1926) and Matossi (1928) used polarized light and prisms to measure the spectral properties of single crystals of magnesite, dolomite, calcite, siderite, witherite, and cerussite from 2 to 20 μm. Their analyses noted differences in the NIR band positions for different carbonates. Subsequent analyses by Hexter (1958a) using transmittance through calcite single crystals and group theory calculations produced potential band assignments for several NIR bands near 2.37 μm ($3\nu_3$), 2.55 μm ($2\nu_3 + \nu_1$), 2.82 μm ($2\nu_3 + \nu_2$), 3.2 μm ($\nu_3 + \nu_1 + \nu_4$), 3.5 μm ($2\nu_3$), and 4 μm ($\nu_3 + \nu_1$). The ν_3 vibration occurs frequently in Hexter's NIR assignments. This is expected because the ν_3 band is the dominant vibration in the mid-IR region. Later reflectance spectra of multiple carbonates by Hunt and Salisbury (1971) observed these NIR bands at slightly different wavelength values, likely due to the differences in scattering between transmittance and reflectance spectroscopy. Hunt and Salisbury (1971) modified the band assignments suggested by Matossi (1928) for a few strong NIR carbonate bands and added assignments for the bands at shorter wavelengths near 1.8–1.9 μm ($3\nu_3 + \nu_1$), ~2 μm ($2\nu_3 + 2\nu_1$), and ~2.1–2.2 μm ($2\nu_3 + \nu_1 + \nu_4$). Gaffey (1986, 1987) analyzed NIR reflectance spectra of several carbonates from 0.35 to 2.55 μm, characterized the shape of the CO_3^{2-} overtone and combination bands, provided the crystal field theory bands for the electronic transitions for Fe- and Mn-bearing carbonates, and summarized the band assignments known at that time. Gunasekaran et al. (2006) measured Raman and IR spectra of calcite group carbonates and agreed with the band assignments proposed earlier (Hunt & Salisbury, 1971). The NIR spectral features of carbonates have also been described in summaries of the spectral properties of minerals (Bishop, 2019; Clark et al., 1990; Gaffey et al., 1993).

One complication for assigning the combinations of the fundamental vibrations for these NIR bands is that they rely heavily on the ν_3 vibration and that is measured at different vibrational energies, depending on the technique (see Table 7). Another complication is that the band shapes vary with particle size (Figures 1, 14 and 15). We calculated a large number of possible band assignments for 27 anhydrous carbonates and 7 anhydrous nitrates with different chemistries for bands occurring from ~1.8 to 5.5 μm by summing up the vibrational frequencies in wavenumbers to test the previously suggested band assignments and fill in gaps for additional features. The full band assignment comparison is given in Table S4 using measured fundamental vibrations for each sample. Overtones and combinations were also computed using transmittance spectra from Weir and Lippincott (1961) for comparison. Band assignments for magnesite, calcite,

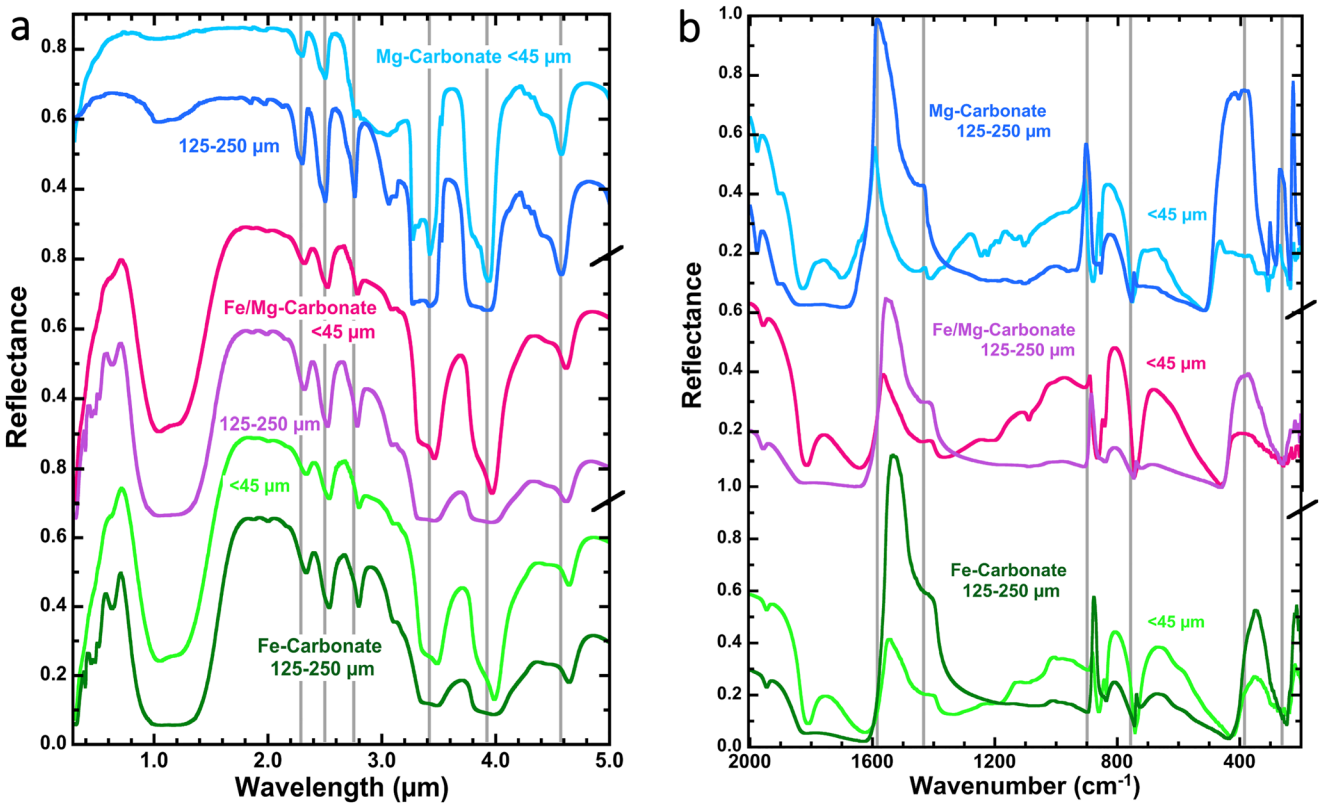

Figure 14. Visible/near-infrared and mid-IR reflectance spectra of two particle size fractions of carbonates with variable Mg and Fe abundances. (a) VNIR spectra from 0.35 to 5 µm. (b) Mid-IR spectra from 200 to 2,000 cm^{-1} (5–50 µm). The magnesite JB1161 contains 0.005 Fe and 0.995 Mg site occupancies, while the Fe/Mg-carbonate JB1162 contains 0.65 Fe, 0.33 Mg, and 0.02 Mn site occupancies, and the siderite JB1163 contains 0.91 Fe, 0.06 Mg, and 0.03 Mn site occupancies. Spectra are offset for clarity, and gray lines mark features in the Mg-carbonate spectra.

and aragonite are presented in Table 9 and spectra of multiple particle sizes of calcite and aragonite are shown in Figure 15 from 150 to 4,600 cm^{-1} (~2.2–66 µm) with potential band assignments marked near the spectral features. We calculated combination bands separately in many cases for the ν_3' vibration (reflectance maximum) and the ν_3 vibration (shoulder or secondary peak in reflectance) that is often more similar to the ν_3 absorption observed in transmittance spectra. Based on the positions of the NIR overtones and combinations observed in reflectance spectra it is necessary to use band assignments including both the ν_3' and ν_3 modes to fully explain these features. This also enabled more accurate band assignments that more fully describe the features observed in the NIR region. Similar plots illustrate these features for magnesite, Mg/Fe-carbonate, siderite, and dolomite in Figure S3. Many of the original band assignments from Hexter (1958a) and Hunt and Salisbury (1971) still hold (Table 9). However, these only describe a fraction of the NIR overtones and combination bands that are present in carbonate spectra. The Hunt and Salisbury (1971) study only had access to the spectra up to 2.5 µm and thus was not able to characterize the band near 2.5 µm or any of the bands at longer wavelengths. By viewing these spectra across the full range from ~2.2 to 66 µm (150–4,600 cm^{-1}) with varying particle size, the associations among the NIR and mid-IR features are more clear and new band assignments were made here for features in the range 2.5–6 µm as well as for shoulders and smaller features below 2.5 µm that were not considered by Hunt and Salisbury (1971).

The spectral properties of nitrates are expected to follow similar trends to those of carbonates because the spectral properties of nitrates are similar to those of carbonates. Although much of the work on band assignments was performed using spectra of carbonates, a few band assignments were also investigated using spectra of nitrates (Hexter, 1958b; Weir & Lippincott, 1961). More recently, the NIR spectral properties of nitrates from the Atacama were investigated by Sutter et al. (2007) and Wang et al. (2018) from 0.35 to 2.5 µm. Wang et al. (2018) also presented NIR reflectance spectra of several anhydrous and hydrated nitrates with different cations. Cloutis et al. (2016) measured reflectance spectra of nitrates and other compounds from

0.35 to 20 μm. The nitrate spectra in these studies support our assumption that parallel band assignments for the nitrates are expected. As described above for carbonates, potential combination bands were computed for nitrates from the measured fundamental vibrations for each sample (Table S4). Overtones and combinations were also computed using transmittance spectra from Weir and Lippincott (1961) when available.

These potential calculated overtones and combination bands were compared to the observed NIR bands for three example nitrates: $LiNO_3$, $NaNO_3$, and KNO_3. However, overtone calculations for nitrates are more complex than those of carbonates due to the increased anharmonicity in the NO_3^- anion compared with the CO_3^{2-} anion. In general, the vibrational frequencies of overtones are less than the energy of the fundamental vibration and an anharmonicity constant X is defined as $\nu_0 = \nu_1/(1 - 2X)$ (e.g., Herzberg, 1945). This anharmonicity constant is higher for molecules with increased H-bonding (Sándorfy, 2006), is increased for molecules with very different masses (Siesler, 2017), and is low for heavier atoms (Bron & Hacker, 1973) in stable molecules (Bron, 1975). Calculations of the anharmonicity constant by Groh (1988) found a 3-fold increase for OH and CH vibrations compared with C=O vibrations and Gupta (2016) found negligible anharmonicity constants for CO vibrations. For these reasons, we opted not to use anharmonicity constants for our carbonate calculations. However, anharmonicity constants are as high as -86 cm^{-1} for OH stretching vibrations in phyllosilicates (Petit et al., 2004) and in the range -30 to -50 cm^{-1} for NO_2^- vibrations near 1,300 cm^{-1} (Cheng & Steele, 2014). We tested several options for the NO_3^- band assignments related to those of carbonates and found that estimated anharmonicity constants of -60 cm^{-1} worked well for the ν_3 band (Table 10). Typically lower anharmonicity constants are needed for bands with lower frequencies, so we applied values of -40 cm^{-1} for the ν_1 band, and -20 cm^{-1} for the ν_2 and ν_4 bands. These are estimates, but serve as examples to illustrate relationships between the fundamental nitrate vibrations and the calculated overtone and combination band absorptions observed in NIR spectra.

7. Implications for Spectroscopic Detection and Characterization of Carbonates and Nitrates

The laboratory data presented here are intended as a resource for remote detection of carbonates and nitrates on the Earth and planetary bodies, as well as for investigation of these minerals in laboratory samples.

Carbonates have been identified in several locations across Mars with varying band shapes near 2.3 and 2.5 μm, indicating variations in the type of carbonates at different locations (Wray et al., 2016). One of the sites on Mars with the most abundant carbonate rocks occurs in the NE Syrtis—Nili Fossae region including Jezero crater, currently being explored by the Mars 2020 Perseverance rover. Specifically, carbonates are under investigation by Perseverance at Jezero crater using Raman spectroscopy collected by the Scanning Habitable Environments with Raman and Luminescence for Organics & Chemicals (SHERLOC) instrument (Beegle et al., 2015) and elemental data from the SuperCam instrument (Wiens et al., 2016). SuperCam will also collect NIR and Raman point spectra of selected outcrops that could be analyzed with the NIR and Raman data presented here. The Raman spectra of carbonates presented in this study will help characterize the type of carbonates present and identify variations in carbonate chemistry across the terrain visited by Perseverance. Coordinating the in situ Raman detections with orbital VNIR data from CRISM will help to further constrain the carbonate type. Recent advances in image calibration are enabling scientists to better resolve the spectral features of small surface outcrops (Itoh & Parente, 2021), and new algorithm development is supporting identification and mapping of these small outcrops (Saranathan & Parente, 2021). Applying new techniques to orbital CRISM images of Jezero crater is enabling refined characterization of carbonates and other minerals there (Parente et al., 2019).

CRISM detections of carbonates at Jezero crater and elsewhere on Mars rely heavily on the band positions near 2.3 and 2.5 μm (e.g., Brown et al., 2020; Ehlmann et al., 2008), but these band positions can be influenced by admixtures of Fe-rich phyllosilicates (Bishop, Perry, et al., 2013). Additionally, the carbonate band near 3.4 μm is not observed as consistently as the other diagnostic bands. However, with improvements in image calibration (Itoh & Parente, 2021; Seelos et al., 2016), oversampling to view smaller surface regions (Kreisch et al., 2017), and reduction in noise and thermal emission contributions (He et al., 2019), this feature is becoming better resolved in CRISM spectra. Palomba et al. (2009) also found evidence for

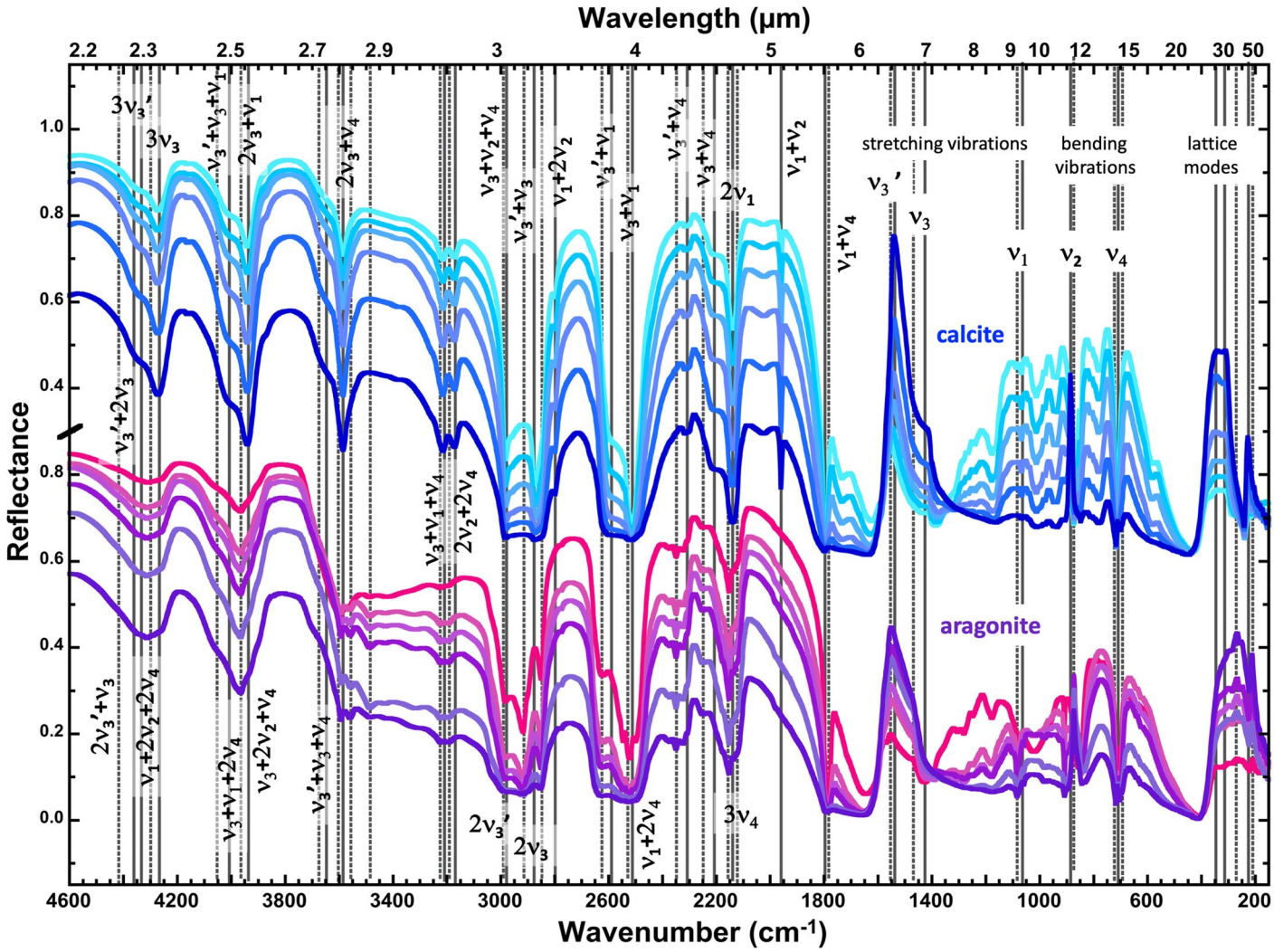

Figure 15. Reflectance spectra across the near-infrared and mid-IR regions illustrating combination and overtone bands. Spectra are included for multiple grain sizes (<45, 45–75, 75–90, 90–125, 125–250, and >250 μm) of calcite JB1458 and aragonite JB1459 with the lighter colors corresponding to the finer size fractions. Possible overtone and combination bands are listed in relation to the fundamental stretching and bending vibrations.

Mg-carbonate on Mars using the band near 3.9–4.0 μm in orbital spectra acquired by the Planetary Fourier Spectrometer (PFS) onboard Mars Express, although this band is weak due to the wide surface footprint.

The band center comparisons reported here for the 2.3, 2.5, and 3.4 μm features are expected to support better estimates of the carbonate chemistry on Mars and its variation in surface outcrops. A summary of carbonate detections using CRISM spectra by Wray et al. (2016) noted that variations in the spectral bands are observed for carbonate outcrops at Nili Fossae, Libya Montes, Leighton crater, McLaughlin crater, and Huygens crater, and a closer look at these data may be warranted using the results from this study. NIR spectra of Fe- and Mg-bearing carbonates are also displayed in Figure 16a by varying cation abundances. Shifts are observed from 2.30 to 2.33 μm with increasing Fe abundance, as well as 2.50–2.53, 2.76–2.79, 3.27–3.36, 3.42–3.49, 3.79–3.84, and 3.94–4.0 μm for features observable by CRISM and other airborne spectrometers.

Carbonates are widespread on Ceres (De Sanctis et al., 2016) as detected by the visible and infrared mapping spectrometer (VIR) on the Dawn mission (De Sanctis et al., 2019). The position of the ~4 μm band in VIR spectra of Ceres varies from 3.95 to 4.01 μm, indicating a range of carbonate compositions (Carrozzo et al., 2018). The most abundant form of carbonates on Ceres includes Mg and Ca cations, but natrite and hydrous Na carbonates are also thought to be present in smaller outcrops (Carrozzo et al., 2018). The strong

Table 9
Band Assignments for Magnesite, Calcite, and Aragonite

Magnesite JB0946				Calcite JB1458				Aragonite JB1459					
Meas. μm	Meas. cm^{-1}	Calc. R	Calc. T	Meas. μm	Meas. cm^{-1}	Calc. R	Calc. T	Meas. μm	Meas. cm^{-1}	Calc. R	Calc. T	Band Assignment	Source
1.85	5405	5407	5521	1.88	5319	5327	5383	1.90	5263	5508	5377	$3\nu_3+\nu_1$	Hunt and Salisbury (1971)
1.97	5076	5078	5130	2.00	5000	4974	5038	1.99	5025	5116	5034	$2\nu_3+2\nu_1$	Hunt and Salisbury (1971)
		4728	4792			4623	4663			4750	4662	$2\nu_3+\nu_1+\nu_4$	Hunt and Salisbury (1971) assignment for 2.16 μm
2.13	4695	4680	4740	2.16	4630	4616	4626	2.16	4630	4698	4592	$2\nu_3+2\nu_2$	
		4825	4759			4633	4685			4683	4691	$3\nu_1+2\nu_4$	
		4767				4629				4650	4650	$3\nu_3'$	
		4612				4506				4575	4530	$2\nu_3'+\nu_3$	
		4457				4383				4500	4410	$\nu_3'+2\nu_3$	
		4427	4369			4275	4273			4265	4249	$\nu_1+2\nu_2+2\nu_4$	
2.3005	4347	4302	4434	2.3410	4272	4260	4296	2.318	4314	4425	4290	$3\nu_3$	Hexter (1958a)
		4128				4030				4108	4067	$\nu_3'+\nu_3+\nu_1$	
		4049	4063			3919	3943			3992	3947	$\nu_3+\nu_1+2\nu_4$	
2.5026	3996	4001	4011	2.5369	3942	3912	3906	2.5221	3965	3940	3877	$\nu_3+2\nu_2+\nu_4$	
		3973	4043			3907	3951			4033	3947	$2\nu_3+\nu_1$	Hexter (1958a) assignment for 2.5 μm
		3778				3679				3742	3683	$\nu_3'+\nu_3+\nu_4$	
2.76	3623	3623	3705	2.79	3584	3556	3576	2.78	3597	3667	3575	$2\nu_3+\nu_4$	
		3294	3314			3203	3231	2.87	3484	3275	3232	$\nu_3+\nu_1+\nu_4$	
3.06	3268	3322	3282	3.10	3226	3208	3186	3.00	3333	3182	3162	$2\nu_2+2\nu_4$	
3.12	3205	3095	3119	3.15	3175	3024	3025	3.13	3195	3066	3011	$\nu_3+\nu_2+\nu_4$	
		3178				3086				3100	3100	$2\nu_3'$	
3.2740	3054	3023		3.3155	3016	2963		3.3519	2983	3025	2980	$\nu_3'+\nu_3$	
3.4204	2924	2917	2871	3.4546	2895	2843	2849	3.43	2915	2831	2819	$\nu_1+2\nu_2$	
		2868	2956	3.5100	2849	2840	2864	3.51	2849	2950	2860	$2\nu_3$	Hexter (1958a)
3.79	2639	2694		3.8100	2625	2610		3.81	2625	2633	2637	$\nu_3'+\nu_1$	
3.9400	2538	2539	2565	3.9614	2524	2487	2519	3.9796	2513	2558	2517	$\nu_3+\nu_1$	Hexter (1958a)
		2615	2585			2499	2511			2517	2517	$\nu_1+2\nu_4$	
4.26	2347	2344		4.33	2309	2259		4.25	2353	2267	2265	$\nu_3'+\nu_4$	
4.42	2262	2189	2227	4.53	2208	2136	2144	4.44	2252	2192	2145	$\nu_3+\nu_4$	
4.58	2183	2265	2247	4.67	2141	2148	2136	4.65	2151	2151	2145	$3\nu_4$	
		2210	2174			2134	2174			2166	2174	$2\nu_1$	
Meas.	1976	2011	1979	Meas.	1961	1955	1968	Meas.		1957	1953	$\nu_1+\nu_2$	
	1830	1860	1836		1798	1783	1799		1788	1800	1802	$\nu_1+\nu_4$	
	1589				1543				1550		1550	ν_3'	
	1434		1478		1420		1432		1475		1430	ν_3	
	1105		1087		1067		1087		1083		1087	ν_1	
	906		892		888		881		874		866	ν_2	
	755		749		716		712		717		715	ν_4	
									702		703	ν_4'	

Note. "Meas." indicates measured bands, "Calc." indicates calculated bands, *R* refers to reflectance, and *T* refers to transmittance, four digits provided for bands determined from CR data, two digits provided for bands determined from regular spectra; red data are the fundamental vibrations; blue data are wavelength values (in μm) converted from wavenumbers (in cm^{-1}).

band centered at 4.01 μm and weaker doublet at 3.4 and 3.5 μm in spectra collected at Ocator crater were attributed to natrite (Raponi et al., 2019), which is consistent with our results. The shape of the ~4 μm carbonate bands with doublet features near 3.81 and 3.96 μm (De Sanctis et al., 2018) most closely resembles the character of dolomite in our study. This feature varies with the abundance of Ca, Mg, and Fe in our

Table 10
Band Assignments for Selected Nitrates (Li, Na, and K)

LiNO3 JB1583A <125 μm				NaNO3 JB1584A <125 μm				KNO3 JB998A <125 μm					
Meas.	Meas.	Calc.	Calc.	Meas.	Meas.	Calc.	Calc.	Meas.	Meas.	Calc.	Calc.	Band	Source
μm	cm^{-1}	R	T	μm	cm^{-1}	R	T	μm	cm^{-1}	R	T	Assignment	
2.06	4850	4922	4876	2.07	4831	4962	4826	2.10	4764	4846	4840	$2\nu_3$ -60 $+2\nu_1$ -40	
2.22	4515	4583	4580	2.22	4505	4634	4558	2.25	4444	4477	4478	$3\nu_1$ –2*40 $+2\nu_4$ -20	
2.402	4163	4206	4140	2.428	4119	4191	4065	2.467	4054	4152	4140	$3\nu_3$ -2*60	
2.621	3815	3836	3824	2.627	3807	3797	3778	2.673	3741	3767	3768	$\nu_3+2\nu_2$ -20$+\nu_4$	
2.87	3484	3562	3518	2.87	3484	3540	3457	2.91	3436	3503	3494	$2\nu_3$ -60 $+\nu_4$	
3.17	3155	3249	3226	3.17	3155	3257	3190	3.22	3106	3188	3184	$\nu_3+\nu_1+\nu_4$	
3.29	3040	3112	3122	3.30	3030	3066	3090	3.32	3012	3038	3042	$2\nu_2$ –20 $+2\nu_4$ -20	
3.29	3040	3018	3001	3.30	3030	2990	2960	3.32	3012	2963	2961	$\nu_3+\nu_2+\nu_4$	
3.472	2880	2898		3.508	2851	2852		3.599	2779	2828		$2\nu_3'$ -60	
3.472	2880	2745	2754	3.508	2851	2748	2744	3.599	2779	2697	2704	$\nu_1+2\nu_2$	
3.606	2773	2824	2780	3.616	2765	2814	2730	3.657	2734	2788	2780	$2\nu_3$ -60	after Hexter (1958a)
4.014	2491	2548		4.039	2476	2550		4.039	2476	2493		$\nu_3'+\nu_1$	
4.089	2446	2511	2488	4.119	2428	2531	2463	4.175	2395	2473	2470	$\nu_3+\nu_1$	Hexter (1958a)
4.64	2155	2180	2158	4.69	2132	2163	2122	4.66	2146	2139	2134	$\nu_3+\nu_4$	
4.74	2110	2098	2096	4.76	2101	2148	2096	4.85	2062	2058	2060	$2\nu_1$ -40	
Meas.	1904	1907	1911	Meas.	1900	1921	1906	Meas.	1875	1873	1877	$\nu_1+\nu_2$	
	1797	1807	1806		1792	1820	1795		1763	1764	1764	$\nu_1+\nu_4$	
	1479				1456				1444			ν_3'	
	1442		1420		1437		1395		1424		1420	ν_3	
	1069		1068		1094		1068		1049		1050	ν_1	
	838		843		827		838		824		827	ν_2	
	738		738		726		727		715		714	ν_4	
									696			ν_4'	

Note. "Meas." indicates measured bands, "Calc." indicates calculated bands, *R* refers to reflectance, and *T* refers to transmittance, four digits provided for bands determined from CR data, two digits provided for bands determined from regular spectra; estimated anharmonicity constants of −60 cm^{-1} for ν_3, −40 cm^{-1} for ν_1, −20 cm^{-1} for ν_2, and −20 cm^{-1} for ν_4 were applied; red data are the fundamental vibrations; blue data are wavelength values (in μm) converted from wavenumbers (in cm^{-1}).

samples; thus, the shape of this feature could be used for refined determination of carbonate chemistry. The NIR spectra shown in Figure 16b illustrate trends from magnesite to dolomite to calcite with several examples of carbonates with intermediate cation chemistries. The primary NIR bands for dolomite occur near 2.32, 2.52, 2.77, 3.31, 3.46, 3.81, and 3.96 μm.

Carbonates were also observed using OSIRIS-REx Visible and InfraRed Spectrometer (OVIRS) data of near-Earth asteroid (101955) Bennu (Kaplan et al., 2020; Simon et al., 2020). A complex feature is observed near 3.4 μm in OVIRS spectra including multiple overlapping bands that vary with location across Bennu; this feature is attributed to a combination of organic material and carbonates (Simon et al., 2020). Thermal contributions increase toward 4 μm in these spectra increasing the challenge for characterizing the shape of the 4 μm band. The ~3.4 μm band is particularly strong for spectra of the Nightingale crater region, where at least three different spectral shapes are observed, consistent with different carbonate chemistries (Kaplan et al., 2020). The pixel size for the OVIRS data is ~20 m × 30 m, indicating that the outcrops containing carbonates and organics are sufficiently large to contribute spectrally to these pixels. Additional NIR and TIR spectral features observed at Bennu indicate the presence of phyllosilicates and magnetite, providing a mineral assemblage together with the carbonates that is consistent with carbonaceous chondrite meteorites (Hamilton et al., 2019).

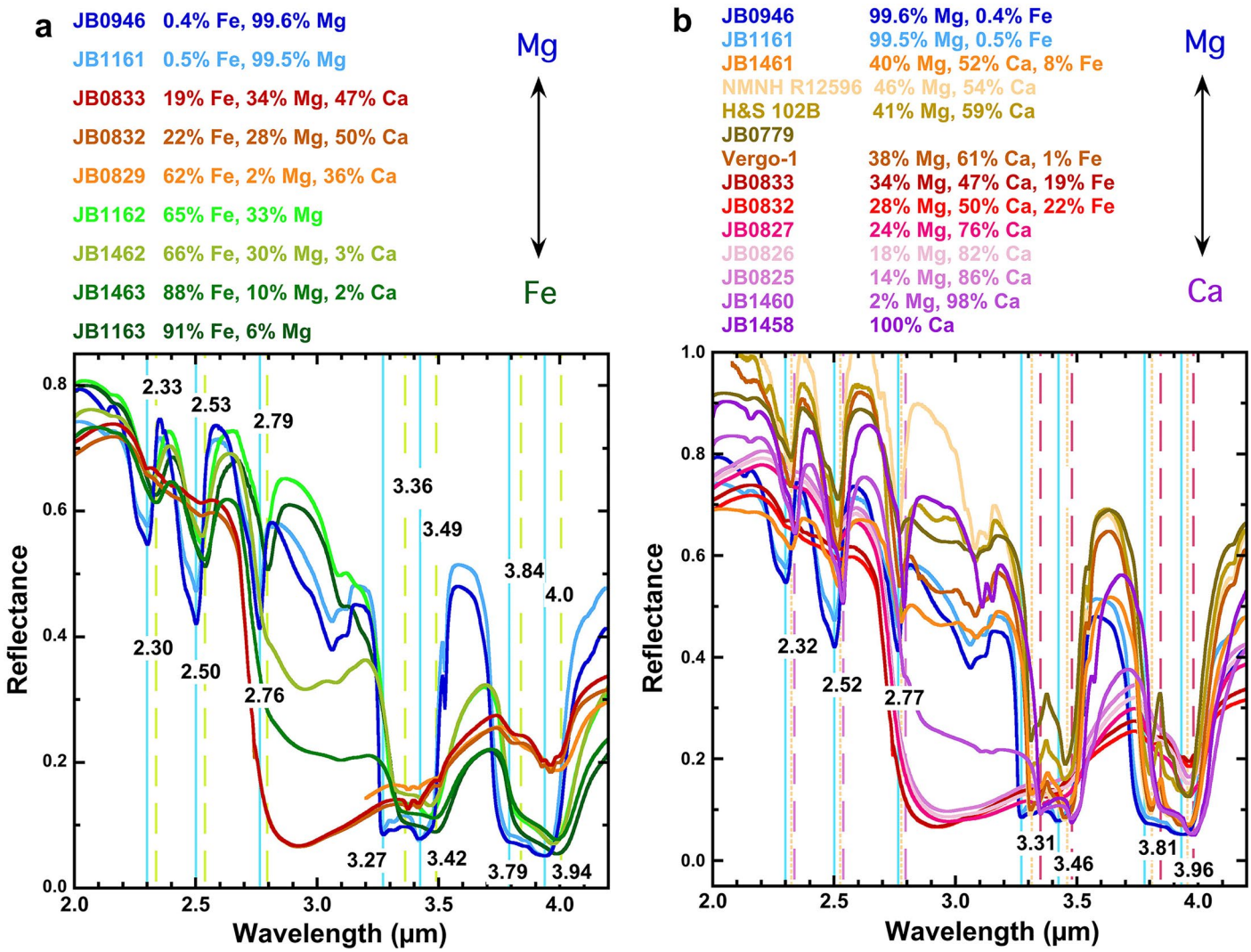

Figure 16. Near-infrared reflectance spectra from 2 to 4.2 μm illustrating variations in carbonate features with chemistry. (a) Trends in carbonate band position and shape from Mg-rich to Fe-rich samples. Light blue lines mark the band centers for magnesite and light green dashed lines mark band centers for siderite. Band center values for magnesite are provided below the spectra and the values for siderite are provided above the spectra. (b) Trends in carbonate band position and shape from Mg-rich to Ca-rich samples. Band centers for dolomite are provided with orange dotted lines marking the position of the bands. Calcite band positions are marked by pink dashed lines.

Nitrates are abundant in the Atacama region of Chile and VNIR spectra have been used for characterization of nitrates there (Sutter et al., 2007; Wang et al., 2018). The band at 2.42 μm observed in Atacama rocks (Wang et al., 2018) is most consistent with $NaNO_3$ (Figure 9c). Using the changes in band positions observed for nitrates in this study, the chemistry of nitrates could be determined for nitrates observed in the Atacama, in lab samples, or on planetary surfaces if they are present.

8. Conclusions

The purpose of this study was to gain an understanding of the band assignments for VNIR spectral features in anhydrous carbonates and nitrates through comparison with the mid-IR and Raman spectra and mineral chemistry, as well as to provide a comprehensive database of carbonate and nitrate spectral features for remote identification of these minerals on planetary surfaces. The mid-IR spectra of anhydrous carbonates and nitrates are dominated by the ν_3 asymmetric stretching vibration of the CO_3^{2-} and NO_3^- anions near 1,275–1,590 cm^{-1} (~6–8 μm) and lattice modes at 150–600 cm^{-1} (~20–60 μm). Similarly, Raman spectra are

dominated by the ν_1 symmetric stretching vibration near 1,050–1,080 cm^{-1} (~9–10 μm), but also include noticeable bands due to lattice modes. Weak bands in IR and Raman spectra are also observed for the ν_2 out-of-plane bending vibration and the ν_4 in-plane bending vibration.

NIR reflectance features include overtones of the ν_3 band and combinations of all four fundamental vibrations, even if they are not well expressed in mid-IR spectra. Previously proposed band assignments for NIR features were tested and new band assignments were recommended through comparison of related minerals with differing cation chemistries. Carbonates and nitrates include a large number of overlapping bands in the NIR region that form the characteristic shape of the NIR spectra of carbonate and nitrate minerals. The most important features for remote detection of carbonates are observed at ~2.3, 2.5, 3.4, 4.0, and 4.6 μm. These bands are shifted to slightly longer wavelengths for nitrates and occur at ~2.4, 2.6, 3.5, 4.1 and 4.8 μm.

Extended visible region bands are observed in Fe- and Mn-bearing carbonates due to electronic transitions. Siderites and other Fe-bearing carbonates exhibit a strong, broad crystal field theory band from ~1 to 1.3 μm that can be split into a doublet shape when other cations are present. The influence of Fe is nonlinear, with small amounts of Fe inducing a noticeable band in carbonate spectra. Multiple, sharp features are observed in rhodochrosite spectra from 0.3 to 0.55 μm. Related bands shifted toward longer wavelengths (~0.4–0.63 μm) are observed in siderites with minor Mn abundance. This is attributed to a disruption of the mineral structure due to the different size of the Fe^{2+} cation, which is largely controlling the structure.

Multiple spectral features are characterized in this study for several types of carbonates and nitrates. Band centers of key NIR, mid-IR, and Raman features are coordinated to facilitate remote detections of these minerals on planetary surfaces. Band asymmetry and width are also compared with the band center for selected NIR features. Many of these band center comparisons and band feature comparisons produce clusters of data for distinct groups or types of carbonates and nitrates. In general the mid-IR and NIR band positions followed trends with the size of the effective ionic radii of the cation. One exception to this is the Pb^{2+} cation in both carbonate and nitrate. This study provides reflectance spectra from 0.3 to ~50 μm of a large collection of carbonates and nitrates, accompanied by emissivity spectra, Raman spectra, and XRD for many of the samples. This data will support remote detection of carbonates and nitrates on planetary bodies and will enable better determination of carbonate chemistry on planetary bodies including Mars, Ceres, and Bennu.

Conflict of Interest

The authors declare no conflicts of interest relevant to this study.

Data Availability Statement

Raw spectral data are available at Brown University's Reflectance Experiment Lab (RELAB): Milliken, R. (2020). RELAB Spectral Library Bundle. Geosciences Node. https://doi.org/10.17189/1519032 and the USGS Spectroscopy Lab at https://www.usgs.gov/labs/spec-lab. The continuum removed spectral data produced in this study are included as supplementary data files and are shared on the SETI Institute Data Repository at https://dmp.seti.org/jbishop/carbonates_xxi/ as well as at a unique, searchable public site at the Open Science Framework (OSF): https://osf.io/hru4c/. Any use of trade, firm, or product names in this publication is for descriptive purposes only and does not imply endorsement by the U.S. Government. Detailed information about the band centers and band assignment calculations are provided in supporting online tables and figures.

Acknowledgments
The authors wish to thank W.R. Gnesda and C. Haberle for helpful comments that improved this article. Support for this project in the early stages was provided by grant #NNX12AO55G from NASA's Planetary Geology and Geophysics Program to J. L. Bishop and A. J. Brown, and the Planetary Geology and Geophysics Research for Undergraduates Program to S. J. King. Recent support was provided to J. L. Bishop, S. J. King, and A. J. Brown from NASA's Astrobiology Institute and to J. L. Bishop from PDART grant # 80NSSC19K0424. J. F. Lin acknowledges support from the Geophysics Program of the National Science Foundation (EAR-1916941).

References

Adler, H. H., & Kerr, P. F. (1963). Infrared spectra, symmetry and structure relations of some carbonate minerals. *American Mineralogist*, *48*, 839–853. https://doi.org/10.2113/gsecongeo.58.6.839

Aronson, J. R., Emslie, A. G., & McLinden, H. G. (1966). Infrared Spectra from Fine Particulate Surfaces. *Science*, *152*(3720), 345. https://doi.org/10.1126/science.152.3720.345-a

Bandfield, J. L., Glotch, T. D., & Christensen, P. R. (2003). Spectroscopic identification of carbonate minerals in the Martian dust. *Science*, *301*, 1084–1087. https://doi.org/10.1126/science.1088054

Beegle, L., Bhartia, R., White, M., DeFlores, L., Abbey, W., Wu, Y.-H., et al. (2015). *SHERLOC: Scanning habitable environments with Raman and luminescence for organics and chemicals*. Paper presented at the Proceedings of the 2015 IEEE Aerospace Conference (Vol. 1, p. 11).
Bishop, J. L. (2019). Chapter 4: Visible and near-infrared reflectance spectroscopy of geologic materials. In J. L. Bishop, J. F. Bell III, & J. E. Moersch (Eds.), *Remote compositional analysis: Techniques for understanding spectroscopy, mineralogy, and geochemistry of planetary surfaces* (pp. 68–101). Cambridge University Press. https://doi.org/10.1017/9781316888872.006
Bishop, J. L., King, S. J., Lane, M. D., Lafuente, B., Brown, A. J., & Hiroi, T. et al. (2017). Spectral properties of anhydrous carbonates and nitrates. Paper presented at the 48th Lunar and Planetary Science Conference (Abstract #2362).
Bishop, J. L., & Murad, E. (2002). Spectroscopic and geochemical analyses of ferrihydrite from springs in Iceland and applications to Mars. In J. L. Smellie & M. G. Chapman (Eds.), *Volcano-ice interactions on Earth and Mars* (pp. 357–370). Geological Society, Special Publication No.202. https://doi.org/10.1144/gsl.sp.2002.202.01.18
Bishop, J. L., Mustard, J. F., Pieters, C. M., & Hiroi, T. (1998). Recognition of minor constituents in reflectance spectra of Allan Hills 84001 chips and the importance for remote sensing on Mars. *Meteoritics & Planetary Science*, *33*, 693–698. https://doi.org/10.1111/j.1945-5100.1998.tb01675.x
Bishop, J. L., Perry, K. A., Dyar, M. D., Bristow, T. F., Blake, D. F., Brown, A. J., & Peel, S. E. (2013). Coordinated spectral and XRD analyses of magnesite-nontronite-forsterite mixtures and implications for carbonates on Mars. *Journal of Geophysical Research*, *118*(4), 635–650. https://doi.org/10.1002/jgre.20066
Bishop, J. L., Pieters, C. M., Hiroi, T., & Mustard, J. F. (1998). Spectroscopic analysis of martian meteorite Allan Hills 84001 powder and applications for spectral identification of minerals and other soil components on Mars. *Meteoritics & Planetary Science*, *33*, 699–708. https://doi.org/10.1111/j.1945-5100.1998.tb01676.x
Bishop, J. L., Schelble, R. T., McKay, C. P., Brown, A. J., & Perry, K. A. (2011). Carbonate rocks in the Mojave Desert as an analog for Martian carbonates. *International Journal of Astrobiology*, *10*(4), 349–358. https://doi.org/10.1017/S1473550411000206
Bishop, J. L., Tirsch, D., Tornabene, L. L., Jaumann, R., McEwen, A. S., McGuire, P. C., et al. (2013). Mineralogy and morphology of geologic units at Libya Montes, Mars: Ancient aqueous outcrops, mafic flows, fluvial features and impacts. *Journal of Geophysical Research*, *118*(3), 487–513. https://doi.org/10.1029/2012JE004151
Blake, D. F., Morris, R. V., Kocurek, G., Morrison, S. M., Downs, R. T., Bish, D., et al. (2013). Curiosity at Gale Crater, Mars: Characterization and analysis of the Rocknest sand shadow. *Science*, *341*(6153). https://doi.org/10.1126/science.1239505
Blake, D. F., Vaniman, D. T., Achilles, C. N., Anderson, R., Bish, D. L., Bristow, T., et al. (2012). Characterization and calibration of the CheMin mineralogical instrument on Mars Science Laboratory. *Space Science Reviews*, *170*(1–4), 341–399. https://doi.org/10.1007/978-1-4614-6339-9_12
Blaney, D. L., & McCord, T. B. (1989). An observational search for carbonates on Mars. *Journal of Geophysical Research*, *94*, 10159–10166. https://doi.org/10.1029/jb094ib08p10159
Böttcher, M. E., Gehlken, P. L., & Usdowski, E. (1992). Infrared spectroscopic investigations of the calcite-rhodochrosite and parts of the calcite-magnesite mineral series. *Contributions to Mineralogy and Petrology*, *109*(3), 304–306. https://doi.org/10.1007/BF00283320
Bron, J. (1975). The importance of anharmonicity of the vibrational excited states in chemical kinetics. *Canadian Journal of Chemistry*, *53*(20), 3069–3074. https://doi.org/10.1139/v75-435
Bron, J., & Hacker, S. O. (1973). The anharmonicity correction for kinetic isotope effect calculations. *Canadian Journal of Chemistry*, *51*(16), 2765–2768. https://doi.org/10.1139/v73-413
Brown, A. J. (2006). Spectral curve fitting for automatic hyperspectral data analysis. *IEEE Transactions on Geoscience and Remote Sensing*, *44*, 1601–1608. https://doi.org/10.1109/tgrs.2006.870435
Brown, A. J., King, S. J., & Bishop, J. L. (2021). Distinguishing anhydrous carbonates using spectral centroid and asymmetry near 2.5 and 4 microns. Paper presented at the 52nd Lunar and Planetary Science Conference (Abstract #2708).
Brown, A. J., SimonHook, J. A., Baldridge, A. M., Crowley, J. K., Bridges, N. T., Thomson, B. J., et al. (2010). Hydrothermal formation of clay-carbonate alteration assemblages in the Nili Fossae region of Mars. *Earth and Planetary Science Letters*, *297*, 174–182. https://doi.org/10.1016/j.epsl.2010.1006.1018
Brown, A. J., & Storrie-Lombardi, M. C. (2006). *MR PRISM: A spectral analysis tool for the CRISM*. Paper presented at the Proceedings of SPIE Optics and Photonics, 6309—Instruments, Methods and Missions for Astrobiology IX.
Brown, A. J., Sutter, B., & Dunagan, S. (2008). The MARTE imaging spectrometer experiment: Design and analysis. *Astrobiology*, *8*(5), 1001–1011. https://doi.org/10.1089/ast.2007.0142
Brown, A. J., Viviano, C. E., & Goudge, T. A. (2020). Olivine-carbonate mineralogy of the Jezero Crater Region. *Journal of Geophysical Research: Planets*, *125*(3), e2019JE006011. https://doi.org/10.1029/2019JE006011
Burns, R. G. (1993). *Mineralogical applications of crystal field theory* (2nd ed., p. 551). Cambridge University Press.
Buzgar, N., Apopei, A. I., & Buzatu, A. (2009). *Romanian database of Raman spectroscopy*. Retreived from http://rdrs.ro
Calvin, W. M., King, T. V. V., & Clark, R. N. (1994). Hydrous carbonates on Mars? Evidence from Mariner 6/7 infrared spectrometer and groundbased telescopic spectra. *Journal of Geophysical Research*, *99*, 14659–14675. https://doi.org/10.1029/94je01090
Carrozzo, F. G., De Sanctis, M. C., Raponi, A., Ammannito, E., Castillo-Rogez, J., Ehlmann, B. L., et al. (2018). Nature, formation, and distribution of carbonates on Ceres. *Science Advances*, *4*(3), e1701645. https://doi.org/10.1126/sciadv.1701645
Carter, J., & Poulet, F. (2012). Orbital identification of clays and carbonates in Gusev crater. *Icarus*, *219*(1), 250–253. https://doi.org/10.1016/j.icarus.2012.02.024
Cheng, X., & Steele, R. P. (2014). Efficient anharmonic vibrational spectroscopy for large molecules using local-mode coordinates. *The Journal of Chemical Physics*, *141*(10), 104105. https://doi.org/10.1063/1.4894507
Clark, R. N., King, T. V. V., Klejwa, M., & Swayze, G. A. (1990). High spectral resolution reflectance spectroscopy of minerals. *Journal of Geophysical Research*, *95*(B8), 12653–12680. https://doi.org/10.1029/jb095ib08p12653
Clark, R. N., Swayze, G. A., Wise, R., Livo, E., Hoefen, T., Kokaly, R., & Sutley, S. J. (2007). *USGS digital spectral library splib06a*. U.S. Geological Survey.
Cloutis, E., Berg, B., Mann, P., & Applin, D. (2016). Reflectance spectroscopy of low atomic weight and Na-rich minerals: Borates, hydroxides, nitrates, nitrites, and peroxides. *Icarus*, *264*, 20–36. https://doi.org/10.1016/j.icarus.2015.08.026
Crowley, J. K. (1986). Visible and near-infrared spectra of carbonate rocks: Reflectance variations related to petrographic texture and impurities. *Journal of Geophysical Research: Solid Earth*, *91*(B5), 5001–5012. https://doi.org/10.1029/JB091iB05p05001
De Angelis, S., Carli, C., Tosi, F., Beck, P., Brissaud, O., Schmitt, B., et al. (2019). NIR reflectance spectroscopy of hydrated and anhydrous sodium carbonates at different temperatures. *Icarus*, *317*, 388–411. https://doi.org/10.1016/j.icarus.2018.08.012
De Angelis, S., Corte, V. D., Baratta, G. A., Rietmeijer, F. J. M., Brunetto, R., Palumbo, P., et al. (2011). Raman microspectroscopy performed on extraterrestrial particles. *Spectroscopy Letters*, *44*(7–8), 549–553. https://doi.org/10.1080/00387010.2011.610424

De Sanctis, M. C., Ammannito, E., Carrozzo, F. G., Ciarniello, M., Giardino, M., Frigeri, S., et al. (2018). Ceres's global and localized mineralogical composition determined by Dawn's Visible and Infrared Spectrometer (VIR). *Meteoritics & Planetary Science*, *53*(9), 1844–1865. https://doi.org/10.1111/maps.13104

De Sanctis, M. C., Ammannito, E., Raponi, A., Frigeri, A., Ferrari, M., Carrozzo, F. G., et al. (2019). Fresh emplacement of hydrated sodium chloride on Ceres from ascending salty fluids. *Nature Astronomy*, *4*(8), 786–793. https://doi.org/10.1038/s41550-020-1138-8

De Sanctis, M. C., Raponi, A., Ammannito, E., Ciarniello, M., Toplis, M. J., McSween, H. Y., et al. (2016). Bright carbonate deposits as evidence of aqueous alteration on (1) Ceres. *Nature*, *536*(7614), 54–57. https://doi.org/10.1038/nature18290

Deer, W. A., Howie, R. A., & Zussman, J. (1992). *An introduction to the rock-forming minerals* (2nd ed., p. 528). Longman.

Downs, R. T., & Hall-Wallace, M. (2003). The American Mineralogist crystal structure database. *American Mineralogist*, *88*, 247–250. https://doi.org/10.2138/am-2003-0409

Ehlmann, B. L., Mustard, J. F., Murchie, S. L., Poulet, F., Bishop, J. L., Brown, A. J., et al. (2008). Orbital identification of carbonate-bearing rocks on Mars. *Science*, *322*, 1828–1832. https://doi.org/10.1126/science.1164759

Ericksen, G. E. (1981). *Geology and origin of the Chilean nitrate deposits (Geological Survey Professional Paper 1188)*. United States Government Printing Office.

Fanale, F. P., Salvail, J. R., Banerdt, W. B., & Saunders, R. S. (1982). The regolith-atmosphere-cap system and climate change. *Icarus*, *50*, 381–407. https://doi.org/10.1016/0019-1035(82)90131-2

Farmer, V. C. (1974). *The infrared spectra of minerals* (p. 539). The Mineralogical Society.

Farsang, S., Facq, S., & Redfern, S. A. T. (2018). Raman modes of carbonate minerals as pressure and temperature gauges up to 6 GPa and 500 °C. *American Mineralogist: Journal of Earth and Planetary Materials*, *103*(12), 1988–1998. https://doi.org/10.2138/am-2018-6442

Gaffey, S. J. (1985). Reflectance spectroscopy in the visible and near-infrared (0.35–2.55 μm): Applications in carbonate petrology. *Geology*, *13*, 270–273. https://doi.org/10.1130/0091-7613(1985)13<270:RSITVA>2.0.CO;2

Gaffey, S. J. (1986). Spectral reflectance of carbonate minerals in the visible and near infrared (0.35-2.55 microns); calcite, aragonite, and dolomite. *American Mineralogist*, *71*(1–2), 151–162.

Gaffey, S. J. (1987). Spectral reflectance of carbonate minerals in the visible and near infared (0.35–2.55 μm): Anhydrous carbonate minerals. *Journal of Geophysical Research*, *92*, 1429–1440. https://doi.org/10.1029/jb092ib02p01429

Gaffey, S. J., McFadden, L. A., Nash, D., & Pieters, C. M. (1993). Ultraviolet, visible, and near-infrared reflectance spectroscopy: Laboratory spectra of geologic materials. In C. M. Pieters & P. A. J. Englert (Eds.), *Remote geochemical analysis: Elemental and mineralogical composition* (pp. 43–77). Cambridge University Press.

Goetz, A. F. H., Vane, G., Solomon, J. E., & Rock, B. N. (1985). Imaging spectrometry for Earth remote sensing. *Science*, *228*(4704), 1147–1153. https://doi.org/10.1126/science.228.4704.1147

Gooding, J. L. (1978). Chemical weathering on Mars. Thermodynamic stabilities of primary minerals (and their alteration products) from mafic igneous rocks. *Icarus*, *33*, 483–513. https://doi.org/10.1016/0019-1035(78)90186-0

Gooding, J. L., Wentworth, S. J., & Zolensky, M. E. (1988). Calcium carbonate and sulfate of possible extraterrestrial origins in the EETA79001 meteorite. *Geochimica et Cosmochimica Acta*, *52*(4), 909–915. https://doi.org/10.1016/0016-7037(88)90361-4

Grady, M. M., & Wright, I. (2006). The carbon cycle on early Earth—And on Mars? *Philosophical Transactions of the Royal Society B: Biological Sciences*, *361*(1474), 1703–1713. https://doi.org/10.1098/rstb.2006.1898

Groh, W. (1988). Overtone absorption in macromolecules for polymer optical fibers. *Makromolekulare Chemie*, *189*(12), 2861–2874. https://doi.org/10.1002/macp.1988.021891213

Gunasekaran, S., Anbalagan, G., & Pandi, S. (2006). Raman and infrared spectra of carbonates of calcite structure. *Journal of Raman Spectroscopy*, *37*(9), 892–899. https://doi.org/10.1002/jrs.1518

Gupta, V. P. (2016). 8—Vibrational frequencies and intensities. In V. P. Gupta (Ed.), *Principles and applications of quantum chemistry* (pp. 247–289). Academic Press. https://doi.org/10.1016/B978-0-12-803478-1.00008-X

Hamilton, V. E., Simon, A. A., Christensen, P. R., Reuter, D. C., Clark, B. E., Barucci, M. A., et al. (2019). Evidence for widespread hydrated minerals on asteroid (101955) Bennu. *Nature Astronomy*, *3*(4), 332–340. https://doi.org/10.1038/s41550-019-0722-2

Harner, P. L., & Gilmore, M. S. (2015). Visible-near infrared spectra of hydrous carbonates, with implications for the detection of carbonates in hyperspectral data of Mars. *Icarus*, *250*, 204–214. https://doi.org/10.1016/j.icarus.2014.11.037

He, L., O'Sullivan, J. A., Politte, D. V., Powell, K. E., & Arvidson, R. E. (2019). Quantitative reconstruction and denoising method HyBER for hyperspectral image data and its application to CRISM. *IEEE Journal of Selected Topics in Applied Earth Observations and Remote Sensing*, *12*(4), 1219–1230. https://doi.org/10.1109/JSTARS.2019.2900644

Hendricks, S. B., Posnjak, E., & Kracek, F. C. (1932). Molecular rotation in the solid state. The variation of the crystal structure of ammonium nitrate with temperature. *Journal of the American Chemical Society*, *54*(7), 2766–2786. https://doi.org/10.1021/ja01346a020

Herzberg, G. (1945). *Molecular spectra and molecular structure. II. Infrared and Raman spectra of polyatomic molecules*. D. Van Nostrand Co., Inc.

Hexter, R. M. (1958a). High-resolution, temperature-dependent spectra of calcite. *Spectrochimica Acta*, *10*(3), 281–290. https://doi.org/10.1016/0371-1951(58)80094-6

Hexter, R. M. (1958b). Infrared spectroscopic investigation of anion rotational disorder in sodium nitrate. *Spectrochimica Acta*, *10*(3), 291–298. https://doi.org/10.1016/0371-1951(58)80095-8

Hopkinson, L., Rutt, K. J., & Kristova, P. (2018). The near-infrared spectra of the alkali carbonates. *Spectrochimica Acta Part A: Molecular and Biomolecular Spectroscopy*, *200*, 143–149. https://doi.org/10.1016/j.saa.2018.04.020

Horgan, B. H. N., Anderson, R. B., Dromart, G., Amador, E. S., & Rice, M. S. (2020). The mineral diversity of Jezero crater: Evidence for possible lacustrine carbonates on Mars. *Icarus*, *339*, 113526. https://doi.org/10.1016/j.icarus.2019.113526

Hunt, G. R., & Salisbury, J. W. (1971). Visible and near-infrared spectra of minerals and rocks: II. *Carbonates, Modern Geology*, *2*, 23–30.

Hunt, G. R., & Vincent, R. K. (1968). The behavior of spectral features in the infrared emission from particulate surfaces of various grain sizes. *Journal of Geophysical Research*, *73*, 6039–6046. https://doi.org/10.1029/jb073i018p06039

Itoh, Y., & Parente, M. (2021). A new method for atmospheric correction and de-noising of CRISM hyperspectral data. *Icarus*, *354*, 114024. https://doi.org/10.1016/j.icarus.2020.114024

Kaplan, H. H., Lauretta, D. S., Simon, A. A., Hamilton, V. E., DellaGiustina, D. N., Golish, D. R., et al. (2020). Bright carbonate veins on asteroid (101955) Bennu: Implications for aqueous alteration history. *Science*, *370*(6517), eabc3557. https://doi.org/10.1126/science.abc3557

King, S. J., Bishop, J. L., & Brown, A. J. (2014). *Spectral properties of Ca-, Mg-, and Fe- bearing carbonates and implications for Mars*. Paper presented at the Eighth International Conference on Mars.

Kirschvink, J. L., Maine, A. T., & Vali, H. (1997). Paleomagnetic evidence of a low-temperature origin of carbonate in the Martian meteorite ALH 84001. *Science*, *275*, 1629–1633. https://doi.org/10.1126/science.275.5306.1629

Kokaly, R. F., Clark, R. N., Swayze, G. A., Livo, K. E., Hoefen, T. M., Pearson, N. C., et al. (2017). *USGS spectral library version 7* (Data Series 1035, p. 61). U.S. Geological Survey.

Kreisch, C. D., O'sullivan, J. A., Arvidson, R. E., Politte, D. V., He, L., Stein, N. T., et al. (2017). Regularization of Mars Reconnaissance Orbiter CRISM along-track oversampled hyperspectral imaging observations of Mars. *Icarus*, *282*, 136–151. https://doi.org/10.1016/j.icarus.2016.09.033

Krishnamurti, D. (1960). The Raman spectra of aragonite, strontianite and witherite. *Proceedings of the Indian Academy of Sciences—Section A*, *51*(6), 285–295. https://doi.org/10.1007/bf03045784

Lafuente, B., Downs, R. T., Yang, H., & Stone, N. (2015). *The power of databases: The RRUFF project* (pp. 1–30). De Gruyter. https://doi.org/10.1515/9783110417104-003

Lane, M. D. (1999). Midinfrared optical constants of calcite and their relationship to particle size effects in thermal emission spectra of granular calcite. *Journal of Geophysical Research*, *104*, 14099–14108. https://doi.org/10.1029/1999je900025

Lane, M. D., & Bishop, J. L. (2019). Chapter 3: Mid-infrared (thermal) emission and reflectance spectroscopy. In J. L. Bishop, J. F. Bell III, & J. E. Moersch (Eds.), *Remote compositional analysis: Techniques for understanding spectroscopy, mineralogy, and geochemistry of planetary surfaces* (pp. 42–67). Cambridge University Press.

Lane, M. D., & Christensen, P. R. (1997). Thermal infrared emission spectroscopy of anhydrous carbonates. *Journal of Geophysical Research*, *102*(E11), 25581–25592. https://doi.org/10.1029/97je02046

Lane, M. D., & Christensen, P. R. (1998). Thermal infrared emission spectroscopy of salt minerals predicted for Mars. *Icarus*, *135*, 528–536. https://doi.org/10.1006/icar.1998.5998

Lane, M. D., Dyar, M. D., & Bishop, J. L. (2004). Spectroscopic evidence for hydrous iron sulfate in the Martian soil. *Geophysical Research Letters*, *31*, L19702. https://doi.org/10.11029/12004GL021231

Le Paillier-Malécot, A. (1973). Étude spectroscopique de l'ion Mn2+ dans un monocristal de carbonate de manganèse naturel ($MnCO_3$) en phases paramagnétique et antiferromagnétique. *Journal de Physique*, *34*(5–6), 429–439. https://doi.org/10.1051/jphys:01973003405-6042900

Leshin, L. A., Mahaffy, P. R., Webster, C. R., Cabane, M., Coll, P., Conrad, P. G., et al. (2013). Volatile, isotope, and organic analysis of Martian fines with the Mars Curiosity rover. *Science*, *341*(6153). https://doi.org/10.1126/science.1238937

Lin, J.-F., Liu, J., Jacobs, C., & Prakapenka, V. B. (2012). Vibrational and elastic properties of ferromagnesite across the electronic spin-pairing transition of iron. *American Mineralogist*, *97*(4), 583–591. https://doi.org/10.2138/am.2012.3961

Lippmann, F. (1973). *Sedimentary carbonate minerals*. Springer Verlag.

Liu, J., Lin, J.-F., & Prakapenka, V. B. (2015). High-pressure orthorhombic ferromagnesite as a potential deep-mantle carbon carrier. *Scientific Reports*, *5*(1), 7640. https://doi.org/10.1038/srep07640

Lobanov, S. S., Goncharov, A. F., & Litasov, K. D. (2015). Optical properties of siderite ($FeCO_3$) across the spin transition: Crossover to iron-rich carbonates in the lower mantle. *American Mineralogist*, *100*(5–6), 1059–1064. https://doi.org/10.2138/am-2015-5053

Logan, L. M., Hunt, G. R., & Salisbury, J. W. (1975). The use of mid-infrared spectroscopy in remote sensing of space targets. In C. Karr (Ed.), *Infrared and Raman spectroscopy of lunar and terrestrial minerals* (pp. 117–142). Academic Press. https://doi.org/10.1016/b978-0-12-399950-4.50010-0

Lyon, R. J. P. (1964). *Evaluation of infrared spectrophotometry for compositional analysis of lunar and planetary soils, II, Rough and powdered surfaces* (Report No. NASA CR: 100). National Aeronautics and Space Administration.

Martin, J. B. (2017). Carbonate minerals in the global carbon cycle. *Chemical Geology*, *449*, 58–72. https://doi.org/10.1016/j.chemgeo.2016.11.029

Matossi, F. (1928). Absorption linear polarisierter ultraroter Strahlung im Kalkspat (2 μ–16 μ). *Zeitschrift für Physik*, *48*(9), 616–623. https://doi.org/10.1007/BF01339312

Mattila, A., Pylkkänen, T., Rueff, J. P., Huotari, S., Vankó, G., Hanfland, M., et al. (2007). Pressure induced magnetic transition in siderite $FeCO_3$ studied by X-ray emission spectroscopy. *Journal of Physics: Condensed Matter*, *19*(38), 386206. https://doi.org/10.1088/0953-8984/19/38/386206

McKay, C. P., & Nedell, S. S. (1988). Are there carbonate deposits in the Valles Marineris, Mars? *Icarus*, *73*(1), 142–148. https://doi.org/10.1016/0019-1035(88)90088-7

McKay, D. S., Gibson, E. K., Jr., Thomas-Keprta, K. L., Vali, H., Romanek, C. S., Clemett, S. J., et al. (1996). Search for past life on Mars: Possible relic biogenic activity in Martian meteorite ALH 84001. *Science*, *273*, 924–930. https://doi.org/10.1126/science.273.5277.924

Michalski, J. R., Cuadros, J., Niles, P. B., Parnell, J., Deanne Rogers, A., & Wright, S. P. (2013). Groundwater activity on Mars and implications for a deep biosphere. *Nature Geoscience*, *6*(2), 133–138. https://doi.org/10.1038/ngeo1706

Michalski, J. R., & Niles, P. B. (2010). Deep crustal carbonate rocks exposed by meteor impact on Mars. *Nature Geoscience*, *3*, 751–755. https://doi.org/10.1038/ngeo971

Ming, D. W., Archer, P. D., Glavin, D. P., Eigenbrode, J. L., Franz, H. B., Sutter, B., et al. (2014). Volatile and organic compositions of sedimentary rocks in Yellowknife Bay, Gale Crater, Mars. *Science*, *343*(6169). https://doi.org/10.1126/science.1245267

Moersch, J. E., & Christensen, P. R. (1995). Thermal emission from particulate surfaces: A comparison of scattering models with measured spectra. *Journal of Geophysical Research*, *100*, 7465–7477. https://doi.org/10.1029/94je03330

Morris, R. V., Ruff, S. W., Gellert, R., Ming, D. W., Arvidson, R. E., Clark, B. C., et al. (2010). Identification of carbonate-rich outcrops on Mars by the Spirit Rover. *Science*, *329*, 421–424. https://doi.org/10.1126/science.1189667

Mustard, J. F., & Hays, J. E. (1997). Effects on hyperfine particles on reflectance spectra from 0.3 to 25 μm. *Icarus*, *125*. https://doi.org/10.1006/icar.1996.5583

Palomba, E., Zinzi, A., Cloutis, E. A., D'Amore, M., Grassi, D., & Maturilli, A. (2009). Evidence for Mg-rich carbonates on Mars from a 3.9 μm absorption feature. *Icarus*, *203*, 58–65. https://doi.org/10.1016/j.icarus.2009.04.013

Parente, M., Itoh, Y., & Saranathan, A. (2019). *New CRISM data products for improved characterization and analysis of the Mars 2020 landing site*. Paper presented at the IGARSS 2019—2019 IEEE International Geoscience and remote sensing Symposium (pp. 4911–4914). IEEE https://doi.org/10.1109/igarss.2019.8899313

Petit, S., Decarreau, A., Martin, F., & Buchet, R. (2004). Refined relationship between the position of the fundamental OH stretching and the first overtones for clays. *Physics and Chemistry of Minerals*, *31*, 585–592. https://doi.org/10.1007/s00269-004-0423-x

Pollack, J. B., Kasting, J. F., Richardson, S. M., & Poliackoff, K. (1987). The case for a warm, wet climate on early Mars. *Icarus*, *71*, 203–224. https://doi.org/10.1016/0019-1035(87)90147-3

Pollack, J. B., Roush, T. L., Witteborn, F., Bregman, J., Wooden, D., Stoker, C., et al. (1990). Thermal emission spectra of Mars (5.4–10.5 μm): Evidence for sulfates, carbonates, and hydrates. *Journal of Geophysical Research*, *95*(B9), 14595–14627. https://doi.org/10.1029/jb095ib09p14595

Railsback, L. B. (1999). Patterns in the compositions, properties, and geochemistry of carbonate minerals. *Carbonates and Evaporites*, *14*, 1. https://doi.org/10.1007/BF03176144

Rampe, E. B., Blake, D. F., Bristow, T. F., Ming, D. W., Vaniman, D. T., Morris, R. V., et al. (2020). Mineralogy and geochemistry of sedimentary rocks and eolian sediments in Gale crater, Mars: A review after six Earth years of exploration with Curiosity. *Geochemistry*, *80*(2), 125605. https://doi.org/10.1016/j.chemer.2020.125605

Raponi, A., De Sanctis, M. C., Carrozzo, F. G., Ciarniello, M., Castillo-Rogez, J. C., Ammannito, E., et al. (2019). Mineralogy of Occator crater on Ceres and insight into its evolution from the properties of carbonates, phyllosilicates, and chlorides. *Icarus*, *320*, 83–96. https://doi.org/10.1016/j.icarus.2018.02.001

Reeder, R. J. (1990a). *Carbonates: Mineralogy and chemistry* (p. 399). Mineralogical Society of America.

Reeder, R. J. (1990b). Crystal chemistry of the rhombohedral carbonates. In R. J. Reeder (Ed.), *Carbonates: Mineralogy and chemistry* (pp. 1–47). Mineralogical Society of America.

Rietmeijer, F. J. M., Della Corte, V., Ferrari, M., Rotundi, A., & Brunetto, R. (2016). Laboratory analyses of meteoric debris in the upper stratosphere from settling bolide dust clouds. *Icarus*, *266*, 217–234. https://doi.org/10.1016/j.icarus.2015.11.003

Rockwell, B. W., & Hofstra, A. H. (2008). Identification of quartz and carbonate minerals across northern Nevada using ASTER thermal infrared emissivity data—Implications for geologic mapping and mineral resource investigations in well-studied and Frontier areas. *Geosphere*, *4*(1), 218–246. https://doi.org/10.1130/GES00126.1

Romanek, C. S., Jiménez-López, C., Navarro, A. R., Sánchez-Román, M., Sahai, N., & Coleman, M. (2009). Inorganic synthesis of Fe-Ca-Mg carbonates at low temperature. *Geochimica et Cosmochimica Acta*, *73*(18), 5361–5376. https://doi.org/10.1016/j.gca.2009.05.065

Ruff, S. W., Christensen, P. R., Barbera, P. W., & Anderson, D. L. (1997). Quantitative thermal emission spectroscopy of minerals: A technique for measurement and calibration. *Journal of Geophysical Research*, *102*(14), 899–814. https://doi.org/10.1029/97jb00593

Salisbury, J. W. (1993). Mid-infrared spectroscopy: Laboratory data. In C. M. Pieters, & P. A. J. Englert (Eds.), *Remote geochemical analysis: Elemental and mineralogical composition* (pp. 79–98). Cambridge University Press.

Salisbury, J. W., Hapke, B., & Eastes, J. W. (1987). Usefulness of weak bands in midinfrared remote sensing of particulate planetary surfaces. *Journal of Geophysical Research*, *92*(B), 702–710. https://doi.org/10.1029/jb092ib01p00702

Salisbury, J. W., & Wald, A. (1992). The role of volume scattering in reducing spectral contrast of reststrahlen bands in spectra of powdered minerals. *Icarus*, *96*, 121–128.

Salisbury, J. W., Walter, L. S., Vergo, N., & D'Aria, D. M. (1991). *Infrared (2.1–25 μm) spectra of minerals* (p. 267). Johns Hopkins University Press.

Sándorfy, C. (2006). Hydrogen bonding: How much anharmonicity? *Journal of Molecular Structure*, *790*(1), 50–54. https://doi.org/10.1016/j.molstruc.2005.07.036

Saranathan, A. M., & Parente, M. (2021). Adversarial feature learning for improved mineral mapping of CRISM data. *Icarus*, *355*, 114107. https://doi.org/10.1016/j.icarus.2020.114107

Sarrazin, P., Blake, D. F., Feldman, S., Chipera, S. J., Vaniman, D. T., & Bish, D. L. (2005). Field deployment of a portable X-ray diffraction/X-ray fluorescence instrument on Mars analog terrain. *Powder Diffraction*, *20*(2), 128–133. https://doi.org/10.1154/1.1913719

Schaefer, C., Bormuth, C., & Matossi, F. (1926). Das ultrarote Absorptionsspektrum der Carbonate. *Zeitschrift für Physik*, *39*(9), 648–659. https://doi.org/10.1007/BF01322127

Scheetz, B. E., & White, W. B. (1977). Vibrational spectra of the alkaline earth doublet carbonates. *American Mineralogist*, *62*, 36–50.

Scott, E. R. D., Krot, A. N., & Yamaguchi, A. (1998). Carbonate in fractures of Martian meteorite Allan Hills 84001: Petrologic evidence for impact origin. *Meteoritics & Planetary Science*, *33*, 709–719. https://doi.org/10.1111/j.1945-5100.1998.tb01677.x

Seelos, F. P., Viviano-Beck, C. E., Morgan, M. F., Romeo, G., Aiello, J. J., & Murchie, S. L. (2016). CRISM hyperspectral targeted observation PDS product sets—TERs and MTRDRs. Paper presented at the 47th Lunar and Planetary Science Conference (Abstract #1783).

Shannon, R. D. (1976). Revised effective ionic radii and systematic studies of interatomic distances in halides and chalcogenides, *Acta Crystallographica Section A*, *32*(5), 751–767. https://doi.org/10.1107/S0567739476001551

Sidey, V. (2016). On the effective ionic radii for ammonium. *Acta Crystallographica Section B*, *72*(4), 626–633. https://doi.org/10.1107/S2052520616008064

Siesler, H. W. (2017). Near-infrared spectra, interpretation. In J. C. Lindon, G. E. Tranter, & D. W. Koppenaal (Eds.), *Encyclopedia of spectroscopy and spectrometry* (3rd ed., pp. 30–39). Academic Press. https://doi.org/10.1016/B978-0-12-409547-2.12173-0

Simon, A. A., Kaplan, H. H., Hamilton, V. E., Lauretta, D. S., Campins, H., Emery, J. P., et al. (2020). Widespread carbon-bearing materials on near-Earth asteroid (101955) Bennu. *Science*, *370*(6517). https://doi.org/10.1126/science.abc3522

Speer, J. A. (1990). Crustal chemistry and phase relations of orthorhombic carbonates. In R. J. Reeder (Ed.), *Carbonates: Mineralogy and chemistry* (pp. 145–190). Mineralogical Society of America.

Stevenson, R. (1968). Absorption spectrum of MnCO3. *Journal of Applied Physics*, *39*(2), 1143–1145. https://doi.org/10.1063/1.1656202

Summers, D. M. (2012). The prebiotic chemistry of nitrogen and the origin of life. In J. Seckbach (Ed.), *Genesis-in the beginning: prebiotic life, chemical models and early biological evolution* (pp. 201–216). Springer. https://doi.org/10.1007/978-94-007-2941-4_12

Sutter, B., Dalton, J. B., Ewing, S. A., Amundson, R., & McKay, C. P. (2007). Terrestrial analogs for interpretation of infrared spectra from the Martian surface and subsurface: Sulfate, nitrate, carbonate, and phyllosilicate-bearing Atacama Desert soils. *Journal of Geophysical Research*, *112*. https://doi.org/10.1029/2006JG000313

Théorêt, A., & Sandorfy, C. (1964). Infrared spectra and crystalline phase transitions of ammonium nitrate. *Canadian Journal of Chemistry*, *42*(1), 57–62. https://doi.org/10.1139/v64-009

Tirsch, D., Bishop, J. L., Voigt, J. R. C., Tornabene, L. L., Erkeling, G., & Jaumann, R. (2018). Geology of central Libya Montes, Mars: Aqueous alteration history from mineralogical and morphological mapping. *Icarus*, *314*, 12–34. https://doi.org/10.1016/j.icarus.2018.05.006

Treiman, A. H., Barrett, R. A., & Gooding, J. L. (1993). Preterrestrial aqueous alteration of the Lafayette (SNC) meteorite. *Meteoritics*, *28*, 86–97. https://doi.org/10.1111/j.1945-5100.1993.tb00251.x

Urmos, J., Sharma, S., & Mackenzie, F. T. (1991). Characterization of some biogenic carbonates with Raman spectroscopy. *American Mineralogist*, *76*, 641–646.

Viviano, C. E., Moersch, J. E., & McSween, H. Y. (2013). Implications for early hydrothermal environments on Mars through the spectral evidence for carbonation and chloritization reactions in the Nili Fossae region. *Journal of Geophysical Research: Planets*, *118*(9), 1858–1872. https://doi.org/10.1002/jgre.20141

Wang, F., Bowen, B. B., Seo, J.-H., & Michalski, G. (2018). Laboratory and field characterization of visible to near-infrared spectral reflectance of nitrate minerals from the Atacama Desert, Chile, and implications for Mars. *American Mineralogist*, *103*(2), 197–206. https://doi.org/10.2138/am-2018-6141

Weir, C. E., & Lippincott, E. R. (1961). Infrared studies of aragonite, calcite, and vaterite type structures in the borates, carbonates, and nitrates. *Journal of Research of the National Bureau of Standards, Section A: Physics and Chemistry*, *65A*(3), 173–183. https://doi.org/10.6028/jres.065a.021

White, W. B. (1974). The carbonate minerals. In V. C. Farmer (Ed.), *The infrared spectra of minerals* (pp. 227–284). The Mineralogical Society.

Wiens, R., Maurice, S., McCabe, K., Cais, P., Anderson, R. B. & Beysaac, O. et al. (2016). The SuperCam remote sensing instrument suite for Mars 2020. Paper presented at the 47th Lunar and Planetary Science Conference (Abstract #1322).

Wray, J. J., Murchie, S. L., Bishop, J. L., Ehlmann, B. L., Milliken, R. E., Wilhelm, M. B., et al. (2016). Orbital evidence for more widespread carbonate-bearing rocks on Mars. *Journal of Geophysical Research*, *121*(4), 652–677. https://doi.org/10.1002/2015JE004972

Zubkova, N. V., Pushcharovsky, D. Y., Ivaldi, G., Ferraris, G., Pekov, I. V., & Chukanov, N. V. (2002). Crystal structure of natrite, γ-Na_2CO_3. *Neues Jahrbuch für Mineralogie—Monatshefte*, *2002*(2), 85–96. https://doi.org/10.1127/0028-3649/2002/2002-0085